# Labelling of cells with different materials for X-ray fluorescence imaging and cell targeting studies

## Dissertation

zur Erlangung des Doktorgrades

der Naturwissenschaften

(Dr.rer.nat)

dem

Fachbereich Chemie

der Universität Hamburg

vorgelegt von

**Yanan Kang**

Aus

Henan, China Hamburg, 2022

The presented work conducted under the supervision of Dr. Neus Feliu and Prof. Wolfgang Parak at the Center for Hybrid Nanostructures (CHyN) of the University of Hamburg, Germany (from November 2018 to November 2021).

First Evaluator:

Prof. Dr. Wolfgang Parak

Second Evaluator:

Prof. Dr. Kai Rothkamm

Examination commission members:

Prof. Dr. Wolfgang Parak (Chair)

Prof. Dr. Florian Grüner

Dr. Elisabetta Gargioni

Disputation date: 11.02.2022

# Index

# Abstract

X-ray imaging is a mature means of tissue imaging, making iodine-based contrast agents widely used in various scientific research and clinical imaging. After more than half a century of development, commercial iodine-containing contrast agents have been characterized by high water solubility, low biobinding, low toxicity, and high biotolerance. However, due to their rapid renal excretion and high dosage, they still damage the function of kidneys, heart, and thyroid. In order to find an optimal way of iodine delivery, small iodine-containing molecules (4IH) were labeled on BSA, dextran, PMA coated AuNPs, and synthesized iodine-doped AgI NPs, commercial contrast agent iohexol as the control. ICP-MS detected the content of iodine in each carrier, and the labeling efficiency was: PMA-Au-I<AgI NP<Dex-I<BSA-I, and there is about 4 iodine on each BSA molecule. In combination with endocytosis and exocytosis, results showed that within a non-cytotoxic iodine concentration range, BSA-I not only showed an order of magnitude higher cell internalization of iodine than that of iohexol, but also efflux less than 40% iodine from cells after 72 hours of endocytosis, compared with more than 95% of iohexol. The above results indicate that BSA is a safe and efficient carrier for delivering iodine into cells, paving the way for the subsequent X-ray imaging to acquire high-quality images and the development of new iodine contrast agents.

PSMA small molecule inhibitors have the advantages of good cell permeability and fast blood clearance, making them the first choice for constructing PCa molecular probes. Most of the small molecule reagents prepared for PSMA imaging and treatment are based on urea scaffolds. The glutamate-urea-based motif is a highly appropriate building block for preparing effective PSMA inhibitors. At present, research hotspots at home and abroad are mainly focused on developing nuclide-labeled molecules with a high affinity to PSMA. There are few studies on nanoparticles that use PSMA small molecule inhibitors as targets. Here, we prepared PSMA targeting nanoparticles with a small sulfhydryl ligand, mercaptoundecanoic acid (MUA) as a spacer, and a glutamate-urea-based PSMA small molecule inhibitor a targeting molecule. In vitro stability studies and cell uptake

experiments showed that small MUA functional ligand could not maintain sufficient stability of AuNP in cell culture medium, and the aggregation of nanoparticles resulted in no obvious evidence of the targeting of PSMA-I, which required further optimization of the ligand before investigation.

With the in-depth study of targeted nanoparticles, researchers have found that the targeting efficiency of nanoparticles is deeply affected by factors such as the antibody density or size or direction on the surface. However, the platform to investigate the targeting efficiency of a single variable is still missing. It is not easy to find conclusive evidence that their surface antibody density determines the targeting efficiency of nanoparticles. To this end, we used scFv and SNAP-tag to control the effect of antibody size and orientation and constructed a platform to investigate the impact of antibody density on targeting efficiency with a single variable. The successful preparation and purification of AuNPs with a discrete number of ligands highlights their potential as a reliable platform for studying the relationship between targeting efficiency and antibody density.

## Zusammenfassung

Röntgenbildgebung ist Eine etablierte Methode der Gewebebildgebung, wodurch jodbasierte Kontrastmittel in einer Vielzahl von wissenschaftlichen Forschungen und klinischen Bildgebungen weit verbreitet sind. Nach mehr als einem halben Jahrhundert Entwicklung zeichnen sich kommerzielle jodhaltige Kontrastmittel durch hohe Wasserlöslichkeit, geringe Biobindung, geringe Toxizität und hohe Biotoleranz aus. Aufgrund ihrer schnellen renalen Ausscheidung und hohen Dosierung schädigen sie jedoch die Nieren-, Herz- und Schilddrüsenfunktionen. Um einen optimalen Weg der Jodzufuhr zu finden, wurden kleine jodhaltige Moleküle (4IH) auf BSA, Dextran, PMA-beschichteten AuNPs und synthetisierten Jod-dotierten AgI-NPs mit dem kommerziellen Kontrastmittel Iohexol als Kontrolle markiert. Der Jodgehalt in jedem Träger wurde durch ICP-MS nachgewiesen, und die Markierungseffizienz war: PMA-Au-I < AgI NP < Dex-I < BSA-I, und es gibt ungefähr 4 Jod auf jedem BSA-Molekül. In Kombination mit Endozytose- und Exozytose-Experimenten zeigte sich, dass innerhalb eines nicht-zytotoxischen Iod-Konzentrationsbereichs, BSA-I nicht nur eine um Größenordnungen höhere Internalisierung von Jod in die Zellen aufweist als Iohexol, sondern auch weniger als 40 % Jod aus den Zellen nach 72 Stunden Endozytose ausschleust, verglichen mit mehr als 95 % bei Iohexol. Die obigen Ergebnisse zeigen, dass BSA ein sicherer und effizienter Träger für die Einbringung von Jod in die Zellen ist, der den Weg für die anschließende Röntgenbildgebung zur Gewinnung hochwertiger Bilder und die Entwicklung neuer Jodkontrastmittel ebnet.

Niedermolekulare PSMA-Inhibitoren haben den Vorteil, dass sie gut zelldurchlässig sind und schnell vom Blut ausgeschieden werden, was sie zur ersten Wahl für die Entwicklung von molekularen PCa-Sonden macht. Die meisten der bisher hergestellten niedermolekularen Reagenzien für die PSMA-Bildgebung und -Behandlung basieren auf Harnstoffgerüsten, insbesondere das Glutamat-Harnstoff-Motiv ist ein sehr geeigneter Baustein für die Herstellung wirksamer PSMA-Inhibitoren. Derzeit konzentrieren sich die Forschungsschwerpunkte im In- und Ausland vor allem auf die Entwicklung nuklidmarkierter Moleküle mit hoher Affinität zu PSMA, und es gibt nur wenige Studien zu

Nanopartikeln, die kleine PSMA-Inhibitoren als Zielstruktur verwenden. Hier haben wir PSMA Targeting-Nanopartikel mit einem kleineren Sulfhydryl-Liganden, Mercaptoundecanoic Säure (MUA) als Spacer und ein PSMA klein Molekül-Inhibitor basierend auf Glutamat-Harnstoff hergestellt. In-vitro-Stabilitätsstudien und Experimente zur Zellaufnahme zeigten, dass der kleine funktionelle MUA-Ligand keine ausreichende Stabilität der AuNP im Zellkulturmedium aufrechterhalten konnte, und die Aggregation der Nanopartikel führte zu keinem offensichtlichen Hinweis auf das Targeting von PMA-I, was eine weitere Optimierung des Liganden vor der Untersuchung erforderte.

Bei der eingehenden Untersuchung von zielgerichteten Nanopartikeln haben Wissenschaftler festgestellt, dass die Zielgenauigkeit von Nanopartikeln stark von Faktoren wie der Antikörperdichte, der Antikörpergröße oder der Dichte auf der Oberfläche beeinflusst wird. Es fehlt jedoch noch eine Plattform zur Untersuchung der Targeting-Effizienz einer einzelnen Variable, und es ist schwierig, schlüssige Beweise dafür zu finden, dass die Targeting-Effizienz von Nanopartikeln durch ihre Oberflächen-Antikörperdichte bestimmt wird. Zu diesem Zweck haben wir scFv- und SNAP-Tags verwendet, um die Auswirkungen der Antikörpergröße und der festen Ausrichtung zu kontrollieren, und eine Plattform konstruiert, um die Auswirkungen der Antikörperdichte auf die Zieleffizienz mit einer einzigen Variable zu untersuchen. Die erfolgreiche Herstellung und Reinigung von AuNPs mit einer diskreten Anzahl von Liganden unterstreicht ihr Potenzial als zuverlässige Plattform für die Untersuchung der Beziehung zwischen Targeting-Effizienz und Antikörperdichte.

# 1. Introduction

## 1.1. Iodine as a contrast agent for X-ray fluorescence imaging

Medical imaging is a technique that aims to take images of internal tissues of the human body or a part of the human body in a non-invasive manner to diagnose and examine diseases, provide valuable information for implementing treatment plans, and track disease progression or drug efficacy. At present, the diagnostic methods used in the clinic include ultrasound imaging (USG), computed tomography (CT), magnetic resonance imaging (MRI), positron emission tomography (PET), single-photon emission computed tomography (SPECT), and optical imaging[1] (Figure 1-1).
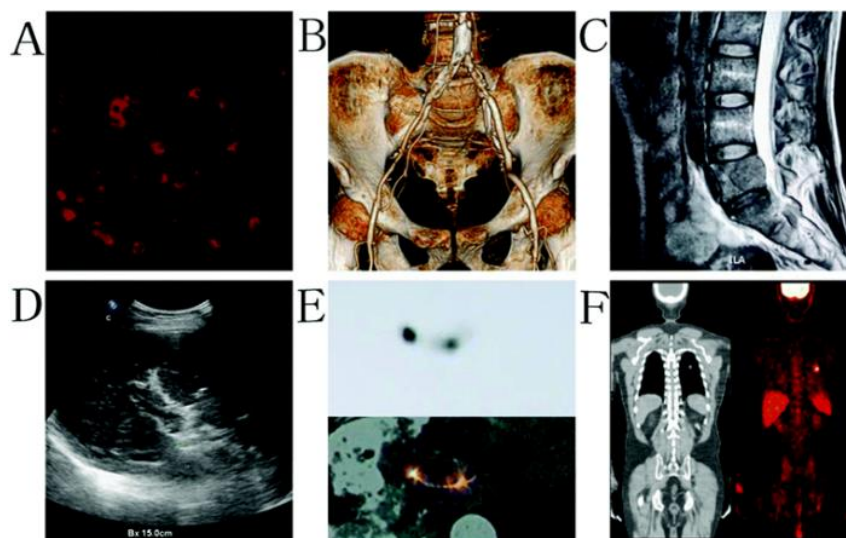


*Figure 1-1.* *The main imaging technology for clinical applications. A) Fluorescence image of tumor cells; B) CT image of arterial stenosis; C) MRI image of lumbar metastasis; D) US detection of portal vein thrombosis; E) SPECT evaluation of $^{125}I$ seed implantation; F) PET detection of lung cancer. The figure was extracted from reference[2].*

Of all the medical imaging techniques available, X-ray imaging is one of the most commonly used because of its high resolution and low cost. X-rays are a form of ionizing electromagnetic radiation that has a specific penetrating force. Utilizing the difference in human tissue density and thickness, the amount of X-rays absorbed during the penetration

process is different, creating a contrast between tissues and organs[3]. The transmitted X-ray signal undergoes imaging processing, such as X-ray film, screen or TV screen display, and X-ray image with black and white contrast, and the level difference can be obtained.

However, soft tissues such as the gastrointestinal, cardiovascular, urinary, liver, lungs, and tumor tissues lack sufficient contrast, and the imaging effect is inferior[4]. At this time, contrast agents are needed to improve imaging efficiency. Currently, X-ray contrast agents are mainly small molecules containing iodine. Iodine (I) is introduced as the main component of X-ray contrast agents due to its high-quality X-ray absorption coefficient[5]. In the past century, iodized contrast agents have transitioned from inorganic iodine to organic monoiodized, deionized, and triiodized molecules, from lipophilic to hydrophilic, from ionic to nonionic, and from monomer to dimer[6] (Figure 1-2).
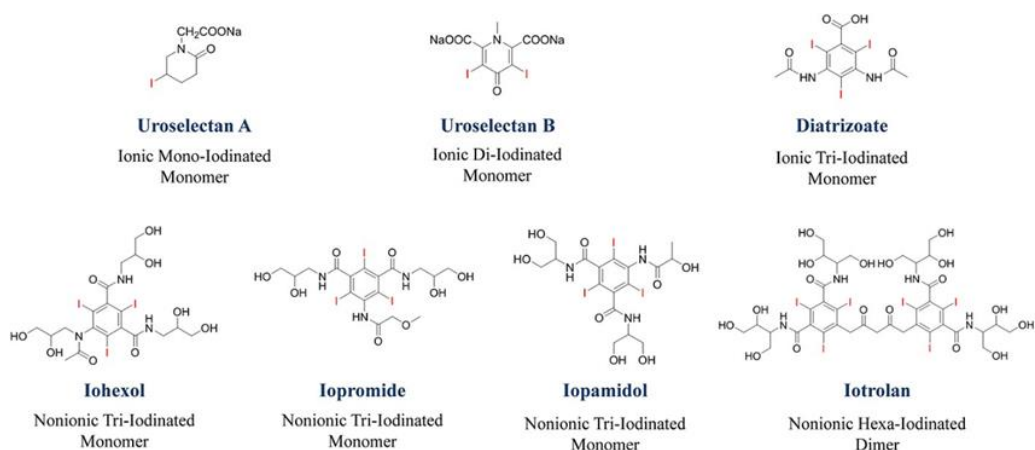


*Figure 1-2. Chemical structure of representative iodinated X-ray contrast agents. The development of iodized X-ray contrast agents has shifted from inorganic and organic lipophilic ionic molecules to organic hydrophilic non-ionic molecules. The figure was extracted from reference[7].*

The evolution of iodinated contrast agents has dramatically reduced the toxic and side effects during clinical use. For example, compared with ionic type, non-ionic type reduces the reaction with the polypeptide, cell membrane, and other biological structures[8]; reduces the adverse effects of high osmotic pressure ion type on the heart and kidneys[6, 8]. In addition to the problem of equal osmotic pressure, viscosity after the formulation of the

6

contrast agent also needs to be considered[9-10]. In addition, the high-viscosity contrast agent stays in the kidney for a longer time, which is likely to cause kidney damage[10]. Although many efforts have been made to improve the physical and chemical properties of iodinated contrast agents, commercial contrast agents such as iohexol and iomethol still have significant limitations in clinical applications[7]. The kidney has an immediate clearance effect on iodine-containing small molecule contrast media[11]. Iodine-containing compounds have only a concise imaging time. Usually, they require repeated administration of large doses, which can easily cause severe adverse reactions, such as allergic reactions, contrast nephropathy, and thyroid dysfunction[12-14].

Due to the inherent limitations of iodinated small molecule contrast agents, most studies use NP to improve the formulation of X-ray contrast agents. The most direct strategy is to use the shielding ability of metal nanoparticles to X-rays to achieve CT contrast enhancement instead of iodine as a contrast agent for X-ray imaging. Gold ($Z = 79$) has been extensively studied because it has high-K edge energy of 80.7 keV, is incredibly dense (19.3 g/cm$^3$), and is generally considered biocompatible and biologically inert[4]. Jackson et al.[15] determined the advantages of AuNP and traditional contrast agents in image contrast enhancement. At a concentration of 0.5077 M, the contrast enhancement of AuNP is 88% higher than iodine at low energy and 115% higher at high energy (Figure 1-3). The inherent properties of nanostructures made of metals depend on their size, shape, composition, and internal structure. The differences between them may affect their biological distribution and their recognition by phagocytes[7]. Another strategy is to covalently bond the iodinated small molecules to the polymer backbone[16], or physically trap the iodinated small molecules into the polymer carrier to form NPs[17]. Due to the leakage problem of physical embedding, few studies have been reported. Covalent bonding can prevent the leakage and loss of iodinated molecules from NP. Therefore, it is essential to evaluate the biodegradability and safety of NPs of different sizes made from various polymers. Finding a suitable vector for carrying iodine into cells is a potential strategy to solve the limitations of X-ray imaging applications.
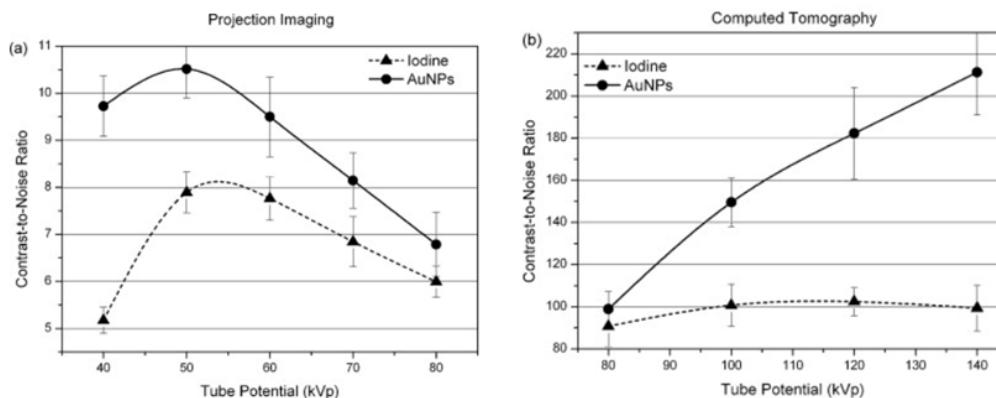
***Figure 1-3.*** *Comparison of contrast-to-noise ratio between AuNPs and iodine-based X-ray contrast agents at different X-ray tube potentials. The graph shows that the contrast and noise ratio of AuNP and Ultravist® for (A) CR and (B) CT imaging depend on the applied X-ray tube potential. The figure was extracted from reference[15].*

## 1.2. Small molecule inhibitor targeting prostate specific membrane antigen (PSMA) for diagnosis and treatment

With the development of science and technology and people's higher requirements for tumor treatment effects, integrated application methods for tumor diagnosis and treatment is the leading research goal of current scientists[18]. To solve this medical problem, nanomedicine diagnostic and therapeutic agents came into being. It integrates drugs and imaging reagents into nanoparticles and uses the small size effect, surface effect, and quantum effect of nanoparticles to make them have unique light, sound, heat, magnetism, electricity, and other unique properties to deliver drugs to pathological tissues. Based on these unique properties of nanomaterials, nanomedicine diagnostic and therapeutic agents can achieve one or more treatment methods, including photodynamic, photothermal, sonodynamic therapy, and drug therapy, combined with tumor site imaging, to accurately treat tumor lesions[19] (Figure 1-4).
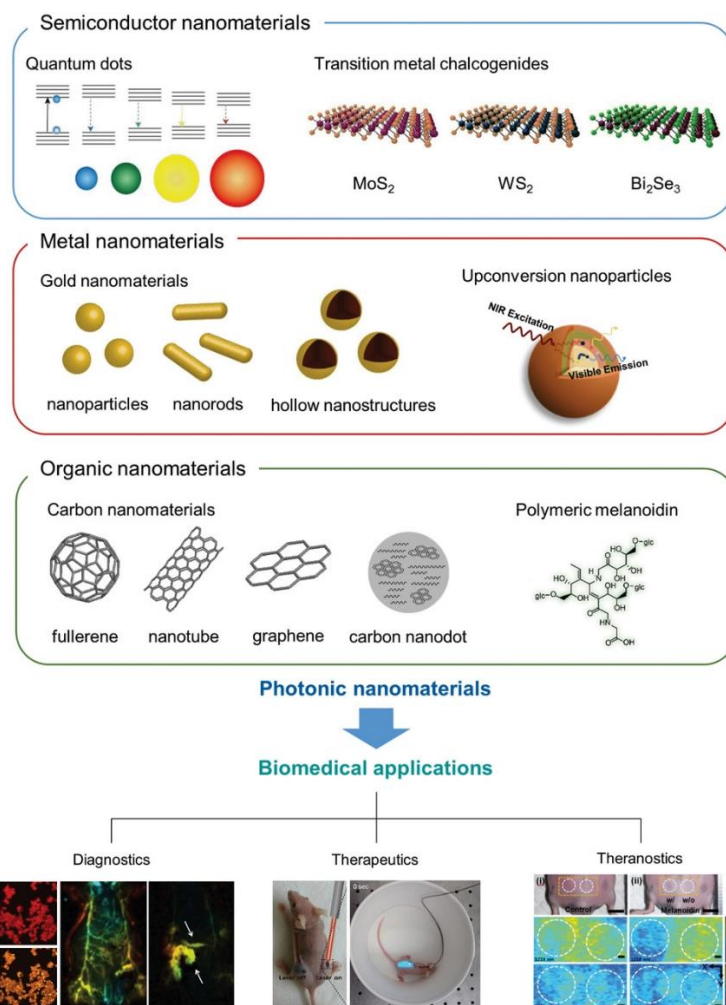
***Figure 1-4.*** *Nanomaterials for diagnostic, therapeutic and therapeutic diagnostic applications. The figure was extracted from reference[20].*

In recent decades, researchers have discovered that receptors are overexpressed on the surface of many tumor cells, and these receptors are generally closely related to the growth and proliferation of tumor cells[21]. However, on the surface of normal cells, these receptors are usually not expressed or low expressed. Therefore, molecules that can specifically bind to these receptors can be connected to appropriate drug carriers through electrostatic adsorption and covalent bonding to form a receptor-mediated nano-active targeted drug delivery system[22]. Compared with passive targeted drug delivery, active targeted delivery can achieve drug uptake of normal cells and tissues far below the tumor site, overcome the shortcomings of poor free drug selectivity, and achieve precise diagnosis and treatment of tumor sites.

In recent years, prostate cancer has been the most common malignant tumor in men and the third leading cause of cancer-related death worldwide[23]. Prostate-specific membrane antigen (PSMA) is a type II transmembrane protein that is highly expressed on the surface of prostate cancer epithelial cell membranes in the form of monomers or dimers. However, its enzymatic activity in prostate cancer cells has not yet been elucidated[24]. PSMA is not only expressed in the epithelial cell membrane of prostate cancer, but also the neovascular endothelial cell membrane of other solid tumors, such as bladder cancer, pancreatic cancer, lung cancer, and kidney cancer; as well as normal tissues and organs, such as salivary glands, lacrimal glands, proximal tubules, epididymis, ovaries, astrocytes, and central nervous system, PSMA also expresses[25]. In normal prostate epithelial cells, PSMA is only slightly expressed in the cytoplasm and on the apical membrane side of the cell, not on the basement membrane side, so it cannot be bound by targeting molecules[26]. The PSMA located in the cytoplasm is the product of the N-terminal truncation of the transmembrane protein, called PSM', and its role has not yet been elucidated. In the prostate tissue with dysplasia, PSMA can be seen transporting from the apical membrane side to the basement membrane side. With the progress of dysplasia and tumor aggressiveness, the expression of PSMA on the basement membrane side increases significantly. Studies have shown that the higher the Gleason score, the higher the PSMA/PSM' ratio[27]. Therefore, PSMA may promote tumor invasion and metastasis, but existing studies have not yet clarified its mechanism of action. Due to the characteristics mentioned above of PSMA, PSMA is a sensitive and specific prostate cancer marker and an important target molecule for the diagnosis and treatment of prostate cancer, with good application prospects.

In recent years, ligands targeting PSMA have developed rapidly, which are mainly divided into three categories: monoclonal antibodies, aptamers, and small molecule inhibitors. Radionuclide-labeled monoclonal antibodies are the earliest PSMA targeting molecules used in imaging. For example, 7E11 ([111]InCYT-356, ProstaScint) is currently the only prostate cancer imaging agent approved by the US Food and Drug Administration (FDA)[28]. However, the limitations of monoclonal antibodies are inevitable: potential immunogenicity; the considerable molecular weight of the antibody leads to poor tumor

tissue permeability; the low uptake rate makes the image quality unsatisfactory[29]. Aptamer A10 is a specific aptamer for PSMA. In vitro experiments have confirmed that the aptamer A10 carrying adriamycin and cisplatin can help transport these chemotherapeutic drugs into prostate cancer cells to achieve the effect of inhibiting tumor cell growth[30]. However, as oligonucleotides or oligopeptides, aptamers are sensitive to temperature and pH changes, making it difficult to label the nuclide.



(a)

1: R= $SCH_3$
2: R= Ph (4-OH, 3-I)
3: R= $SCH_2$Ph (4-F)
4: R= $CH_2CH_2CH_2$NHCOPh (4-I)

(b)
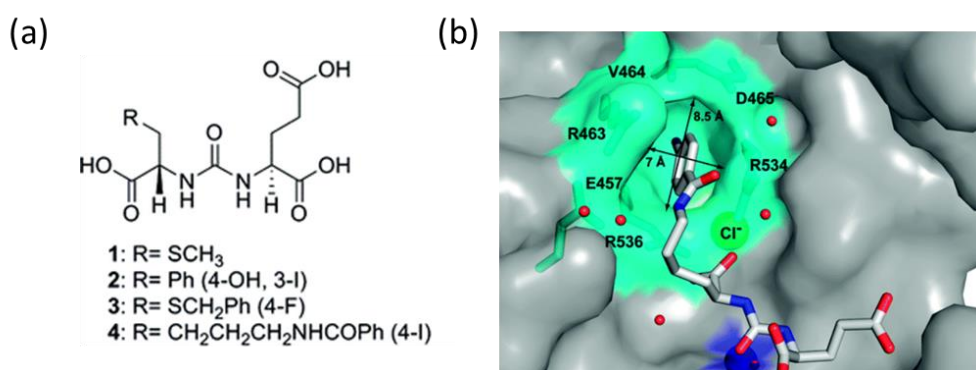
*Figure 1-5.* *(A) The skeleton structure of PSMA small molecule inhibitor Glu-Urea. (B) The hydrophobic pocket accessory to the S1 site. The active site bound DCIBzL is in stick representation. The dissected substrate-binding cavity of PSMA is shown in semi-transparent surface representation (gray). The side chains of amino acids delineating the "accessory hydrophobic pocket" are shown in stick representation and colored cyan. The active-site $Zn^{+2}$ and S1 bound $Cl^-$ are colored blue and represented as a transparent sphere, respectively and water molecules are shown as red spheres. The figure was extracted from reference[31].*

PSMA small molecule inhibitors mainly have three types of groups, namely urea group, thiol group and phosphate group. Among them, the urea group with the highest affinity has a small molecular weight and high clearance rate, which has been proven to be used to diagnose and treat prostate cancer[32]. Cyril Bafinka and Younjoo Byunt et al.[31] designed and synthesized GCPII type small molecule inhibitors containing glutamate-urea (Glu-Urea) skeleton (Figure 1-5) and evaluated their binding mechanism and binding effect. The experimental results prove that the designed and synthesized Glu-Urea framework small molecule inhibitor can specifically bind to GCPII. Since GCPII and PSMA have the same

enzymatic activity, small molecule compounds containing Glu-Urea backbone can also specifically bind to PSMA. Therefore, the use of Glu-Urea small molecule compounds as PSMA targeting molecules for molecular imaging of prostate cancer has a good application prospect.

Recently, Joey et al.[33] reported a prostate-specific membrane antigen (PSMA-1)-targeted gold nanoparticle (AuNP-5kPEG-PSMA-1Pc4) for photodynamic therapy of prostate cancer (Figure 1-6). In vitro cell uptake experiments showed that PSMA-positive PC3-pip cells had significantly higher nanoparticle uptake than PSMA-negative PC3-flu cells. In addition, more complete cell killing was observed under different doses of light in Pc3-pip than in PC3-flu cells, indicating that Pc4 has active targeting after release. Similarly, in vivo studies have shown that tumors expressing PSMA in remission 14 days after PDT. It proves that the nano system can provide surgical guidance for prostate tumor resection and therapeutic intervention when surgery is insufficient.
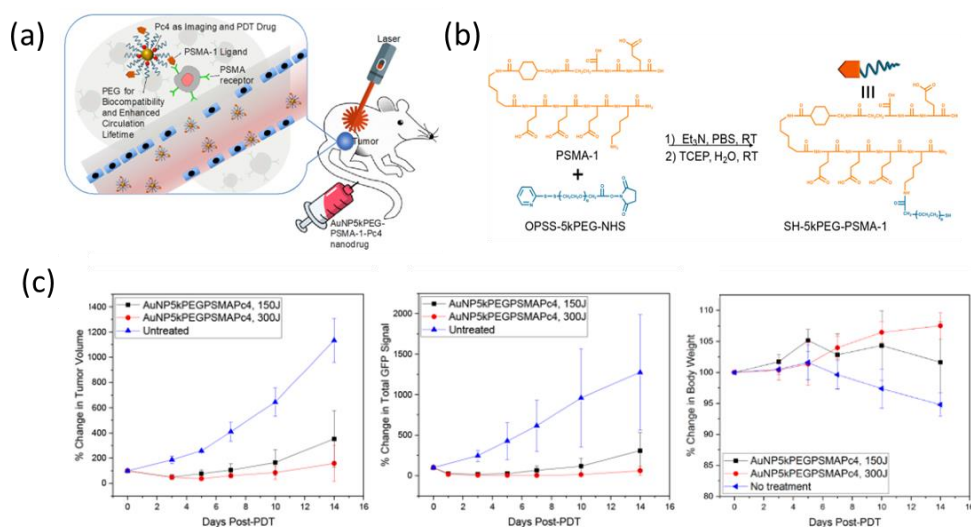


*Figure 1-6. (A) Schematic diagram of PSMA-1 targeting gold nanoparticles containing Pc4 as imaging agent and PDT agent. (B) Schematic diagram of the structure of the ligand SH-5kPEG-PSMA-1. (C) Determine the therapeutic effect by monitoring the tumor volume, total GFP signal and body weight, respectively. The figure was extracted from reference[33].*

## 1.3. Oriented immobilization of antibodies

### 1.3.1. Antibodies and single chain antibody scFv

As critical biological molecules in the immune system, antibodies are mainly secreted by B lymphocytes and memory cells. They can specifically bind to specific antigens and play an irreplaceable role in the process of identifying, and targeting pathogens. The most common antibody in a biological body, such as IgG antibody (~150kDa), consists of two heavy chains (H chain) and two light chains (L chain); disulfide bonds generally connect the heavy chain and light chain. Through a variety of interactions (hydrogen bond, hydrophobic interaction, electrostatic interaction, etc.) stable combination, the overall structure presents a "Y" shape[34] (Figure 1-7). The antigen binding region is generally located at the end of the two arms of the "Y". The amino acid sequence of this region is highly variable and has achieved the purpose of identifying different antigens and epitopes, so it is also called the variable region.
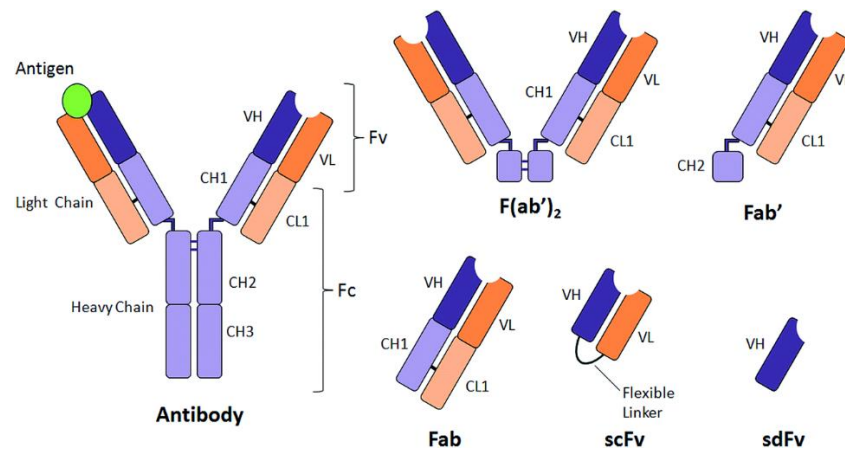


*Figure 1-7. Schematic of an IgG antibody and a nomenclature of some of its possible fragments. The heavy and light chains are shown in purple and orange respectively. The figure was extracted from reference[35].*

Researchers realize the simplification of traditional antibodies through genetic engineering methods. A small molecule antibody-single-chain antibody (scFv) containing only the heavy chain's variable region and the light chain's variable region was prepared, connected by a flexible peptide linker, with a molecular weight of about 30kDa[36]. scFv is a small molecule antibody with a complete antigenic determinant type, that is, it has all antigen-specific

recognition sites and is also a key component of antibody. The molecule is small, and the immunogenicity is low. In the construction and expression, smaller molecules are easier to obtain, and it is easier to penetrate solid tumors to play a role[37-38]. At the same time, scFv also has excellent operability and can be coupled with polyethylene glycol[36], chemotherapeutic drugs[39], various proteins[40], etc., for clinical diagnosis or treatment.

## 1.3.2. Introduction to oriented immobilization of antibodies

Although there are many ways to immobilize antibodies on the surface of nanoparticles, the loss of biological activity after the immobilization of antibodies has always existed. The binding of the antibody on the carrier may have different spatial orientations (Figure 1-8). Only when the antigenic determinant (Fab end) is far away from the solid surface can it more sensitively capture the antigen molecule in the solution and maximum maintain its immunological activity. The random orientation will inactivate part of the immobilized antibody due to steric hindrance and lose its antigen-binding activity[41]. For example, the traditional method based on antibody amino immobilization is convenient and straightforward in operation and does not require special treatment of antibodies. However, because lysine is widely present in proteins when the amino group of the protein is used to immobilize antibodies, the problem of random spatial fixation and multi-point fixation will inevitably occur. The spatial conformation of the immobilized protein changes, and the protein is partially or completely inactivated[42].
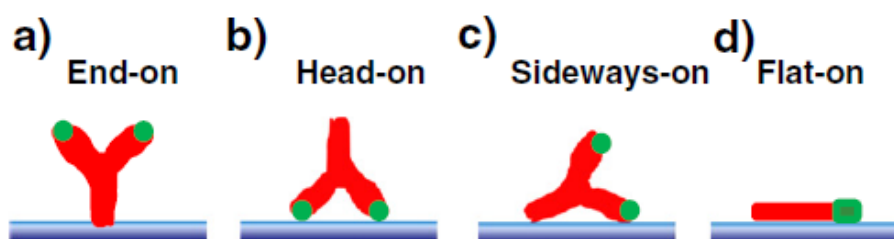


***Figure 1-8.*** *Schematic of the four possible spatial directions of the antibody on the surface of the stationary phase. The figure was extracted from reference[41].*

Directional immobilization of antibodies can keep the "head" of the antibody in an upward

direction without interfering with the immunoreactivity of the antibody antigen, and the binding ability of antigen with it is 2-8 times higher than that of antibody with random fixation, significantly improving the utility of antibody[43]. In recent years, the strategy of using a site-specific (directed) modification to connect affinity ligands has attracted more and more attention. Its advantage lies in the realization of a single-point covalent connection between the affinity ligand and the medium through a site-specific chemical reaction, which guarantees and retains the homogeneity and activity of the affinity ligand to the greatest extent[44]. To this end, various specific binding methods have been developed, such as streptavidin-biotin system, cyclooctyne and azide group clicking chemical modification, targeted proteins A and G, containing peptide-mediated protein splicing, the introduction of unnatural aldehydes into protein structures, protein tag, etc[45-49]. Among them, the introduction of the protein tag has a negligible impact on the yield of the target protein and activity of the target protein, which has the feasibility of production scale-up.

### 1.3.3. Introduction to SNAP-tag protein

Protein tag refers to a polypeptide or protein expressed by fusion with the target protein using DNA in vitro recombination technology to facilitate the expression, detection, tracking, and purification of the target protein. With the continuous development of technology, researchers have successively developed protein tags with various functions. Mainly include: 6xHIS, Flag, GST, c-Myc, eGFP/eCFP/eYFP/mCherryeGFP, HA, SUMO, MBP, Avi-tag, SNAP-tag, Halo-tag, etc[50-52]. Among them, SNAP-tag has developed rapidly due to its high specificity, stability, and diversity of ligands and has been widely used in many fields, such as protein labeling[53] (Figure 1-9).
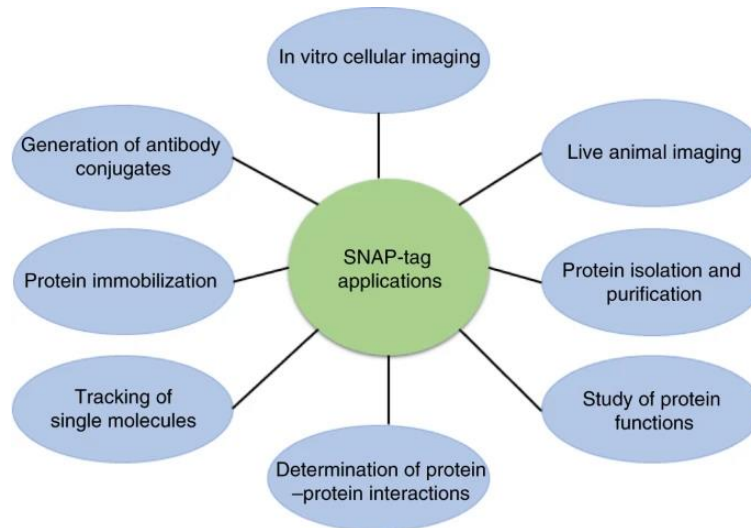
*Figure 1-9.* *Snap-tag technology is used in a variety of biomedical applications, such as in vitro cell imaging, in vivo animal imaging, protein isolation and purification, protein function studies, determination of protein interactions, single-molecule tracking, protein immobilization, and antibody conjugation. The figure was extracted from reference[53].*

SNAP-tag is obtained from a mutant of human $O^6$-methylguanine-DNA methyltransferase (hAGT). In 2003, Johnsson et al.[54] developed SNAP-tag protein tags that can specifically bind to $O^6$-phenylmethylguanine (BG) by taking advantage of hAGT's ability to transfer the alkyl of $O^6$-methylguanine to its active cysteine residue. Related research shows that SNAP-tag can also identify BG derivatives. SNAP-tag has become a powerful tool for protein immobilization and purification by virtue of its high specific recognition and stable covalent binding with BG substrate. At present, the primary methods to realize the immobilization of SNAP-tag fusion protein through BG functionalization on the solid surface are: 1) chemical modification of solid surface based on amino-BG derivatives; 2) supramolecular assembly based on a solid surface; 3) directed immobilization of DNA[55].

Since SNAP-tag can be efficiently and specifically covalently bound to BG substrates, it can be used to modify antibodies by effector molecules, which can overcome the disadvantages of current methods for chemically modifying antibodies by effector molecules[56], so as to achieve uniform antibody labeling and reduce the mutual interference between antibody and effector molecules. Davide et al.[36] fused the single-chain antibody

(scFv) of HER2 with SNAP-tag and used the specific recognition of BG substrate and SNAP-tag to fix the scFv on the surface of MFN, which can effectively target MCF7 cells with expressing HER2 receptor. This method can immobilize peptide ligands that selectively target specific cancer cells on nanoparticles and has a universal value for developing targeted nanoparticles for biomedical applications.

## 1.4. Motivation of the study

### 1.4.1. Study on iodine-labeled carrier for X-ray fluorescence imaging of cells

After the contrast agent enters the body, it can enhance the contrast of organs or tissues, thereby obtaining clearer tissue images, which is conducive to the following clinical diagnosis and treatment. In X-ray imaging, the most widely used non-ionic iodine-containing contrast agent in the clinic is that it does not ionize in an aqueous solution and has low osmotic pressure. Its toxic and side effects are reduced because the structure does not contain carboxyl groups[57]. Although non-ionic iodine-containing CT contrast agents overcome some of the shortcomings of ionic contrast agents, however, such iodine-containing CT contrast agents generally have disadvantages such as non-specific distribution in the body, large doses, short imaging time, and toxicity to blood vessels, kidneys, and central nerves[58-59], which limit their further application. Although many researchers have proposed nanoparticles to solve these problems[60-61], few studies have explored safe and suitable iodine delivery materials. To explore the best way to deliver iodine, we compared the delivery capabilities of different materials, which including: labeling iodine on the polymer coating of AuNP; doping in nanoparticles (AgI NP); protein delivery iodine—iodine-labeled BSA; polysaccharide delivery iodine—iodine-labeled dextran. The purpose of this research is to study the fate of different materials labeled with iodine in cells and find out a carrier that can deliver as much iodine as possible to cells, providing new directions for the development of iodine-containing contrast agents in the future.

### 1.4.2. 3. Evaluation of PSMA targeting AuNP based on Glu-Urea skeleton PSMA small molecule inhibitors

As a new prostate cancer biomarker, PSMA is considered the most significant target protein for specific immunolocalization imaging diagnosis and immunodetected therapy due to its good organ specificity, external segment epitopes of the cell membrane, and high expression in androgen-independent prostate cancer cells[27, 62]. A variety of probes targeting PSMA have been prepared, including monoclonal antibodies, peptides, aptamers, and small molecule compounds[30, 62-64]. PSMA small molecule inhibitors have high stability, short circulation half-life in vivo, and good tissue permeability, which are more advantageous in diagnosing PCa molecular imaging. Mainly include the following three categories: (1) phosphate, phosphonite, phosphonate, phosphoramide, and other derivatives; (2) mercapto, indole-mercapto, hydroxamic acid, sulfonamide derivatives; (3) urea derivatives[65]. Among them, radionuclide-labeled PSMA urea derivatives (containing glutamate-urea-x group) molecular probes have been reported in successful clinical trials[66]. Several strategies have been developed to achieve PSMA targeted prodrugs or nanoparticles in recent years, such as peptides, RNA aptamers, and monoclonal antibodies (mAbs)[33]. However, there are few reports on targeted nanoparticles prepared based on PSMA small molecule inhibitors. Based on the above, we used mercaptoundecanoic acid (MUA) as the spacer chain to obtain the high-density anchoring of AuNP surface with its -SH end, and at the same time, modified a PSMA small molecule inhibitors containing Glutamate-Urea skeleton at the carboxyl-terminal of MUA to construct PSMA targeted nanoparticles. The effects of targeting ligands of different lengths on the stability and targeting of nanoparticles were investigated to explore the feasibility of using PSMA small molecule inhibitors as targeting ligands to prepare PSMA targeted nanoparticles.

### 1.4.3. Oriented Coupling of Discrete Number of Antibody to AuNPs for targeted labeling cell

With the development of nanotechnology, active targeting nanoparticles are becoming more and more popular, where the targeted ligands on the surface can selectively bind the overexpressed antigens on the surface of the target cell. Antibodies are widely used in targeting ligands, and their targeting efficiency is closely related to the fixation direction[67].

Random immobilization of antibodies may lead to denaturation of proteins and block of active sites, so some or even all biological activities of the immobilized ligands may be directly affected by steric hindrance or change of active sites during immobilization[41]. In addition, some studies have pointed out that the tight irreversible (or reversible) binding of antibodies and the control of density can affect their targeting efficiency[68-70]. Although there have been studies investigating the impact on targeting efficiency by controlling the direction or density of the antibody or the stability of the connection, the strategy of orientated immobilization of discrete and precisely controlled numbers of targeted biomolecules on the surface of each NP is still largely missing. Importantly, it is not easy to find evidence of how the ligand affects the targeting efficiency of the nanoparticles. Here, we aim to construct a platform to explore the relationship between the antibody density on the surface of NP and the dependence in vitro and targeting efficiency in vivo. To this end, we utilized SNAP-tag technology to orient the coupling of the discrete number of targeting HER2 receptors scFv on the surface of AuNP, so that each AuNP surface is coupled with precisely one or two scFvs. In vitro and in vivo targeting experiments were conducted to elucidate the relationship between ligand density and targeting.

# 2. Study on iodine-labeled carrier for X-ray fluorescence imaging of cells

## 2.1. Introduction

Computer tomography (CT) scan uses X-rays as scanning light to take multiple pictures of different cross-sections and then combine these pictures into a complete three-dimensional image through a computer program while restoring the internal structure of the scanned object. CT scans have been widely used in clinical disease diagnosis, monitoring, and locating lesions[71-72]. Since many human body tissues are not visible on X-ray films, contrast agents are needed to "deepen" them. Non-ionic contrast agents containing iodine are mainly used in clinical practice[73-74]. The characteristic of iodine is that it is not transparent to X-rays, which can significantly increase the contrast between the tissue and the cavity, and make the image clearer, thereby helping the doctor make a more reliable diagnosis. Non-ionic contrast agents are relatively safe, and however, due to the large amount of drugs entering the blood in a short period (1 mL of contrast agent contains 500-760 mg of drugs)[75-76], they will not only bring a heavy burden to the kidney, may cause contrast nephropathy, but also easily cause allergic reactions, thyroid dysfunction, and other side effects[77]. Therefore, it is necessary to improve the efficiency of iodine labeling cells and reduce the dosage of iodine, thereby reducing side effects.

Based on this, the efficiency of different carriers to deliver iodine into cells was studied. We investigate the I delivery efficiency in cells of the labeled AuNPs, dextran and bovine serum albumin (BSA) preparing by using a small molecular 4-Iodobenzylamine hydrochloride (4IH) as iodine source and synthesized iodine-dopped AgI NPs, while iohexol (a contrast agent used in hospital) were used as control. We screened which carrier can bring as much as possible iodine into cells without killing cells via cytotoxicity, endocytosis, and exocytosis experiments.

## 2.2. Major reagents

| Name | Purity | Company |
| --- | --- | --- |
| hydrogen tetrachloroaurate (III) | ≥ 99.9% | Sigma aldrich |
| Sodium citrate | ≥ 99% | Sigma aldrich |
| Silver nitrate | ≥ 99% | Sigma aldrich |
| Sodium iodine | ≥ 99.5% | Sigma aldrich |
| poly(isobutylene-*alt*-maleic anhydride) | NA | Sigma aldrich |
| anhydrous tetrahydrofuran | ≥ 99.9% | Sigma aldrich |
| chloroform | ≥ 99% | Carl Roth |
| SH-PEG-CH$_3$O (2000 kDa) | NA | Rapp Polymer |
| 1-Ethyl-3-(3-dimethylaminopropyl) carbodiimide | ≥ 97% | Sigma aldrich |
| 4-Iodobenzylamine hydrochloride | ≥ 95% | Sigma aldrich |
| Carboxyl-dextran | NA | Sigma aldrich |
| IODO-Beads® Iodination Reagent | NA | Thermo Scientific |
| Bovine Serum Albumin | NA | Thermo Scientific |
| Sodium dodecyl sulfate | NA | Sigma aldrich |
| Coomassie (Bradford) Protein Assay Kit | NA | Thermo Scientific |
| Nitric acid | 67 wt% | Fisher Chemical |
| Hydrochloric acid | 35 wt% | Fisher Chemical |
| RPMI 1640 medium no phenol red | NA | Gibico |
| Fetal bovine serum | NA | Gibico |
| Penicillin/streptomycin | NA | Gibico |
| Phosphate buffered saline | NA | Gibico |
| 0.05% trypsin/EDTA | NA | Gibico |
| Nitric acid | 67 wt% | Fisher Chemical |
| Hydrochloric acid | 35 wt% | Fisher Chemical |
| Resazurin | ∼ 80% | Sigma aldrich |

## 2.3. Key instruments

| Name | Model | Company |
|---|---|---|
| Dynamic light scattering (DLS) | NANO ZS | Malvern |
| Transmission electron microscopy (TEM) | JEM-1400PLUS HC | JEOL, Germany |
| UV–Vis absorption spectrophotometer | Agilent 8453 | Agilent, USA |
| ICP-MS | 7700 Series | Agilent, USA |

## 2.4. Experiments and methods

### 2.4.1. Synthesis of iodine-loaded PMA-Au nanoparticles (PMA-Au-I)

#### 2.4.1.1. Synthesis of Hydrophilic AuNPs

The hydrophilic 25 nm AuNPs core was prepared based on the previously reported protocol[78]. First, we need to synthesis 18 nm AuNPs as the seed. 300 mL of sodium citrate (99%, Sigma Aldrich, no. W302600) (1.32 mM, 2 mmol, 8.0 eq) was added into a 500 mL three-neck round bottom flask that provided with a condenser and heated to boiling on a magnetic stirrer. After boiling 5 min, 3 mL of gold (III) chloride trihydrate (HAuCl$_4$, ≥ 99.9%, Sigma Aldrich, no. 520918) (25 mM, 0.375 mmol, 1.5 eq) solution was added into flask immediately and further kept boiling for another 10 min. In this process, the color change of the solution from light yellow to violet and finally to wine-red was observed, indicating the formation of gold nanoparticles coated with citrate (Cit-AuNP). Then, the solution was cooled down to 90 °C, secondly, 18 nm AuNPs solution as the seed to prepare larger diameter Cit-AuNPs. The solution should keep at 90 °C during the whole grow procedure. 2 mL of HAuCl$_4$ was added to the solution and stirred for 30 min, and this step was repeated twice. Then, 110 mL of AuNPs solution was extracted and filled 110 mL of Milli-Q water that contained 2 mL of 60 mM sodium citrate (0.12 mmol, 4.8 eq) to dilute the solution, which caused the system temperature to drop rapidly; therefore, the solution takes ca. 30 min to heat up to 90 °C. After that, the 2 mL HAuCl$_4$ solution was injected into the system three times at 30 min intervals as described above, the diameter of

22

25 nm AuNPs were obtained.

## 2.4.1.2. Synthesis of poly(isobutylene-alt-maleic anhydride)-graft-dodecyl (PMA)

The synthesis of the amphiphilic polymer, PMA, is the same as previously studied[79]. 3.084 g (20 mmol) of poly(isobutylene-alt-maleic anhydride) (average $Mw \sim$ 6000 g/mol of the whole polymer, Sigma, no. 531278) was dispersed in 100 mL of anhydrous tetrahydrofuran (THF, ≥ 99.9%, Aldrich, no. 186562) as far as possible by ultrasound in a 250 mL round bottom flask. Next, 2.70 g (15 mmol) of dodecylamine (DDA, ≥ 98%, Fluka, no. 44170) was added to a flask, and the mixture was heated up to 60 °C under stirring and reflux overnight. After that, the product was dried under reduced pressure by an evaporator. It was dissolved in 40 mL chloroform (≥ 99%, Sigma, no. 372978) and dried under reduced pressure. This step was repeated twice to remove residual THF. Finally, PMA was stored in 40 mL of chloroform (final concentration is 0.5M) for further use.

## 2.4.1.3. Phase transfer of Cit-AuNPs from water to chloroform

Citrate, as a ligand, is a relatively weak ligand, which is only physically absorbed on the surface of AuNPs[80], leading to irreversible aggregation of AuNPs in subsequent centrifugation, dialysis and other operations; thus, we need to use stronger ligand to replace citrate to ensure that AuNPs can keep stable in further processing. Polyethylene glycol (PEG), which reduces the absorption of non-specific proteins and enhance biocompatibility of nanoparticles, is a well-known ligand that can prolong the circulation time of nanoparticles in vivo[81-82]. In addition, sulfhydryl can form strong Au-S bond with Au atom[83], thus, the mercapto-PEG is usually employed as PEGylate of Cit-AuNPs. Herein, 2000 KDa SH-PEG-CH$_3$O (Rapp Polymer, no. 12750-40) was used by us to replace the citrate ligand to help AuNPs transfer to chloroform. Simply, SH-PEG-CH$_3$O was dissolved in Milli-Q water to obtain 100 mg/mL of PEG solution. Calculation amount of PEG added according to $C_{PEG}/C_{NP} = 3 \times 10^4$, it is note that the amount of PEG added is excess to ensure that the surface of each AuNP is capped enough PEG molecule (ca. 5-15 PEG per nm$^2$ of AuNP)[78]. Adjust the pH of the mixture to 8-9 with 2 M NaOH, and stirred at room temperature (RT) for at least 3 h.

After PEGylation, mixed the solution with 100 mL of chloroform containing DDA. DDA was added in excess according to formula: $C_{DDA}/C_{NP} = 13 \times 10^6$ to ensure that part or all of the PEG on the surface of AuNPs were replaced by DDA (DDA-AuNPs)[78]. The mixture was stirred quickly under magnetic stirrer at RT until all AuNPs were transferred to lower layer, chloroform phase. After that, the upper layer was trashed and the chloroform phase was collected to wash twice by centrifugation at 9000 rpm for 15 min to get residual DDA and PEG out.

### 2.4.1.4. Preparation of PMA coated AuNPs (PMA-Au NPs)

PMA stored in chloroform was added to DDA-AuNPs and mixed well at RT. Then, the mixture was placed on a rotary evaporator and dried under reduced pressure at 40°C to remove the solvent. This step was repeated three times to get a homogeneous polymer coating. For the last time dried, the film in the flask is dissolved in alkaline sodium borate buffer (SBB, 50 mM, pH 12) instead of chloroform. The obtained PMA-Au NPs were concentrated and washed three times with Milli-Q water by centrifugation at 11000 rpm for 15 min.

### 2.4.1.5. Synthesis of PMA-Au-I by labeling PMA-Au with iodine

Briefly, 1.24 mg of 1-Ethyl-3-(3-dimethylaminopropyl) carbodiimide (EDC, 6.45 mmol, Sigma Aldrich, no. E7750) dissolved into 25 nm 2 mL PMA-Au NPs (con.39.5 nM), stirring 5 min to activate the carboxyl group on the surface of PMA. Then, 0.4 mg of 4-Iodobenzylamine hydrochloride (4IH, 1.29 mmol, Sigma Aldrich, no.59528-27-7) dissolved into 1 mL PB buffer and added into mixture solution, and the solution was stirred at RT for 24 h. After that, the combined solutions are filled into a 3 kDa centrifuge filter tube (Sigma Aldrich, Amicon® Ultra-4 Centrifugal Filter Unit 3 kDa, no. UFC800324), washed 5 times with Milli-Q water (10 min, 8000 rpm) and concentrated.

### 2.4.2. Synthesis of iodine-loaded Dextran (Dex-I)

The synthesis of Dex-I was similar to the above. 100 mg of Carboxyl-dextran (MW: 12 kDa,

8.33 × 10$^{-3}$ mmol) dissolved in 10 mL PB buffer (pH 6.0), then 120 mg of EDC (62.60 mmol) was added into Dextran solution, stirring 5min at RT to mix well. 4IH (100 mg, 37.04 mmol) dissolved into 1 mL PB buffer and added into mixture solution, the mixture reacted at RT for 24h.  Next, Dex-I solution was washed via an ultrafiltration tube (Sigma Aldrich, Amicon® Ultra-4 Centrifugal Filter Unit 3 kDa, no. UFC800324) 5 times with Milli-Q water (10 min, 7000 rpm) to remove the unreacted 4IH.

### 2.4.3. Synthesis of iodine-loaded Bovine Serum Albumin (BSA-I)

The labeling of bovine serum albumin (BSA) is still carried out by the reaction of the carboxyl group on the protein with the amino group on 4IH through EDC. Firstly, 100 mg of BSA (1.50 × 10$^{-3}$ mmol, Sigma Aldrich, no. A8806) was dissolved with 15 mL MES buffer (50 mM, pH 6.0) (Sigma Aldrich, no. M8250). Secondly, 57.51 mg of EDC (0.15 mmol) dissolved in 0.5 mL MES buffer (50 mM, pH 6) was added right away into the BSA suspension. The carboxylic acid groups of BSA were activated by EDC through stirring the mixture by magnetic stirrer from time to time during 10 min incubation time at RT. Thirdly, 3 mL MES buffer contained 40.50 mg of 4IH was added into the solution and continued to be stirred at RT for 3 h to conjugate amino group on 4IH to BSA. Finally, the mixture transferred into a 10 kDa centrifuge filter (Sigma Aldrich, Amicon® Ultra-4 Centrifugal Filter Unit 10 kDa, no. UFC801008) to purify BSA-I, washed with Milli-Q water 5 times by centrifuge to ensure that all unreacted 4IH was removed.

### 2.4.4. Synthesis of AgI nanoparticles

### 2.4.4.1.  Synthesis of Hydrophilic AgI NPs

The synthesis of hydrophilic AgI NPs referenced previous Rie Makiura's work[84] and made some modifications to the synthesis process based on the research of Liu Dandan[85]. In particular, equimolar amount of AgNO$_3$ (Sigma Aldrich, no. 204390-10G) and NaI (Sigma Aldrich, no. 409286-10G) aqueous solution were prepared respectively. 109.50 mg of AgNO$_3$ dissolved in 10 mL MilliQ water (0.05 M) and 276 mg of NaI dissolved in 30 mL MiliiQ water (0.05 M). 100 mL mixed surfactant solution containing 2 mM Sodium dodecyl sulfate

(SDS, Sigma Aldrich, no. 436143-100G) and 1 mM Tween 20 (Sigma Aldrich, no. P1379-250ML) was also prepared. Then, the NaI solution was added to mixed surfactant solution and shaken gently for 5 min to mix well. The prepared AgNO$_3$ solution was slowly added into NaI with mixed surfactants dropwise with stirring in the dark. Holding for an hour, afterward, AgI NPs with yellowish opalescence was obtained. Then the solution was centrifuged to collect NPs, and NPs were washed with MilliQ-water two times to remove surfactant (9000 rpm, 15min).

### 2.4.4.2. Phase transfer of AgI NPs from water to chloroform

Ag$^+$ sites on the surface of AgI NPs[86], which can interact with thiol-containing molecules to form dative bonds to keep NPs stable[87]. It is also to maintain the same modification process with PMA-Au-I to compare the differences between endocytosis and exocytosis. The same procedure was carried out with before, after washing, the concentrated AgI NPs was redistributed in 50 mL MilliQ water, 200 µl of SH-PEG-CH$_3$O (MW: 2 kDa, 50 mg/mL) (Rapp Polymer, no. 12750-40) was added to the solution to PEGylation AgI NPs and stirring at RT in the dark for 4 h.

Next, the PEG-capped AgI NPs were mixed with 50 mL chloroform containing 0.2 M DDA and stirred overnight for phase transfer. It should be noticed that the whole process needs to keep in the dark. When all the AgI NPs were transferred to the chloroform phase, the upper water phase became colorless and transparent, and the organic phase containing nanoparticles in the lower layer was collected by a liquid separation funnel. The collected solution was centrifuged to remove excess DDA (9000 rpm, 15 min).

### 2.4.4.3. Preparation of PMA coated AgI NPs

1 mL of 0.5 M PMA and purified DDA-AgI NPs were added into 250 mL round bottom flask and gently shaken for 5 min to mix well. Then place the round-bottom flask on a rotary evaporator and reduce pressure to dry the solvent at 40°C. After being thoroughly dried, re-dissolve the film formed in the bottle in 50 mL chloroform and then dried again under reduced pressure to remove the solvent. This step was repeated three times to get a

homogeneous PMA coating on the surface of AgI NPs. Notice that after last time drying, instead of re-dissolving with chloroform, the film was dissolved by adding 20 mL of SBB buffer with pH 12. The bottle was allowed to stand overnight at room temperature to ensure that the membrane in the bottle was dispersed entirely in SBB buffer, and then the PMA-AgI NPs obtained was centrifuged via an ultrafiltration tube (Sigma Aldrich, Amicon® Ultra-4 Centrifugal Filter Unit 3 kDa, no. UFC800324) to replace the SBB buffer with MilliQ water and concentrated for subsequent experiments.

### 2.4.5. Characterizations of nanoparticles

### 2.4.5.1. Transmission electron microscopy

Transmission electron microscopy (TEM) of the PMA-Au NPs, PMA-Au-I and AgI NPs were obtained using a JEM-1400PLUS HC TEM (JEOL, Germany) at an acceleration voltage of 200 kV in the bright field image mode. Disperse 2 μL of PMA-Au NPs, PMA-Au-I and AgI NPs stock solution in MilliQ water in 2 mL of MilliQ water to dilute to a very light color, respectively, and dropped 10 μL of diluted solution onto an ultrathin carbon-coated copper TEM grid, dried it at RT and captured images by TEM.

### 2.4.5.2. Dynamic light scattering and zeta potential

The hydrodynamic diameters of PMA-Au NPs, PMA-Au-I and AgI NPs in solution were performed by dynamic light scattering (DLS) instrument (Malvern Zetasizer), as previously reported[78]. A UV-Kuevette, ZH 8.5 mm Deckel (Sarstedt, Germany) was used for the measurement, and the instrument is operated at 633 nm of He-Ne laser with a scattering angle of 173°. Basically, each sample was diluted 100 times with MilliQ water to a concentration of about 0.1 mg/mL. All samples were filtered using 0.2 μm filter membrane and allowed to equilibrate for 5 min at 25 °C. Place 1 mL sample into the sample cuvette and tap the cuvette to release bubbles before inserting into the instrument. Both of the hydrodynamic diameters expressed in terms of intensity and number were recorded. Each sample was measured three times to ensure the repeatability of the experiment, and data are provided as mean value ± standard deviation (SD).

The zeta-potential ζ of NPs at the distance of the electrostatic screening length was measured with laser Doppler anemometry (LDA). Usually, DLS devices can also be used for LDA testing, but it is worth noting that LDA measurements require a special potential cuvette to form electrodes to apply an electric field. Briefly, put 1 mL of the diluted sample ($C_{NPs}$: 0.1 mg/mL) into the potential cuvette, noting that the NP solution must be submerged over the electrode plate and ensure no bubbles in the cuvette. The zeta-potential ζ is taken as mean value ± standard deviation (SD) from the distribution function.

### 2.4.5.3. UV-vis absorption spectroscopy

UV-vis absorption spectroscopy is a simple and universal method for the characterization of colloidal nanoparticles. For that, PMA-Au NPs, PMA-Au-I, and AgI NPs were diluted with MilliQ water and placed 1 mL of them to the cuvette, and the absorption spectra wavelength from 300 nm to 800 nm was recorded with an Agilent 8453 spectrometer.

### 2.4.5.4. Concentration of BSA

The concentration of BSA of iodine labeled BSA (BSA-I) was determined according to the instructions of the Coomassie (Bradford) Protein Assay Kit (Thermo Scientific™, no. 23200). Firstly, the different concentrations of BSA solution required for the standard curve need to be prepared. Refer to Table 2-1 to prepare the standard solution of BSA. Dilute the content of one BSA standard (2 mg/mL) into several clean vials, using MilliQ water as the diluent. Secondly, equilibrate the Coomassie Reagent solution to room temperature, then mix 30 μL of standard curve solution or sample with 1.5 mL of Coomassie Reagent solution, and incubate at RT for 10 min. Thirdly, set the spectrophotometer to 595 nm and zero the background of the instrument with MilliQ water. Subsequently, put all the samples into cuvette and record the absorbance at 595 nm. The 595 nm measurement of the blank sample was subtracted from the 595 nm measurement of the other single standard sample and unknown sample. The standard curve was plotted by plotting the blank corrected mean 595 nm measurement of each BSA standard and its concentration (in μg/mL). The standard curve was used to determine the protein concentration of each unknown sample.

*Table 2-1.* *Preparation of diluted BSA standard solutions (working range is 100-1500 µg/mL).*

| Vial | Volume of diluent | Volume and source of BSA | BSA concentration |
|------|-------------------|--------------------------|-------------------|
| A | 0 | 300 µL of stock | 2000 µg/mL |
| B | 125 µL | 375 µL of stock | 1500 µg/mL |
| C | 325 µL | 325 µL of stock | 1000 µg/mL |
| D | 175 µL | 175 µL of vial B dilution | 750 µg/mL |
| E | 325 µL | 325 µL of vial C dilution | 500 µg/mL |
| F | 325 µL | 325 µL of vial E dilution | 250 µg/mL |
| G | 325 µL | 325 µL of vial F dilution | 125 µg/mL |
| H | 400 µL | 100 µL of vial G solution | 75 µg/mL |
| I | 400 µL | 0 | 0 µg/mL = blank |

### 2.4.5.5. Iodine concentration in the material measured by ICP-MS

All the prepared iodine-labeled compounds or nanoparticles were diluted 100 times with MilliQ water, and 20 µL of each sample were taken out into vials, respectively. Subsequently, the samples were digested with 180 µL of aqua regia (v/v, $HNO_3$ : HCl = 1:3) overnight. On the following day, the digested samples were diluted with 2 mL 2% HCl (35 wt%, Fisher Chemical, USA) and transferred to PFA tubes. Then, the prepared samples were tested for concentration by ICP-MS (Agilent 7700 Series, USA) with the argon gas as flow.

### 2.4.6. Colloidal stability of PMA-Au-I and AgI NPs in different media

To investigate the colloidal stability of the synthesized nanoparticles, we evaluated the stability of these two nanoparticles, PMA-Au-I and AgI NPs in different media, including MliiQ water, PBS, and RPMI 1640 medium containing 10% or 0% fetal bovine serum (FBS) (Thermofisher, no. A1049101). For that, the synthesized PMA-Au-I and AgI NPs were diluted to 2 mg/mL with fresh MilliQ water and filtered by a 0.22 µm filter membrane (Sigma Aldrich, no. GVWP04700). Thereafter, 500 µL of different media were mixed with the same volume of diluted NPs solution. The hydrodynamic diameter and UV absorbance of each sample at the specific time of 0 h and 24 h were characterized by DLS and UV-vis to evaluate the stability of NPs.

### 2.4.7. Cell culture

Human blood (leukemic T-cell lymphoblast) cell line Jurkat were provided by ATCC (Manassas, VA, USA) and cultured in Roswell Park Memorial Institute (RPMI) 1640 Medium (Thermofisher, USA) supplemented with 10% fetal bovine serum (FBS, Biochrom, Germany), 100 U/mL penicillin/streptomycin (P/S, Fisher Scientific, Germany) and 10% HEPES buffer (1 M, Thermofisher, USA). Cells were cultured in the incubator at 37 °C and 5% $CO_2$.

### 2.4.8. Cell viability assay

For the in vitro cell viability of Jurkat cells exposed with different iodine-labeled compounds and nanoparticles was evaluated with Resazurin assay as previously study[88]. Briefly, Jurkat cells were collected from cultured flask by centrifugation and cell suspension at a density of $2.4 \times 10^5$ was prepared with fresh medium. Then, different concentrations of iodine-labeled compound and nanoparticles (iohexol, BSA-I, Dex-I, PMA-Au-I and AgI NPs) based on iodine concentration were prepared with fresh cell medium. A series of exposure concentrations of Jurkat cells are shown in the Table 2-2. It is worthy to notice that Jurkat cells are suspended cells and cannot adhere to the wall. Still, when the cells need to be exposed to materials, the cells or culture medium cannot be taken out separately, so when preparing the cell suspension or exposure solutions, it needs to be prepared at a concentration that is twice the set concentration. 100 µL of the prepared cell suspension and exposure solution were respectively taken and mixed them in a 96-well plate (Sarstedt, Germany) with a growth area of 0.32 $cm^2$ per well and incubated for 24 h. After the expose time, cells were collected from each well into Eppendorf tubes and washed with phosphate buffered saline (PBS, Gibco, Invitrogen, Belgium) three times (0.2 mL per time). Resazurin stock solution was performed by dissolving resazurin salt (Sigma Aldrich, no. R7017) in PBS at a concentration of 0.2 mg/mL. The working concentration of the resazurin was obtained by mixing resazurin stock solution with fresh RPMI 1640 medium containing 10% FBS (v/v, 10:1). The washed cells were resuspended in 100 µL of resazurin working solution and re-placed in a new 96-well plate. The plate was incubated in an incubator at 37 °C for 4 h until the resazurin working solution turned pink. After that, each well of the fluorescence

spectrum of emission from 570 nm to 620 nm was collected by fluorescence meter (Fluorolog-3, Horiba Jobin Yvon, USA) with the excitation at 560 nm. The fluorescence absorption value at the wavelength of 585 nm was selected for cell viability analysis, and the following formula was used for calculation: $V\% = (V_{sample} - V_{blank}) / (V_{control} - V_{blank}) \times 100\%$. Experiments were performed in independent triplicates, each experiment was with different generations of cells and incubations were done on different days.

*Table 2-2. The concentration $C_I$ of iodine compound, iodine-labeled compounds and nanoparticles used in the cell viability assay. The concentrations are presented as mass concentration (mg/mL), molarity concentration (µmol/L) of the iodine.*

| sample | Concentration range | |
|---|---|---|
| | $C_I$ (mg/mL) | $C_I$ (µmol/L) |
| iohexol | $1.22 \times 10^{-4} - 64.00$ | $9.61 \times 10^{-1} - 5.04 \times 10^{5}$ |
| BSA-I | $1.56 \times 10^{-4} - 1.60 \times 10^{-1}$ | $1.23 - 1.26 \times 10^{3}$ |
| Dex-I | $9.76 \times 10^{-5} - 8.00 \times 10^{-1}$ | $7.69 \times 10^{-1} - 6.30 \times 10^{3}$ |
| AgI | $2.95 \times 10^{-5} - 1.21 \times 10^{-1}$ | $2.32 \times 10^{-1} - 9.53 \times 10^{2}$ |
| PMA-Au-I | $7.81 \times 10^{-6} - 8.00 \times 10^{-3}$ | $6.15 \times 10^{-2} - 63.00$ |

## 2.4.9. Cellular uptake study

As previously reported, iodine labeling efficiency in Jurkat cells exposed to iodine-compound, iodine-labeled compounds and nanoparticles were assessed by inductively coupled plasma mass spectrometry (ICP-MS, Agilent 7700 Series)[88-89]. Dilute the collected cells with fresh RPMI 1640 medium supplemented with 10% FBS into a cell suspension with a density of $3.6 \times 10^{6}$ cell/mL, and 1 mL of cell suspension was seeded in a 6-well plate (ThermoFisher, Germany) with a growth area of 9.6 cm$^2$ per well. Then, prepare expose solutions of twice the concentration series set as shown in the Table 2-2. Take 1 mL of the exposure solution of each concentration into a 6-well plate that has added 1 mL of cell suspension, gently shake the plate horizontally to mix the exposure solution and cells evenly, then put the plate in the incubator incubated at 37 °C for 24 h. After the exposure time, the cell solution in each well was transferred to labeled vials, respectively, and the exposure solution was discarded after centrifugation at 300 RCF for 5 min. Subsequently,

cells were washed three times with 1 mL PBS each time. Next, the cell pellet of each concentration was dispersed in 1 mL PBS respectively, and 10 µL of the cell suspension was diluted with PBS 10 times, then the cells of each concentration were counted with a cell counting chamber (Neubauer Chamber, Celeromics Technologies, Spain). The centrifugation was carried out again at 300 RCF for 5 min to get the cell pellets, which were further digested and prepared ICP samples. For that, after collecting the cell pellets, added 75 µL of $HNO_3$ (67 wt%, Fisher Chemical, USA) to each sample to lyse the cells overnight. On the second day, 150 µL of HCl (35 wt%, Fisher Chemical, USA) was added to digest overnight. Finally, completely digested samples were diluted with 2 mL of 2% HCl (35 wt%, Fisher Chemical, USA) and moved to PFA tubes prior at detecting the amount of iodine internalized in Jurkat cells by ICP-MS.

### 2.4.10.        Cell exocytosis study

To investigate the long-term labeling efficiency, intracellular retention of iodine-labeled materials, the amount of intracellular and extracellular iodine was assessed after Jurkat cells were exposed to iodine-labeled materials according to our group's previously published protocols[89]. Fresh RPMI 1640 containing 10% FBS was used to dilute the cells collected from the culture flask by centrifugation to a cell suspension with a density of 3.6 $\times 10^6$ cell/mL. Then, 1 mL of cell suspension was mixed with 1 mL of the prepared exposure solution, which was twice of the set exposure concentration, and placed into a 6-well plate with a growth area of 9.6 $cm^2$ per well. The 6-well plate was cultured at 37 °C with 5% $CO_2$ for 24h. The specific concentrations of the iodine compound, iodine-labeled compounds and nanoparticles used in the exocytosis assay are indicated in Table 2-3. At the end of exposure, the exposure solution was centrifuged at 300 RCF for 5 min to discard. Cells were washed three times with 1 mL fresh PBS to remove the iodine-labeling materials remaining in the culture medium as well as absorbed on the cell surface without being internalized by the cells. Cell pellets at every concentration of each material and supernatant after washing three times were collected and set as control (t=0 h). Note that extracellular iodine is not removed during the removal of the exposure solution and would be counted as exocytic iodine during the ICP-MS measurement. After that, the cells were re-suspended in 2 mL

fresh RPMI 1640 medium containing 10% FBS and placed into a new 6-well plate for further incubation at 37 °C and 5% $CO_2$ for 24 h, 48 h and 72 h. After the cell culture for the specific time was over, both of medium and cells in each well were transferred together to the labeled Eppendorf tubes of sample's name. The supernatant and cells were collected by centrifugation at 300 RCF for 5 min. The cells were dispersed in 1 mL of fresh PBS, and 10 µL of cell suspension was taken and diluted 10 times with 990 µL of PBS for cell counting using cell counting chamber (Neubauer Chamber, Celeromics Technologies, Spain). The processing of cell pellets for ICP-MS measurement is as described above, this part is the content of iodine that is still internalized by the cell and not secreted extracellularly after the desired time of incubation. The iodine content in the collected cell supernatant is as exocytosis fraction of iodine. Briefly, the 150 µL of supernatant was digested overnight with 150 µL of Aqua Regia, then samples were diluted with 1 mL of 2% HCl (35 wt%, Fisher Chemical, USA) and centrifuged at 9000 rpm for 5 min to remove the precipitate, and transferred to the PFA tube for ICP-MS detection. The results are expressed as the percentage of the mass of the exocytosis iodine ($m\_I_{exo}$) in the total mass of intracellular + supernatant iodine ($m\_I_{tot} = m\_I_{pel} + m\_I_{sup}$). Exocytosis experiments of iohexol, AgI NPs and BSA-I were conducted six times independently, and Dex-I and PMA-Au-I were conducted nine times independently.

**Table 2-3.** *The working concentration $C_I$ of iodine compound, iodine-labeled compounds and nanoparticles used in the exocytosis assay. The concentrations are presented as mass concentration (mg/mL), molarity concentration (mmol/L) of the iodine.*

| sample | Concentrations used | |
|---|---|---|
| | $C_I$ (mg/mL) | $C_I$ (mmol/mL) |
| iohexol | 4 | 31.50 |
| | 8 | 63.00 |
| | 16 | 126.00 |
| AgI NPs | 0.002 | 0.016 |
| | 0.004 | 0.032 |
| | 0.008 | 0.064 |
| BSA-I | 0.01 | 0.079 |
| | 0.02 | 0.16 |
| | 0.04 | 0.32 |
| PMA-Au-I | 0.00025 | 0.002 |
| | 0.0005 | 0.004 |
| | 0.001 | 0.008 |
| Dex-I | 0.0125 | 0.1 |
| | 0.025 | 0.2 |
| | 0.05 | 0.4 |

## 2.5. Results and discussions

### 2.5.1. Synthesize and characterization of different materials labeled with iodine

In this study, PMA-Au NPs with a diameter of 25 nm were synthesized as described in previous our group's work[78]. Simply put, according to Baster's modified protocol, gold nanoparticles with a diameter of 18 nm covered by citrate were first obtained as seeds. After that, 1 mL of 25 mM $HAuCl_4$ solution was added every 30 min, and the mixture was kept at 90 °C. The added Au (III) ions would continue to grow on the surface of seed AuNPs under the reducing action of sodium citrate until AuNPs with a diameter of 25 nm were obtained. The chemical reaction formula of sodium citrate to reduce gold salt is as eq 1. The Au NPs were transferred to the organic phase by phase transfer, and at the same time, the weaker ligand citrate was replaced with the ligand DDA which can form strong Au-S coordination bond with the gold surface. Then, PMA is used to coat the outer surface to obtain PMA-Au NPs that can be stably dispersed in water and has modifiable properties. Finally, 4IH was conjugated to PMA via EDC to achieve iodine labeling, and PMA-Au NPs

were performed as a delivery vehicle for iodine. Meanwhile, in order to evaluate which method has a higher iodine delivery efficiency, whether the iodine is labeled on the outer layer of the NP or the NP doped with iodine. Therefore, we synthesized AgI NPs and used the same method for phase transfer to obtain DDA-capped AgI NPs, and finally coated them with PMA.

$$n \cdot HAuCl_4 \text{ (aq)} + n \cdot (^-OCOCH_2)_2 \, C(OH)COO^-)(aq) \rightarrow 4n \cdot Cl^- \text{ (aq)} + 4n \cdot H^+ \text{ (aq)} + Au^0{}_n +$$
$$n \cdot (^-OCOCH_2)_2 \, CO(aq) + n \cdot CO_2 \, (\uparrow) \tag{1}$$
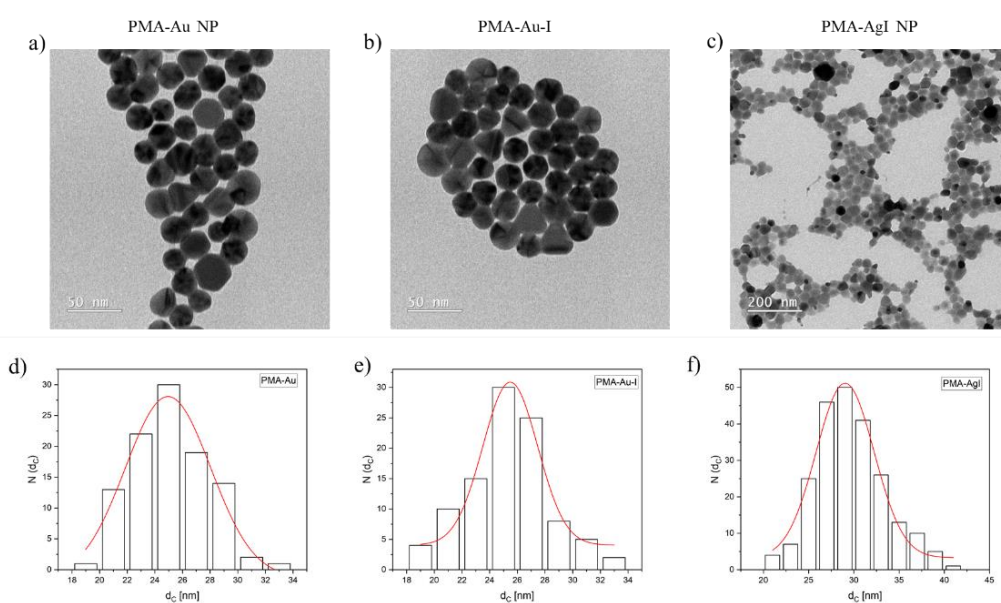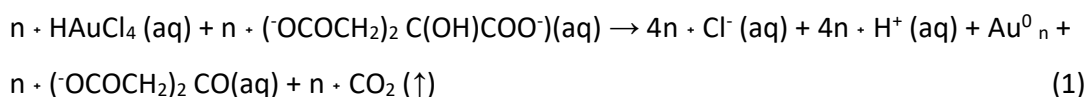


***Figure 2-1.*** *Representative TEM images of a) PMA-Au NPs, b) PMA-Au-I NPs and c) PMA-AgI NPs. TEM figures were captured by Dr. Marta Gallego Gonzalez form CIC BiomaGUNE. d)-f), the respective histogram of size distribution of inorganic core diameter $d_C$. The mean value $\pm$ standard deviation (SD) of a) PMA-Au NPs, b) PMA-Au-I NPs and c) PMA-AgI NPs were $d_c = 24.72 \pm 2.88$ nm, $24.99 \pm 3.53$ nm and $29.72 \pm 4.85$ nm, respectively.*

Firstly, the morphology of two NP was characterized by TEM. As shown in Figure 2-1a, b, c, both PMA-Au NPs and AgI NP are spherical in appearance. The inorganic core of PMA-Au NPs, PMA-Au-I and PMA-AgI NPs was 24.72 ± 2.88 nm, 24.99 ± 3.53 nm and 29.72 ± 4.85 nm, respectively. The corresponding histogram (Figure 2-1d, e, f) also showed that both two NPs have uniformly distributed granular diameters. In addition, hydrodynamic

diameter and particle size distribution are also commonly used to evaluate NP, which are usually obtained by using DLS measurement. The original results obtained by the DLS test are all calculated by light intensity. Therefore, the data read by the intensity distribution curve is the most original, and the other two (volume distribution and number distribution) are calculated based on it. Here, we use intensity distribution and number distribution to characterize its hydration dynamic diameter and distribution. As shown in Figure 2-2a, b, c, d and 2-3a, b, c, d, the hydrodynamic diameter of PMA-Au NPs, PMA-Au-I, AgI NPs and PMA-AgI NPs expressed by intensity distribution were $90.5 \pm 1.64$ nm, $98.7 \pm 2.75$ nm, $103.5 \pm 3.86$ nm and $141.1 \pm 2.85$ nm, respectively. And the number distribution of PMA-Au NPs, PMA-Au-I, AgI NPs and PMA-AgI NPs was $28.7 \pm 1.14$ nm, $29.1 \pm 2.75$ nm, $32.7 \pm 3.86$ nm and $35.8 \pm 2.85$ nm, respectively. The numerical values of number and intensity distribution are not consistent due to different calculation formulas. However, both intensity and number distribution showed one peak of two NPs, indicating that a narrow size distribution. PMA has a lot of active carboxyl groups, when the surface of NP was coated with PMA, the outer layer of NP would also be capped with the number of carboxyl groups, and the whole NP would show a negative charge. As shown in Figure 2-4a, b, the surface potentials of PMA-Au-I, AgI NPs were $-32.4 \pm 4.32$ mV and $-38.6 \pm 3.68$ mV, respectively.

The optical properties of PMA-Au NPs, PMA-Au-I, AgI NPs and PMA-AgI NPs were characterized by UV-Vis. Some of metal nanoparticles (i.e., AuNPs, AgNPs), due to plasma resonance, produce a characteristic peak in the ultraviolet absorption spectrum, and the change of size or composition would make the characteristic peaks shift. The UV absorption peak of PMA-Au NPs (Figure 2-5a) with a metal core of 25 nm is 525 nm, which is consistent with the UV absorption peak of PMA-Au-I (Figure 2-5b) with a metal core of the same size, which means that coupled of 4IH containing iodine to the outer PMA does not effect on its optical properties. Similarly, the UV absorption peak of AgI NPs before and after PMA coating did not change, which was 423 nm. The UV results coincided with the results of TEM and DLS.

In order to investigate the effects of materials with different properties on the efficiency of iodine delivery, we also used 4IH, a small molecule containing iodine, and labeled it with

protein (BSA) and sugar (dextran). In addition, iohexol, a contrast agent used in hospitals, was used as a control. Therefore, we used the amino groups contained in BSA, amino-containing dextran and carboxyl-containing 4IH to carry out an amide reaction through EDC to synthesize iodine-labeled BSA and dextran, which were BSA-I and Dex-I. We also performed DLS and UV detection on the other three compounds, BSA-I, Dex-I and iohexol, as part of their characterization. Iohexol is a small molecule with a molecular weight of 821.138 and is soluble in water. Dextran is a polymer of glucose, a viscous substance similar to starch and dextrin produced by microorganisms. In this study, carboxyl group dextran with a molecular weight of 12,000 Dalton was used. These two compounds cannot self-assemble in water, so they cannot be veracious DLS test (Figure 2-2e, f and Figure 2-3e, f). The ζ potential of iohexol and Dex-I were -1.1 ± 1.16 mV and -5.7 ± 1.35 mV (Figure 2-4c, d). BSA is a globulin with a molecular weight of about 66.5 kDa and a large number of amino and carboxyl residues on the surface. BSA would give a size at 8.15 nm via DLS (Figure 2-2g and Figure 2-3g). The ζ potential of BSA-I was 1.41 ± 2.37 mV (Figure 2-4e). In addition, iohexol, Dex-I and BSA-I were characterized by UV-Vis to obtain ultraviolet absorption spectrum. The results showed in Figure 2-5e, f, g, iohexol and Dex-I have a significant absorption before 350 nm wavelength, but no characteristic peak appears. There is a maximum absorption peak at 595 nm for the BSA-I.
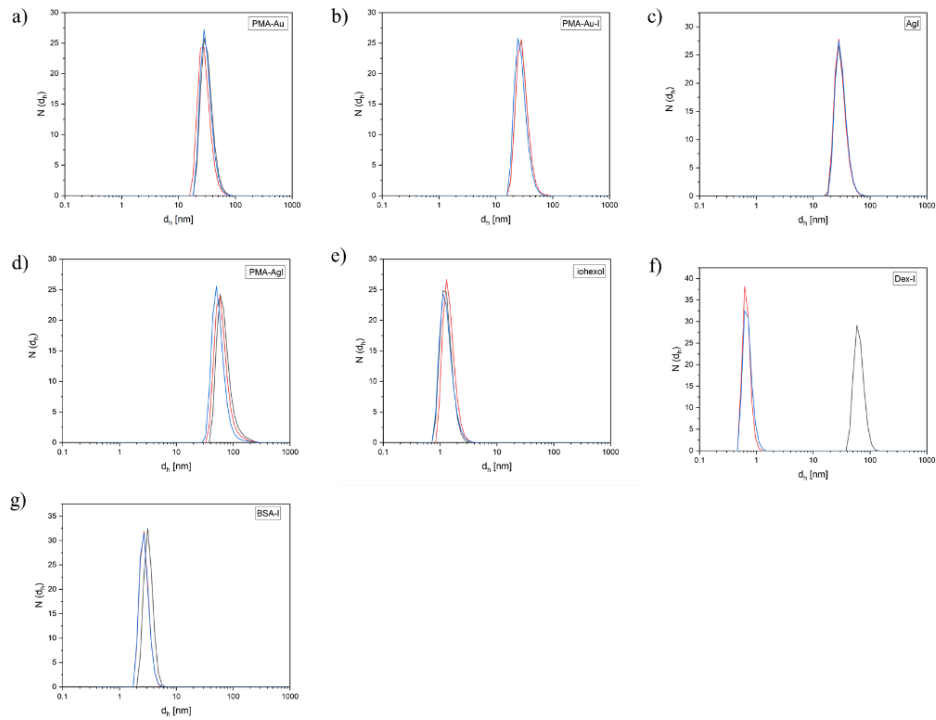
***Figure 2-2.*** *Number hydrodynamic distribution N(dₕ) of the hydrodynamic diameter dₕ of a)*
*PMA-Au NPs, b) PMA-Au-I, c) AgI NPs, d) PMA-AgI NPs, e) iohexol, f) Dex-I, g) BSA-I.*
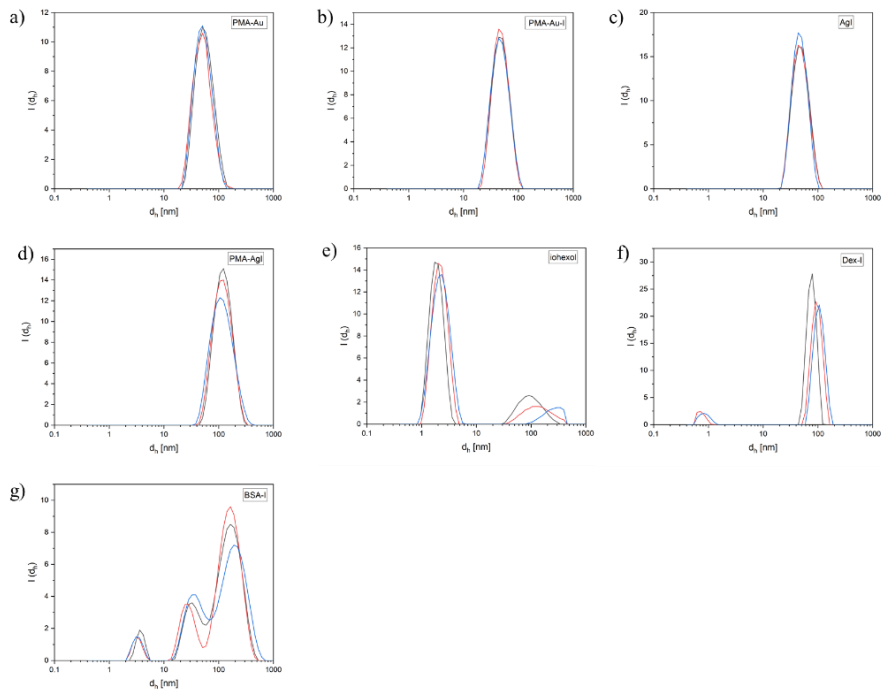


***Figure 2-3.*** *Intensity distribution I(dₕ) of the hydrodynamic diameter dₕ of a) PMA-Au NPs,*
*b) PMA-Au-I, c) AgI NPs, d) PMA-AgI NPs, e) iohexol, f) Dex-I, g) BSA-I.*
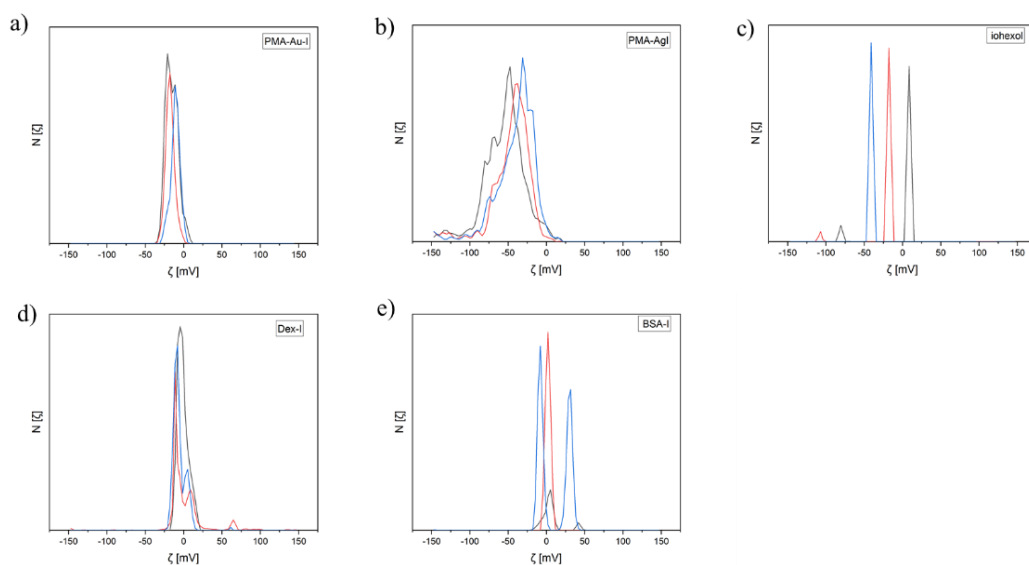
***Figure 2-4.*** *ζ potential distribution N [ζ] of a) PMA-Au-I, b) PMA-AgI NPs, c) iohexol, d) Dex-I, e), BSA-I.*
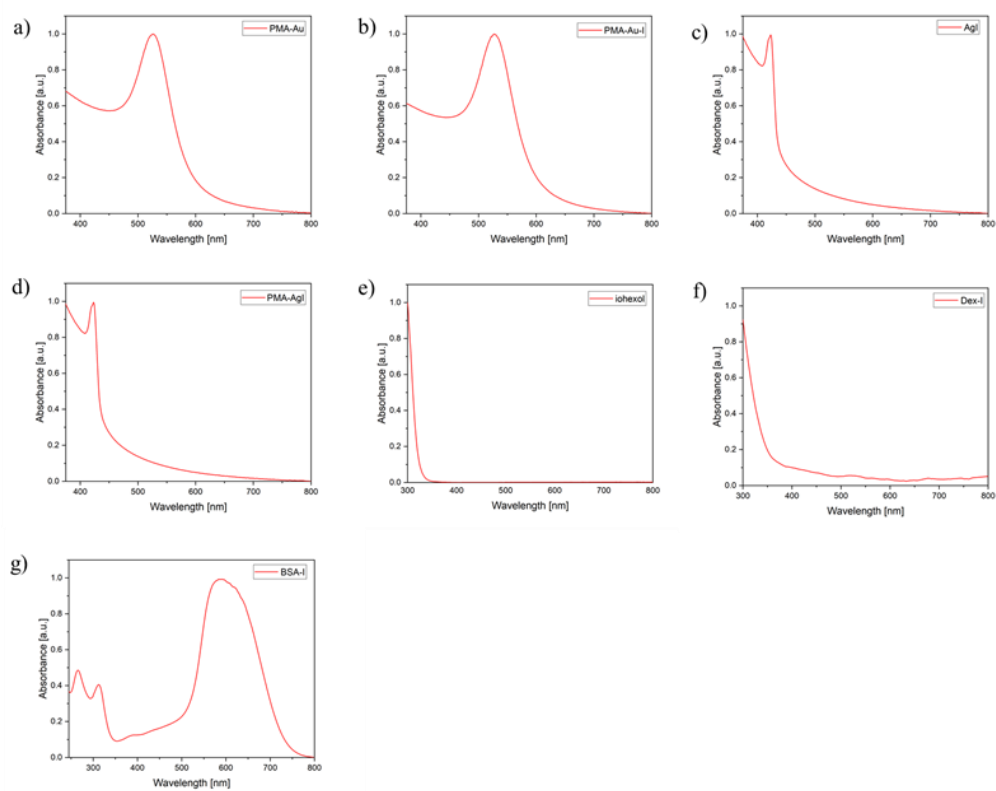


***Figure 2-5.*** *UV-Vis spectra of a) PMA-Au NPs, b) PMA-Au-I, c) AgI NPs, d) PMA-AgI NPs, e) iohexol, f) Dex-I, g) BSA-I.*

## 2.5.2. Determination of iodine concentration in each compound

The concentration of iodine in each compound can be quantified by ICP-MS. ICP-MS is an inorganic multi-element analysis technology that uses inductively coupled plasma as an ion source and mass spectrometry for detection. Before the samples enter the instrument for detection, it needs to be completely digested with strong acid to ensure that the substance to be measured in the form of aerosol or gas into the high-frequency electric field, and form ions under the action of the rapidly changing electric field, $M \rightarrow M^+$. The measured iodine content in each compound is shown in Table 2-4. Iohexol was purchased from UKE hospital and the concentration of iodine was 300 mg/mL. Among them, PMA-Au-I has the lowest iodine labeling efficiency, with a labeling rate of only 0.07, which means that each AuNP surface is labeled with less than one iodine molecule. AgI NPs are silver-doped iodine nanoparticles with a molar ratio of iodine to the silver of 0.61. The molar ratio of iodine to dextran in Dex-I is 2.87, which means that each dextran is labeled with 2.87 iodine molecules. BSA uses EDC method to covalently labeled iodine molecules on BSA, with a labeling efficiency of 4.19. BSA has the highest labeling efficiency, with an average of 4 iodides per BSA molecule.

**Table 2-4.** *The content and proportion of iodine in each compound. The $C_I$ is presented as mass concentration (mg/mL) and millmolarity concentration (mM) of the iodine. The $C_C$ is presented as mass concentration (mg/mL) and millmolarity concentration (mM) of the carrier (i.e., BSA, dextran, Au, Ag).*

| sample | $C_I$ (mg/mL) | $C_I$ (mM) | $C_C$ (mg/mL) | $C_C$ (mM) | $C_I$ /$C_C$ |
|--------|---------------|------------|---------------|------------|--------------|
| Dex-I | 2.53 | 19.92 | 83.3 | 6.94 | 2.87 |
| AgI NP | 17.84 | 140.47 | 24.69 | 230.74 | 0.61 |
| PMA-Au-I | 0.35 | 2.76 | 7.37 | 37.41 | 0.07 |
| BSA-I (EDC) | 1.26 | 9.92 | 157.52 | 2.37 | 4.19 |
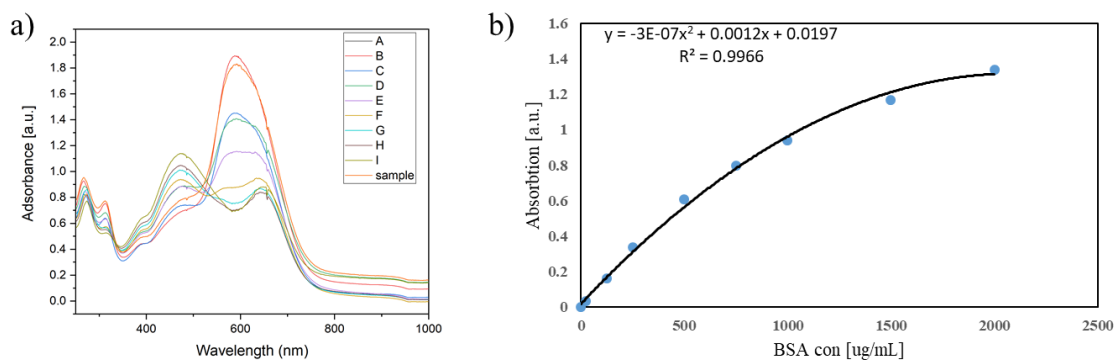
*Figure 2-6.* *a) UV-Vis spectra of standard curves of different concentrations of BSA, and b) the corresponding curve formula.*

### 2.5.3. Stability test of PMA-Au-I and AgI NP

The stability of nanoparticles is inseparable from their effective cellular uptake rate. To this end, we evaluated the stability of PMA-Au-I and AgI nanoparticles in different media, including MilliQ-water, PBS and complete cell culture medium (containing 10% FBS). The stability of nanoparticles was evaluated by the change of UV absorption spectrum and particle size at different time points in different media. Both synthesized AgI NP and PMA-Au-I can keep stable in water, which can be verified from the number distribution and intensity distribution of the two kinds of NP DLS (Figure 2-7, 2-8, 2-9, 2-10) that the hydrodynamic diameter didn't change within 24 h. The complete coincidence of the UV absorption spectra of AgI NP and PMA-Au-I (Figure 2-11) in water at 0 h and 24 h also confirms this fact. As we all know, the biological behavior of colloidal particles depends not only on their stability in water but also on, more importantly, their stability in a solution that simulates the environment in vivo (i.e., cell culture medium)[90]. Because of its complex buffer composition and abundant protein, which is closer to the cell growth environment. As shown in Figures 2-7, 2-8, 2-9, 2-10, 2-11, AgI NP and PMA-Au-I remain stable in the RPMI 1640 medium containing 10% FBS, and the size of both has no significant change compared with that in water. Moreover, the UV absorption peaks of both NP at 0 h and 24 h have no change, demonstrating that they were stable in the cell medium and suitable for in vitro labeling of cells. However, in a high-concentration salt solution such as PBS, since the charge of electrolyte would neutralize the surface charge of NP, if most of the charge carried by the surface of the NP is neutralized, the stabilization of the colloidal charge is destroyed, and the NP are prone to aggregation. The poor reproducibility of the quantitative distribution of AgI NP hydration dynamic diameter indicates that its stability in

41

PBS is not very good. When PMA-Au-I uses PBS as the medium, the broadening of the UV absorption peak also shows that it aggregates in PBS.
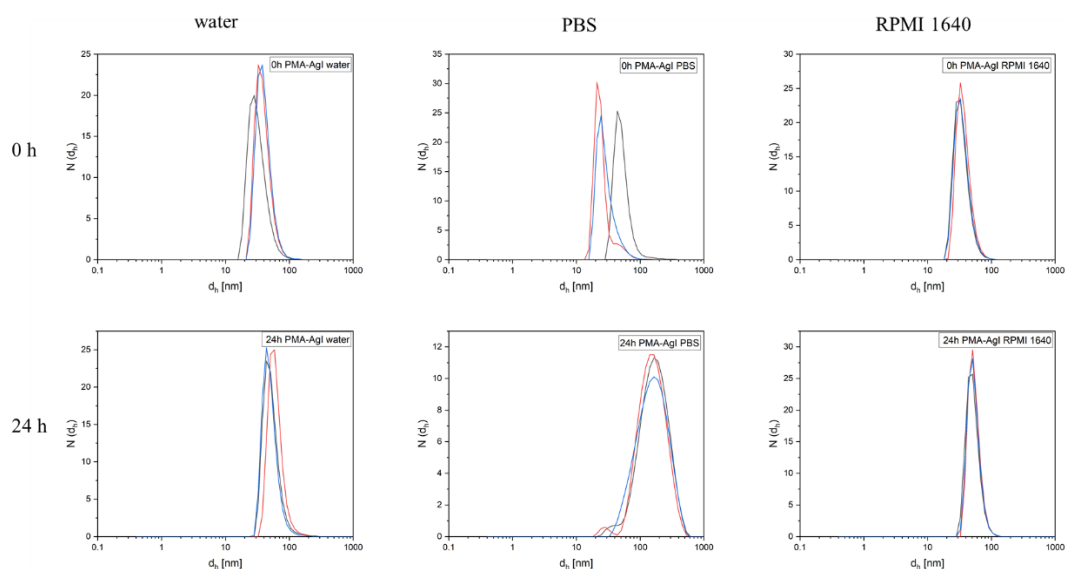


*Figure 2-7.* *At 0h and 24 h, number hydrodynamic distribution $N(d_h)$ of the hydrodynamic diameter of AgI NP in MilliQ-water, PBS and RPMI 1640 (supplement 10% FBS).*
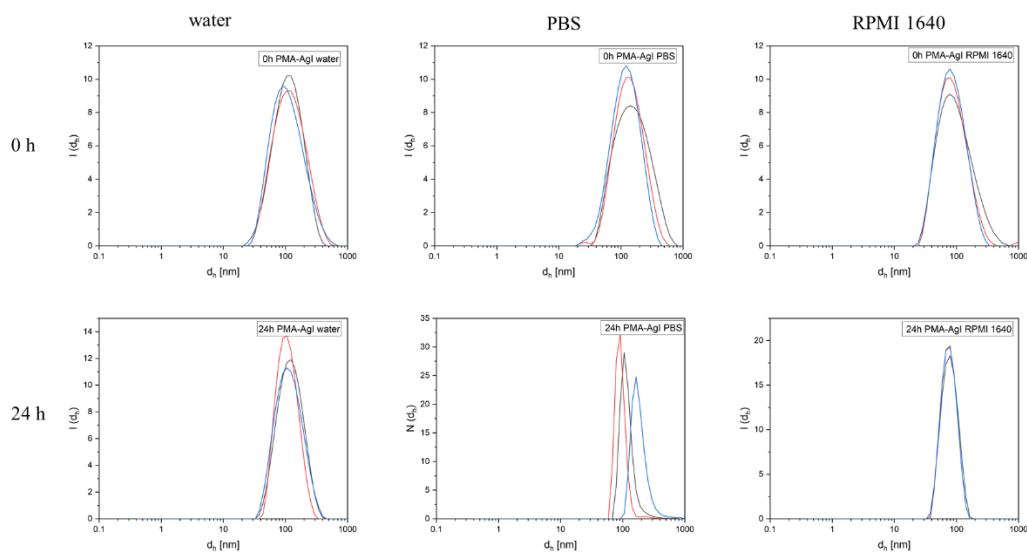


*Figure 2-8.* *At 0h and 24 h, intensity hydrodynamic distribution $I(d_h)$ of the hydrodynamic diameter of AgI NP in MilliQ-water, PBS and RPMI 1640 (supplement 10% FBS).*
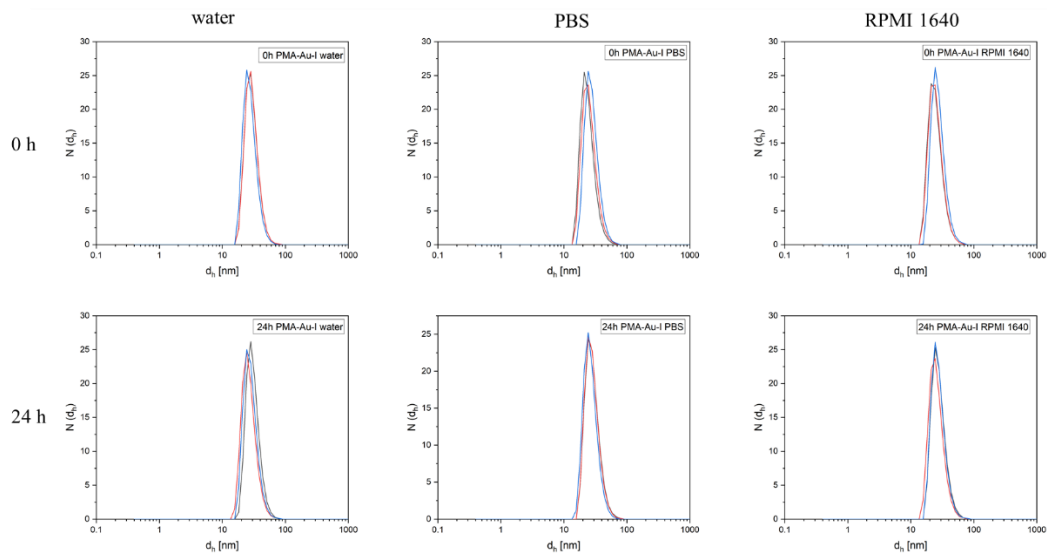
***Figure 2-9.*** *At 0h and 24 h, number hydrodynamic distribution N(d_h) of the hydrodynamic diameter of PMA-Au-I in MilliQ-water, PBS and RPMI 1640 (supplement 10% FBS).*
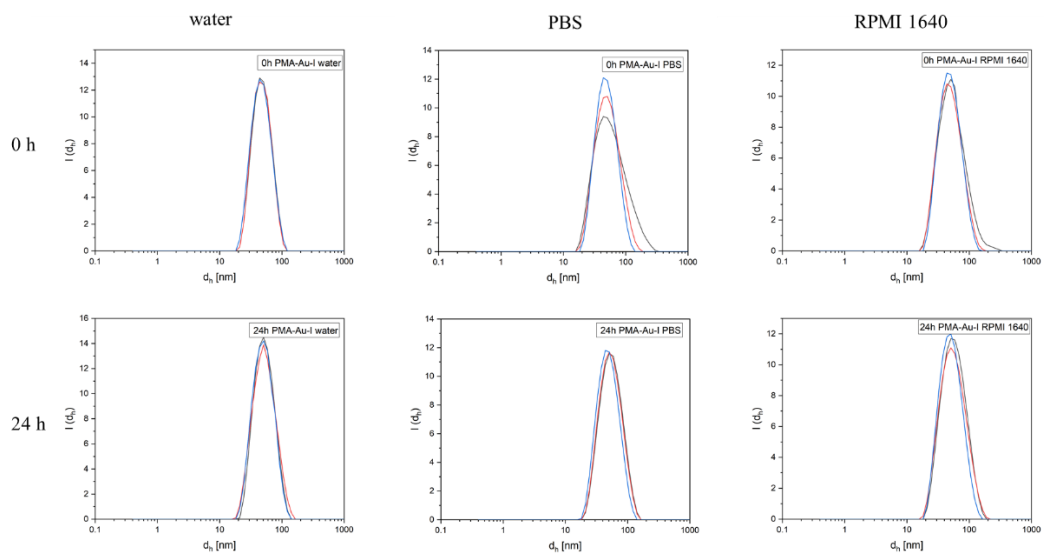


***Figure 2-10.*** *At 0h and 24 h, intensity hydrodynamic distribution I(d_h) of the hydrodynamic diameter of PMA-Au-I in MilliQ-water, PBS and RPMI 1640 (supplement 10% FBS).*
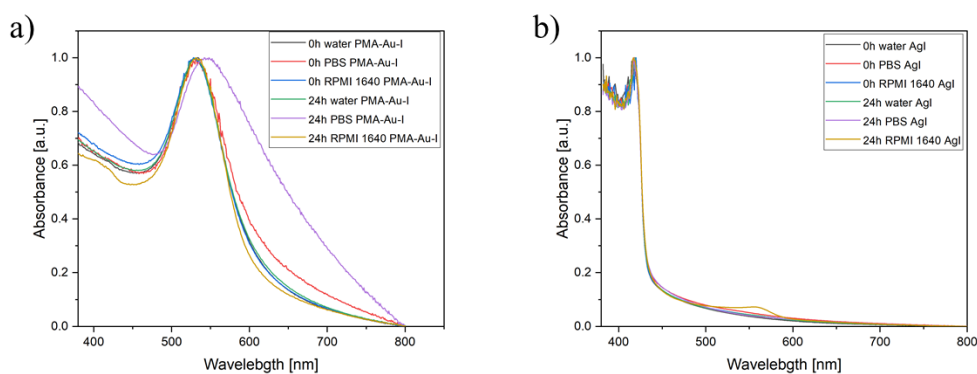
**Figure 2-11.** *At 0h and 24 h, UV-Vis spectrum of PMA-Au-I and AgI NP in MilliQ-water, PBS and RPMI 1640 (supplement 10% FBS).*

### 2.5.4. Cell viability assay

The toxicity of the compound to cells determines when it is used for treatment or diagnosis. Here, we used an acute T-cell leukemia cell line, Jurkat cells, to evaluate the toxicity of various materials in vitro. The resazurin assay, as well known as the Alamar Blue assay. Living cells with metabolic activity can reduce non-fluorescence resazurin to resorufin, which possess strong fluorescence, while dead cells cannot[91]. The stock resazurin solution was diluted with RPMI 1640 to a final working concentration of 0.02 mg/mL, and incubated with cells, which were exposed to different concentrations of different materials for 24 h, for 3-4 h until the solution turned pink. The viability rate of the cells can be obtained by comparing with blank and untreated cell groups. As shown in Figure 2-12, none of materials showed cytotoxicity at low concentrations. Among them, iohexol showed (Figure 2-12a) the best performance, the concentration of non-cytotoxic up to 32 mg/mL, until the concentration increased to 64 mg/mL, the cell viability decreased to 35.00 ± 2.88%. Furthermore, Dex-I showed lower toxicity, which was cytotoxic when the concentration was above 0.1 mg/mL, and the cell viability was 89.02 ± 2.88% when the concentration was 0.1 mg/mL. While the concentration of Dex-I is higher than 0.1 mg/mL, Dex-I exhibits cytotoxicity, which may be caused by the toxicity of dextran, because the corresponding concentration of dextran is about 3.3 mg/mL. This is consistent with previous reports that when dextran is lower than 3 mg/mL, it has no cytotoxic effect on normal human dermal fibroblasts[92].

44
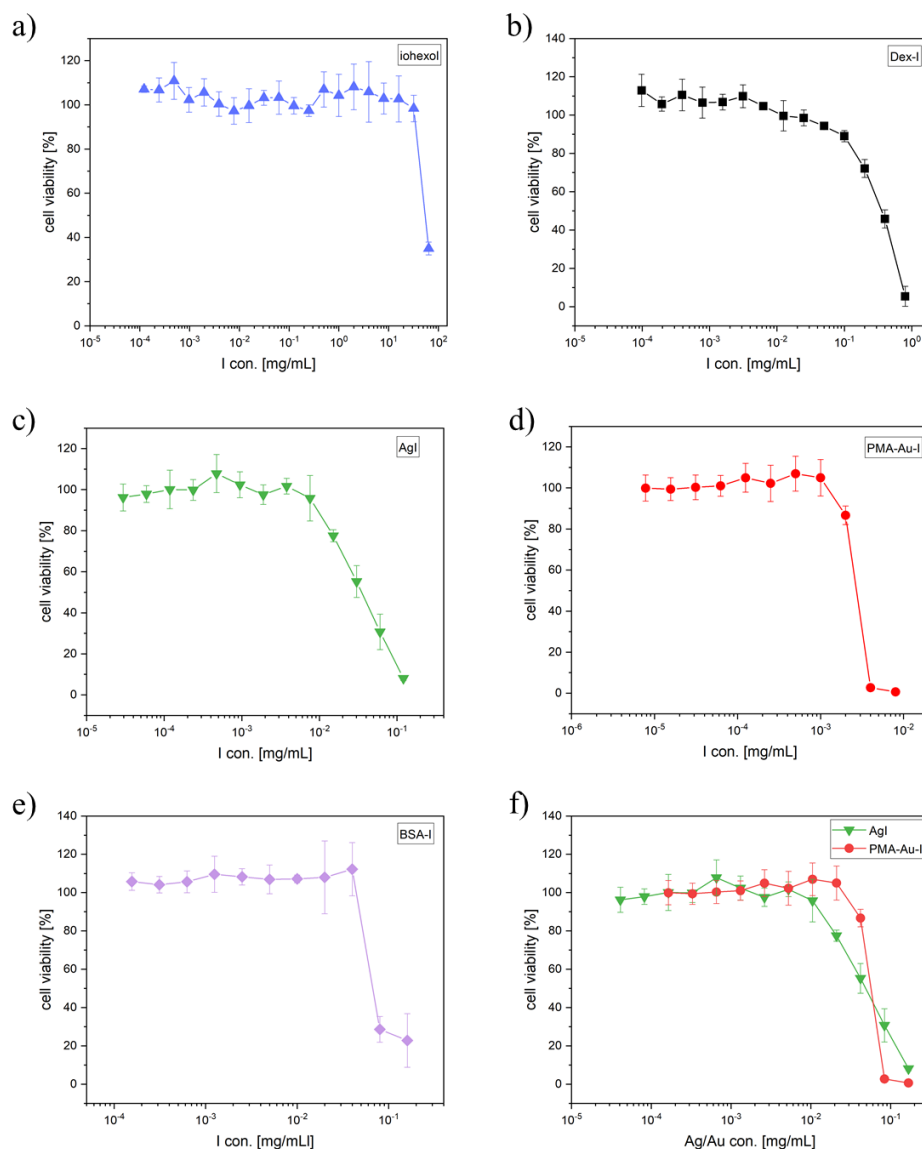
***Figure 2-12.*** *Cell viability of Jurkat cell after exposed to a) iohexol, b) Dex-I, c) AgI, d) PMA-Au-I, e) BSA-I for 24h in RPMI 1640 medium as measured by resazurin assay. f) The cell viability of AgI NP and PMA-Au-I was compared at the same concentration of Ag or Au. Cell viability was expressed as the fluorescence intensity of cells incubated with different compounds normalized to that of untreated control cells. Results are showed as percent cell viability [%] (mean) ± standard deviation (s.d.) from 3 independent experiments (n=3).*

BSA is a non-toxic protein, but it possessed cytotoxic after being labeled with iodine. BSA-I showed relatively high cytotoxicity. When the concentration was lower than 0.04 mg/mL, the cell viability was higher than 100%, while the concentration was 0.08 mg/mL, the cell viability

decreased sharply, only 28.64 ± 6.68%. The two kinds of NPs, AgI NP and PMA-Au-I, showed higher cytotoxicity when combined with iodine due to their inherent cytotoxicity. Although the cytotoxicity of AgNP was higher than that of AuNP[93], PMA-Au-I showed higher cytotoxicity than that of AgI NP because the iodine molecule was labeled on the surface coating polymer of AuNPs and the labeling efficiency was much lower than that of doped nanoparticles, AgI NP. AgI NP showed cytotoxicity at a concentration of 0.03mg/mL and the cell activity were 55.26 ± 7.73%. In comparison, PMA-Au-I showed cytotoxicity at a concentration of 0.004mg/mL and the cell activity were 2.73 ± 1.32%.

### 2.5.5. Cell uptake study

The intracellular accumulation is essential for judging whether the compound is suitable for *in vitro* cell labeling. It is well known that the more iodine is internalized into cells, significantly above the detection line, the easier it is to analyze the amount of iodine in each cell, and iodine-loaded materials are potential candidates. In order to screen out the most suitable materials for carrying iodine, we investigated the cellular uptake of different iodine-labeled materials under a series of concentrations, and the concentration settings were the same as the cell viability test. The uptake of external substances by cells is mainly carried out through endocytosis. Endocytosis refers to the process of forming vesicles through the invagination of the plasma membrane of the cell, wrapping and importing external substances into the cell. It is a way of transporting substances by the plasma membrane of the cell. According to the size, material state, and degree of specificity of the input, endocytosis is generally divided into three types: phagocytosis, pinocytosis, and receptor-mediated endocytosis[94].

After cells were exposed to iodine labeling materials with different concentrations for 24h, cells were collected and counted, and then the concentration of iodine in the cell pellet was quantified by ICP-MS to obtain the mass of internalized iodine in each cell. The exposure concentration of all materials is determined by the concentration of iodine in the material. All materials, except PMA-Au-I, showed concentration-dependent endocytosis, that is, the higher the concentration, the more iodine internalized in the cell, as shown in Figure 2-13. Combined with the results of previous cell viability, PMA-Au-I has no significant changes in endocytosis

within a safe concentration range (Figure 2-13d). When the iodine concentration in PMA-Au-I is 0.002 mg/mL, the amount of iodine in each cell is $0.00204 \pm 0.0004$ pg. While the exposure concentration of iodine is $9.75 \times 10^{-7}$ mg/mL, the amount of iodine in each cell is $0.00299 \pm 0.0007$ pg. Iodine-containing molecules are labeled on the PMA polymer in the outer layer of PMA-Au nanoparticles by an amide reaction with a labeling efficiency of about 0.07 iodine per nanoparticle, and the amount of iodine atoms per nanoparticle is much lower than the number of gold atoms. In addition, considering that high concentrations of gold nanoparticles can cause damage to the cells[95], so the exposed iodine concentration is lower, which is one of the possible reasons for the lower endocytosis of the cells. The endocytosis of gold nanoparticles by cells is limited, contributing to the lower efficiency of iodine internalization. In addition, the performance of dextran as a carrier for delivering iodine is also unsatisfactory. Within the entire working concentration range, the cellular uptake of Dex-I was not significantly different from the corresponding concentrations of PMA-Au-I NP and iohexol. When the lowest working concentration of Dex-I is $9.80 \times 10^{-5}$ mg/mL, the content of iodine in each cell is $0.0008 \pm 0.0005$ pg, and when the cells are exposed to the highest concentration of Dex-I, the cell uptake is $0.045 \pm 0.0032$ pg. The low uptake rate of Dex-I by cells may be due to the low labeling rate of iodine. Each dextran is labeled with about 3 iodine molecules.

Compared to PMA-Au-I, the iodine-doped AgI NP performed much better. Endocytosis of AgI NP at the highest concentration (iodine concentration 0.121 mg/mL) could reach $44.94 \pm 1.79$ pg per cell, which is much higher than the endocytosis of iohexol ($0.019 \pm 0.006$ pg per cell) at the same concentration, as shown in Figure 2-13a, c, f, but the toxicity is far greater than that of iohexol. However, within the safe concentration range (less than 0.0151 mg/mL), the endocytosis of AgI ($0.726 \pm 0.062$ pg per cell) is still the highest among all materials, much higher than the commercially available contrast agent iohexol ($0.0024 \pm 0.0006$ pg per cell). When the AgI concentration is lower than 0.00024mg/mL, the endocytosis of the cells is the lowest and reaches the plateau, which is $0.0136 \pm 0.0002$ pg per cell. The above results indicate that using iodine-doped nanoparticles maybe is a promising way to deliver as much iodine as possible into cells.
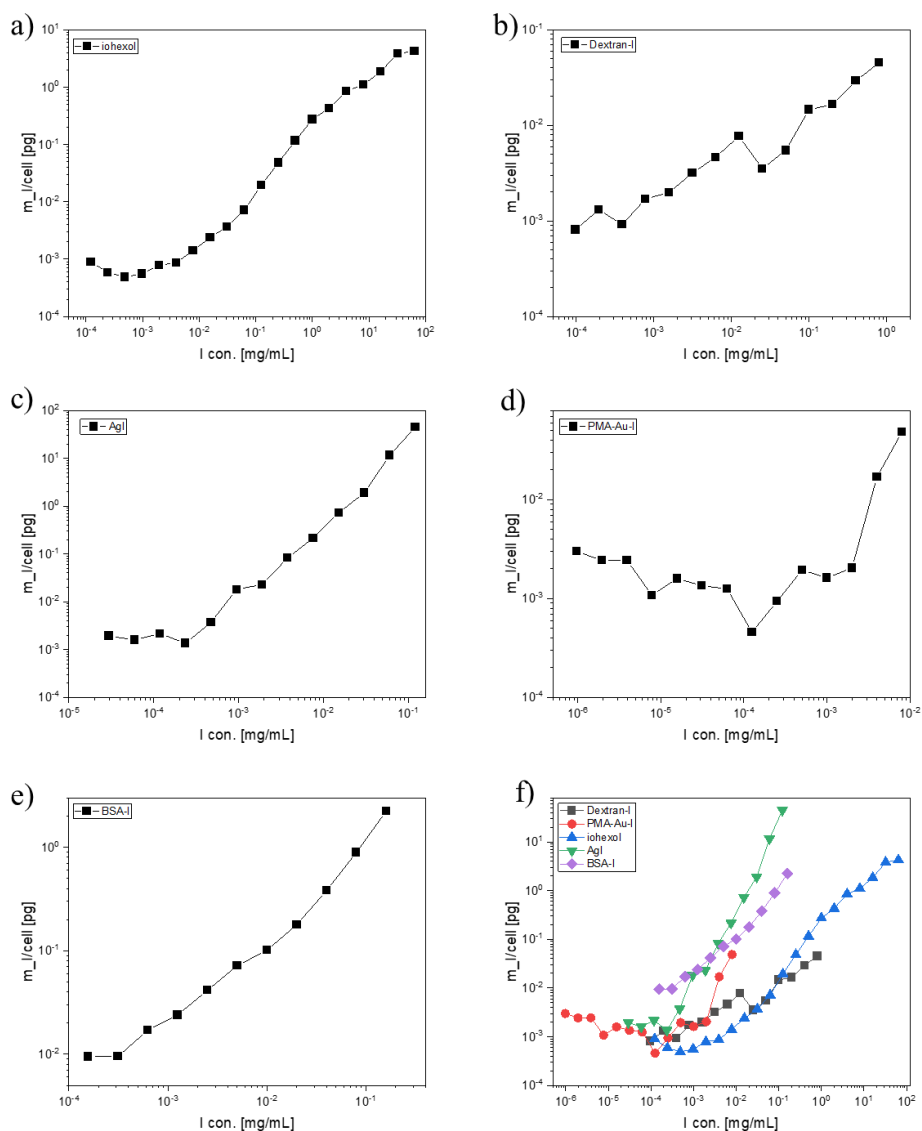
***Figure 2-13.*** *Cell endocytosis of Jurkat cell after exposed to different concentration of a) iohexol, b) Dex-I, c) AgI, d) PMA-Au-I, e) BSA-I for 24h in RPMI 1640 medium as measured by ICP-MS. f) The summary of endocytosis of iodine in different materials. X-axis refer to I concentration. Results are showed as percent cell viability [%] (mean) ± standard deviation (s.d.) from 3 independent experiments (n=3). Error bars are omitted for clarity and presented as average value. The ICP-MS was operated by our groupmate Yang Liu, and data was collected and analysis by myself.*

The next best performer in cellular endocytosis was iodine-labeled BSA, BSA-I. The variation of their cellular endocytosis showed a strong linear relationship with the variation of BSA-I

concentration. In the whole concentration range, the endocytosis of BSA-I was higher than that of the other three materials, PMA-Au-I, Dex-I and iohexol, which was comparable to the endocytosis of AgI NP in the same concentration range (Figure 2-13f). At the highest concentration of BSA-I, 0.16 mg/mL, the endocytosis of iodine is $2.23 \pm 1.26$ pg per cell, but the cell viability at this concentration is only 18%. This may be since the properties of BSA have changed after being labeled with iodine. Compared with BSA, it has higher cytotoxicity. This may be subject to a follow-up investigation. The maximum concentration within the safe range, 0.04 mg/mL, the amount of iodine in each cell is $0.38 \pm 0.18$ pg. Although it is significantly lower than the endocytosis of AgI NP at the same concentration, it is almost 70 times the endocytosis of iohexol. Notably, even with BSA-I at the lowest concentration of $1.6 \times 10^{-4}$ mg/mL, the amount of iodine per cell was $0.0095 \pm 0.0071$ pg, which was significantly higher than that of the other four materials and approximately four times greater than the amount endocytosed of AgI NP.

### 2.5.6. Cell exocytosis study

As a delivery vehicle for contrast agent iodine and delivering as much iodine as possible into the cell, it must also be able to stay in the cell for a long time to complete the subsequent X-ray fluorescence imaging. In order to examine the ability of candidate carriers to retain time in cells, we performed exocytosis of each material at different time points at 24, 48, and 72 h. Exocytosis is the opposite process of endocytosis. Cells will discharge small or large molecules in the cell through vesicles and fusion with the cell membrane, and release them into the extracellular matrix. The amount of iodine remaining in the cell can be obtained by detecting the concentration of iodine outside the cell, such as in the culture medium. Three of the safe concentrations were selected to investigate the exocytosis of each vector in the cell. After the cells were exposed to the carrier for 24 hours, the iodine concentration in the supernatant and the cell pellets were detected after 24, 48, and 72 hours of continue cultured. The amount of iodine within 24 h after cell exposure is used as the start of the exocytosis experiment, that is, t=0, the mass of iodine in the cell pellet should correspond to that of iodine at the corresponding concentration in the endocytosis experiment. As shown in Figure 2-14, this hypothesis has also been verified the

iodine endocytosis of the four materials iohexol, AgI NP, PMA-Au-I and BSA-I when t=0 is consistent with the corresponding endocytosis results. As shown in Figure 2-14b, the endocytosis of Dex-I exocytosis is inconsistent with previous endocytosis experiments, which may be caused by the low concentration of iodine in the cells and significant errors in detection.

Next, the amount of iodine of intracellular and extracellular after 24, 48 and 72 h of exocytosis was investigated to compare the intracellular retention capacity of each vector. In terms of changes in iodine amount in the cell pellet (Figure 2-15), iohexol showed the most rapid decrease at both high and low concentrations in Figure 2-15a. The amount of iodine in the cell pellet exposed to 4 mg/mL of iohexol was $2.27 \pm 0.23$ ug at t=0, but decreased to $0.35 \pm 0.071$ ug after 24 h of exocytosis, and to $0.13 \pm 0.050$ ug and $0.046 \pm 0.024$ ug after 48 h and 72 h, respectively. After 72 h of exocytosis, the iodine content in cell blocks was only $2.1 \pm 0.93\%$ (Figure 2-18a) of the total mass, and compared with t=0, the amount of iodine in each cell decreased by 97.93%, leaving only $0.013 \pm 0.007$ ug (Figure 2-20a) per cell. While the iodine content of cell clumps exposed to high concentration of iohexol, i.e. 16 mg/mL, decreased from $7.33 \pm 0.61$ ug at t=0 to $2.03 \pm 0.30$ ug, $0.79 \pm 0.21$ ug and $0.22 \pm 0.053$ ug after 24, 48 and 72 h of exocytosis, respectively (Figure 2-15a). The iodine content in the cell pellet decreased from $81.4 \pm 2.9\%$ at t=0 to only $2.5 \pm 0.5\%$ of the total mass at 72 h in Figure 2-18a. Accordingly, the iodine content in each cell decreased from $2.04 \pm 0.17$ ug to $0.061 \pm 0.014$ ug, which decreased by 97% (Figure 2-20a). Correspondingly, the iodine content in the cell supernatant of the iohexol group increased with the increase of exocytosis time. As shown in Figure 2-16a, the iodine content in the supernatant of 4 mg/mL increased from $0.18 \pm 0.017$ ug at t=0 to $2.15 \pm 0.32$ ug after 72 h of exocytosis, and its proportion in the total mass increased from $7.04 \pm 0.56\%$ to $97.93 \pm 0.93\%$ (Figure 2-19a); the iodine content in the supernatant in the 16 mg/mL group increased from $1.67 \pm 0.27$ ug to $8.76 \pm 0.59$ ug after exocytosis of 72 h (Figure 2-16a), which percentage in the total mass of iodine was increased by 80.9% to $97.5 \pm 0.53\%$ (Figure 2-19a). The above results indicated that small molecular contrast agent, iohexol, has a short retention time in cells, and 60% to 70% of iohexol would be excreted to extracellular within 24 h.
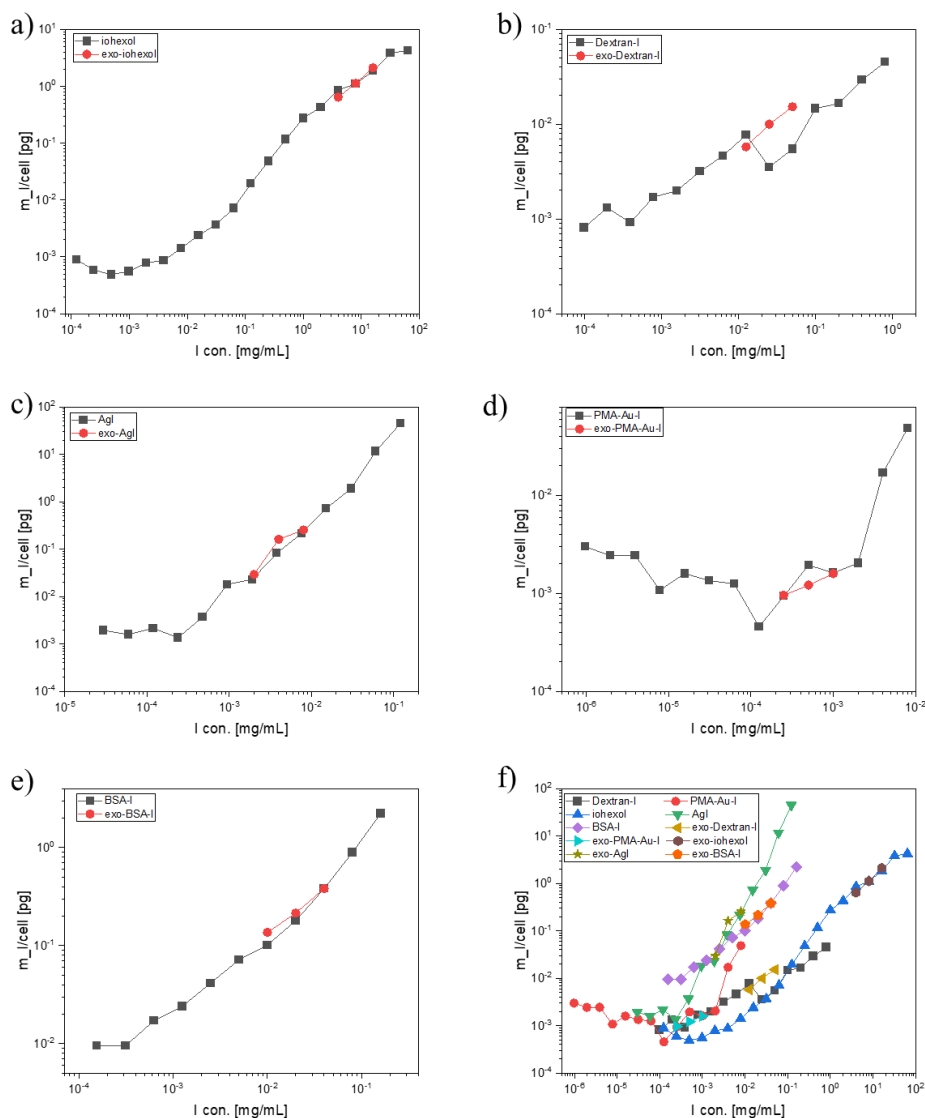
***Figure 2-14.*** *The corresponding endocytosis in exocytosis of Jurkat cell after exposed to different concentration of a) iohexol, b) Dex-I, c) AgI, d) PMA-Au-I, e) BSA-I for 24h in RPMI 1640 medium as measured by ICP-MS. f) The summary of corresponding endocytosis in exocytosis of iodine in different materials. X-axis refer to I concentration. Results are showed as percent cell viability [%] (mean) ± standard deviation (s.d.) from 3 independent experiments (n=3). Error bars are omitted for clarity and presented as average value. The ICP-MS was operated by our groupmate Yang Liu, and data was collected and analysis by myself.*

The other four carriers were glucose polymers, proteins and nanoparticles, all of which were macromolecules. The results of the exocytosis experiment showed that they remained in cells for a relatively long time. Among them, AgI NP has a lower exocytosis rate at low concentration,

namely exposure to 0.002 mg/mL, compared with medium concentration and high concentration, as shown in Figure 2-15c, 2-18c. The amount of iodine in cell clumps decreased from $66.5 \pm 20.7\%$ of the total mass ratio at t=0 to $22.1 \pm 10.7\%$ after 72 h of exocytosis, a decrease of 44.4%. The exocytosis rate was higher after 0.004 mg/mL and 0.008 mg/mL AgI NP treatment. The iodine content in cell pellet decreased from $0.35 \pm 0.027$ ug and $0.67 \pm 0.18$ ug at the beginning of exocytosis to $0.09 \pm 0.018$ ug and $0.22 \pm 0.03$ ug after 72 h of exocytosis, respectively. The percentage in total mass decreased by 62.9% and 55.8%, respectively. It is worth noting that the intracellular iodine amount of AgI NP and iohexol treated cells decreased most rapidly within 24 h, and then decreased at a slower rate within 48 or 72 h, so that the intracellular iodine amount of AgI NP treated cells during exocytosis for 48 and 72 h did not show significant changes. AgI NP-treated cells had a higher amount of iodine in the supernatant at t=0 (Figure 2-16c, 2-19c), especially in the low-concentration group, the iodine content in the supernatant was $0.052 \pm 0.046$ ug, accounting for $33.5 \pm 20.7\%$ of the total mass. This may be caused by accidentally separating a small part of the cells into the supernatant when separating the supernatant and cells at t=0.

A similar situation also appeared in the exocytosis experiments of Dex-I and PMA-Au-I NP-treated cells, which were shown in Figure 2-16b, d and 2-19b, d. Because of the low iodine labeling rate of these two carriers, the error in detecting the amount of iodine in the cells was large, and nine independent repeated experiments were carried out. Among them, the cells with PMA-Au-I internalized after 72 hours of exocytosis, the three concentrations from low to high, the intracellular amount of iodine decreased by 22.5%, 18% and 15.1%, respectively (Figure 2-18d). The exocytosis rate of cells exposed to Dex-I was lower than that of PMA-Au-I, and the intracellular amount of iodine decreased by 11.3%, 12.3% and 18.4% from high to low concentrations, respectively (Figure 2-18c). Although most Dex-I and PMA-Au-I NPs can stay in the cell for a long time, their internalization amount is small, and the error produced in the detection is relatively large. It is particularly noteworthy that the amount of iodine in the supernatant of the two groups is much higher than that in the cells (Figure 2-16b, d and 2-19b, d). On the one hand, because the iodine concentration in the supernatant is too low, the error of the iodine concentration obtained during the detection is relatively large, and multiplied by the large volume of the supernatant, the final result is much higher than the iodine content in the cell. On the other hand, the carrier may be adsorbed on the cell surface, so the

uninternalized iodine cannot be completely removed by washing at t=0, and the iodine adsorbed on the cell surface falls off into the supernatant in the subsequent cell culture process.

Among the evaluated iodine-labeled carriers, the amount of iodine of BSA-I treated cell internalization at t=0 is the highest among the four carriers except iohexol, as shown in Figure 2-15e. The endocytosis at the three concentrations of BSA-I was $0.36 \pm 0.078$ ug, $0.61 \pm 0.06$ ug and $1.23 \pm 0.25$ ug, respectively, and their proportions in the total mass are $87.1 \pm 6.9\%$, $88.7 \pm 5.2\%$ and $88.5 \pm 7.2\%$, respectively (Figure 2-18e). After 24 hours of exocytosis, the amount of iodine in the cells only decreased by about 10%, and the mass of iodine in the cell clumps was $0.30 \pm 0.055$ ug, $0.49 \pm 0.055$ ug and $1.07 \pm 0.22$ ug, respectively (Figure 2-15e and 2-18e). Although the mass of intracellular iodine in cell pellet treated with BSA-I was not as good as iohexol at t=24 h, it was much higher than the mass of intracellular iodine in cells treated with other carriers at exocytosis 24 h, and its exocytosis rate was significantly lower than that of iohexol. In addition, even after 72 h of exocytosis, the cells treated with 0.01 mg/mL, 0.02 mg/mL and 0.04 mg/mL of BSA-I still contained $52.2 \pm 9.0\%$, $63.6 \pm 6.6\%$ and $57.7 \pm 5.9\%$ of the total mass of iodine, respectively. Compared with t=0, the mass percentage of the intracellular iodine decreased 34.9%, 25.1% and 30.8%, respectively. Although the decrease rate of intracellular amount of iodine is not as low as that of Dex-I and PMA-Au-I NP, the final intracellular amount of iodine is the highest among the five compounds, which were $0.22 \pm 0.032$ ug, $0.39 \pm 0.024$ ug and $0.79 \pm 0.036$ ug, respectively (Figure 2-15e). These results indicate that BSA has potential advantages as an iodine carrier, with high amount of cell internalization and low cell efflux rate.
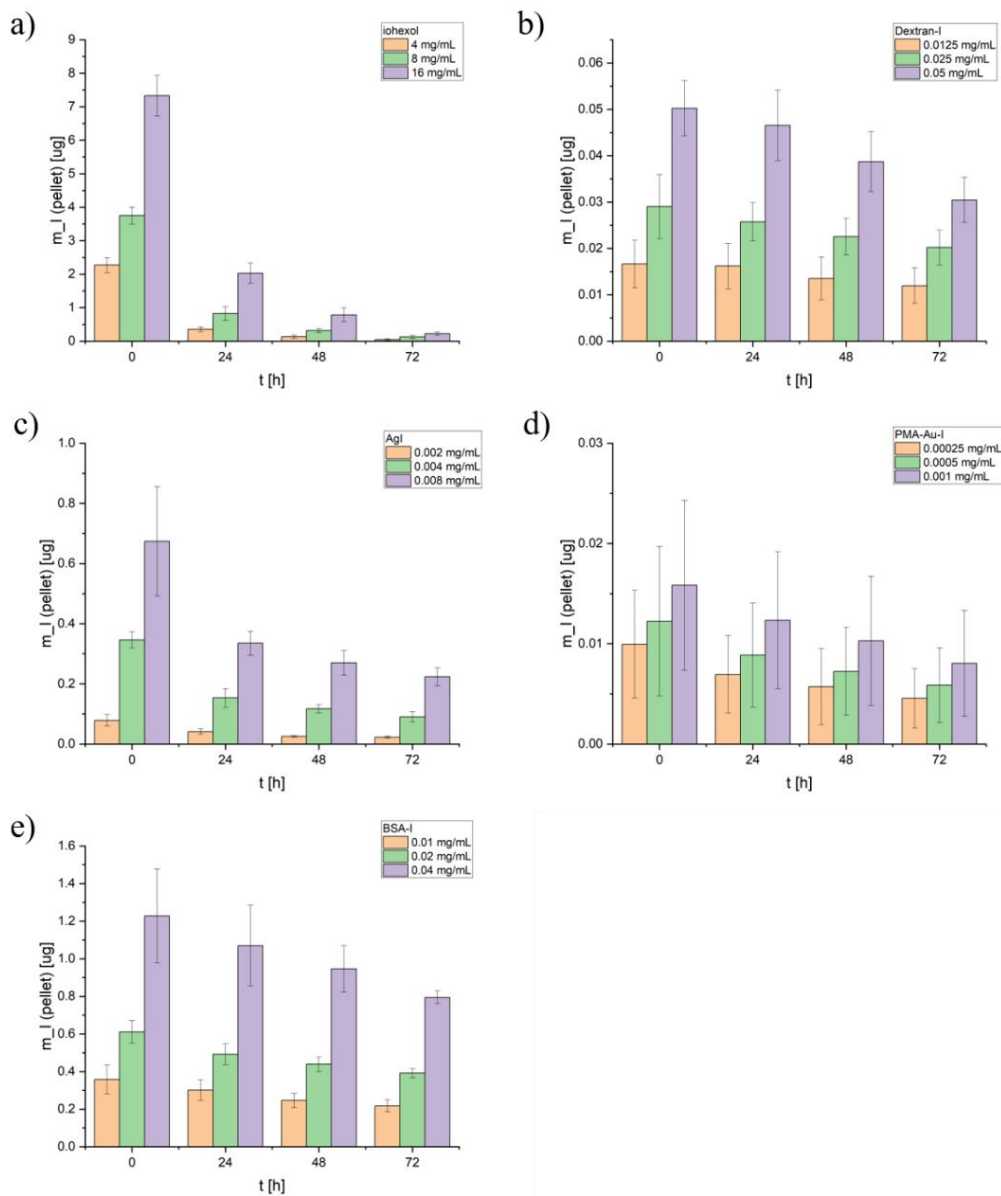
***Figure 2-15.*** *The exocytosis of Jurkat cell after exposed to different concentration at the indicated doses $c_I$ for 24 h (see the table of Table 2-3). The mass of iodine in the cell pellet, a) iohexol, b) Dex-I, c) AgI, d) PMA-Au-I, e) BSA-I, was measured by ICP-MS at the following 24, 48 and 72h. Results are showed as mean ± standard deviation (s.d.) from 3 independent experiments (n=3). The ICP-MS was operated by our groupmate Yang Liu, and data was collected and analysis by myself.*
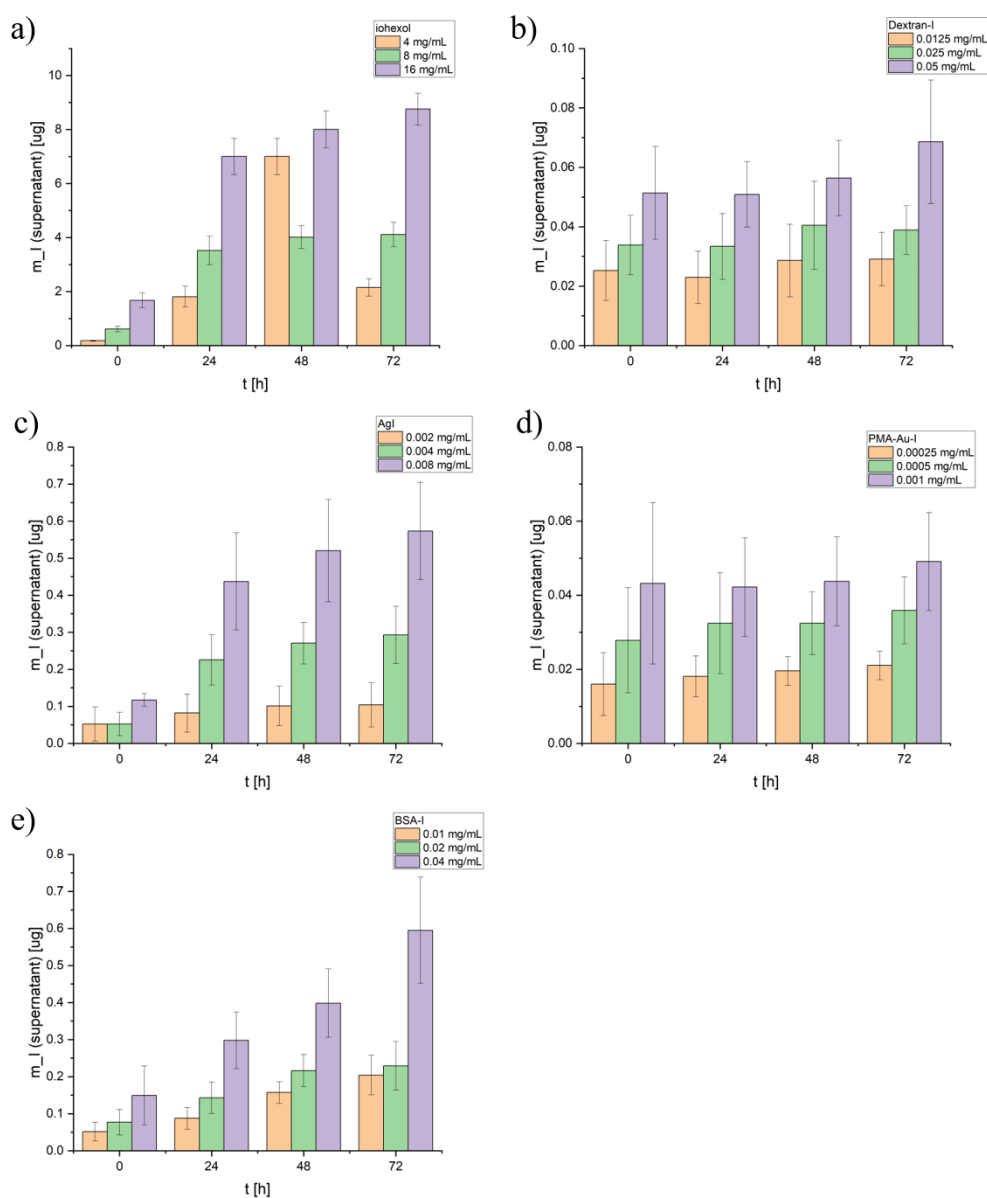
***Figure 2-16.*** *The exocytosis of Jurkat cell after exposed to different concentration at the indicated doses $c_I$ for 24 h (see the table of Table 2-3). The mass of iodine in the supernatant, a) iohexol, b) Dex-I, c) AgI, d) PMA-Au-I, e) BSA-I, was measured by ICP-MS at the following 24, 48 and 72h. Results are showed as mean ± standard deviation (s.d.) from 3 independent experiments (n=3). The ICP-MS was operated by our groupmate Yang Liu, and data was collected and analysis by myself.*
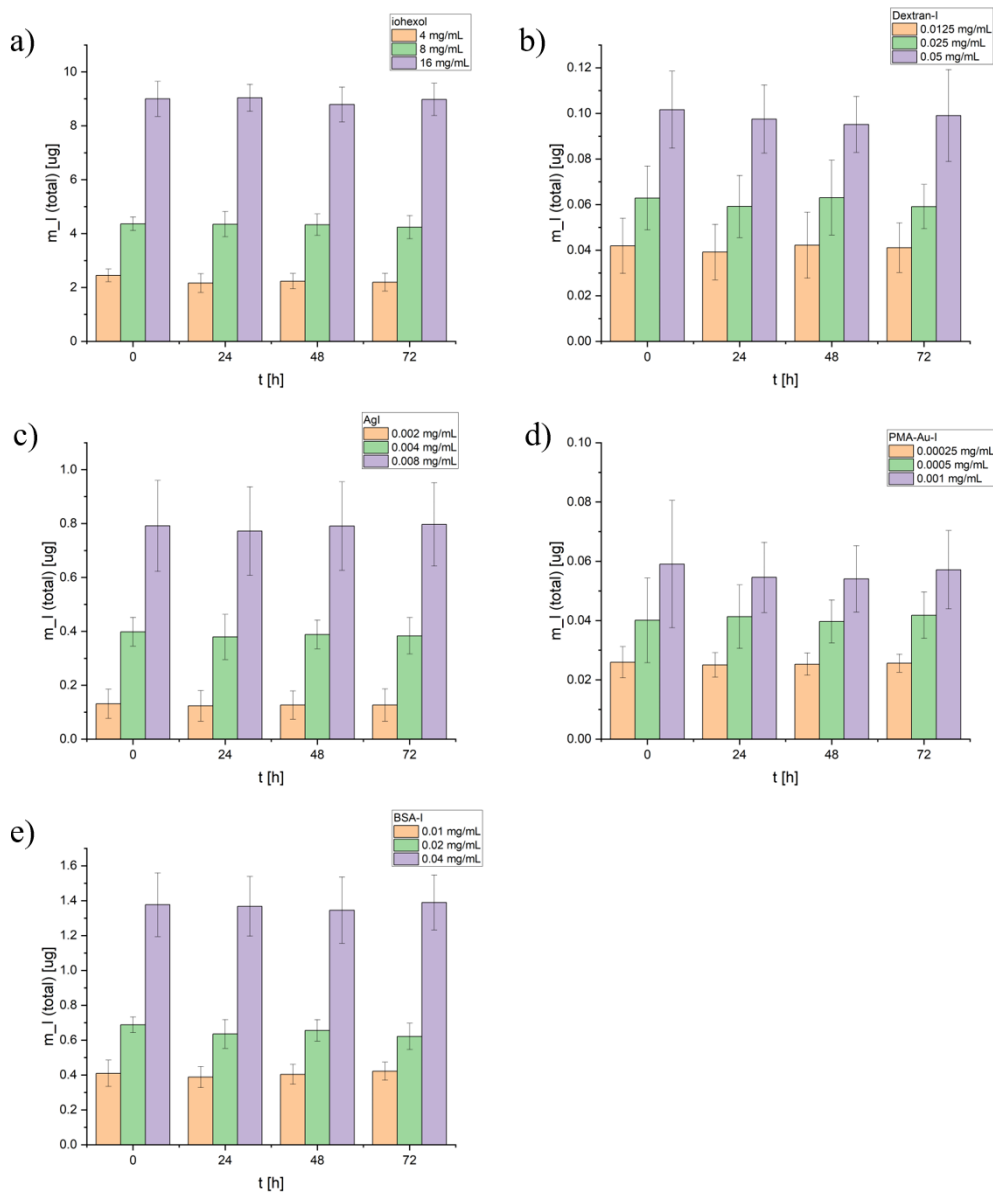
***Figure 2-17.*** *The exocytosis of Jurkat cell after exposed to different concentration at the indicated doses $c_I$ for 24 h (see the table of Table 2-3). The total iodine mass ($m_{pellet}$ + $m_{supernatant}$) of a) iohexol, b) Dex-I, c) AgI, d) PMA-Au-I, e) BSA-I, was measured by ICP-MS at the following 24, 48 and 72h. Results are showed as mean ± standard deviation (s.d.) from 3 independent experiments (n=3). The ICP-MS was operated by our groupmate Yang Liu, and data was collected and analysis by myself.*

***Figure 2-18.*** *The exocytosis of Jurkat cell after exposed to different concentration at the indicated doses $c_I$ for 24 h (see the table of Table 2-3). The amount of iodine in cell pellet as a percentage of total iodine of a) iohexol, b) Dex-I, c) AgI, d) PMA-Au-I, e) BSA-I, at the following 24, 48 and 72h. Results are showed as percent cell viability [%] (mean) ±standard deviation (s.d.) from 3 independent experiments (n=3). The ICP-MS was operated by our groupmate Yang Liu, and data was collected and analysis by myself.*
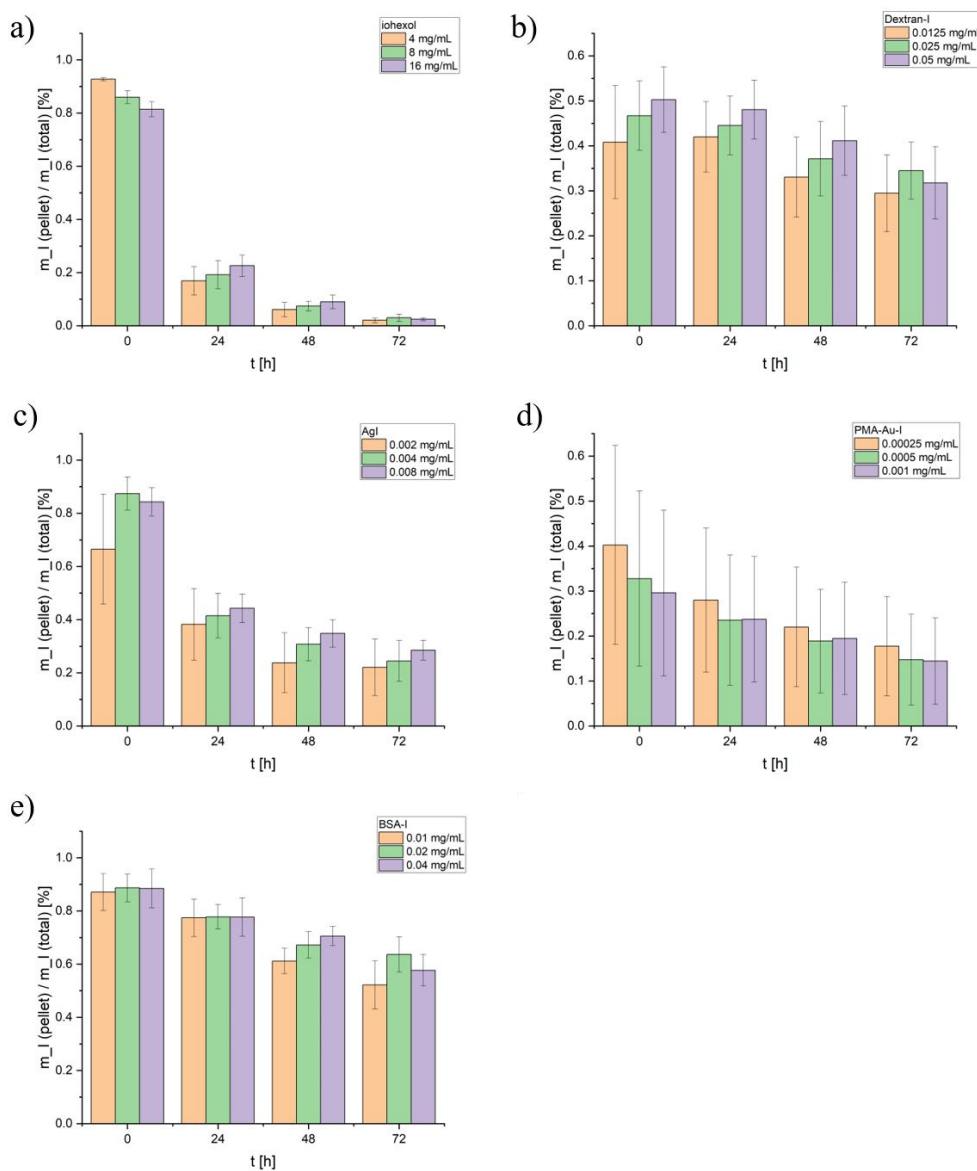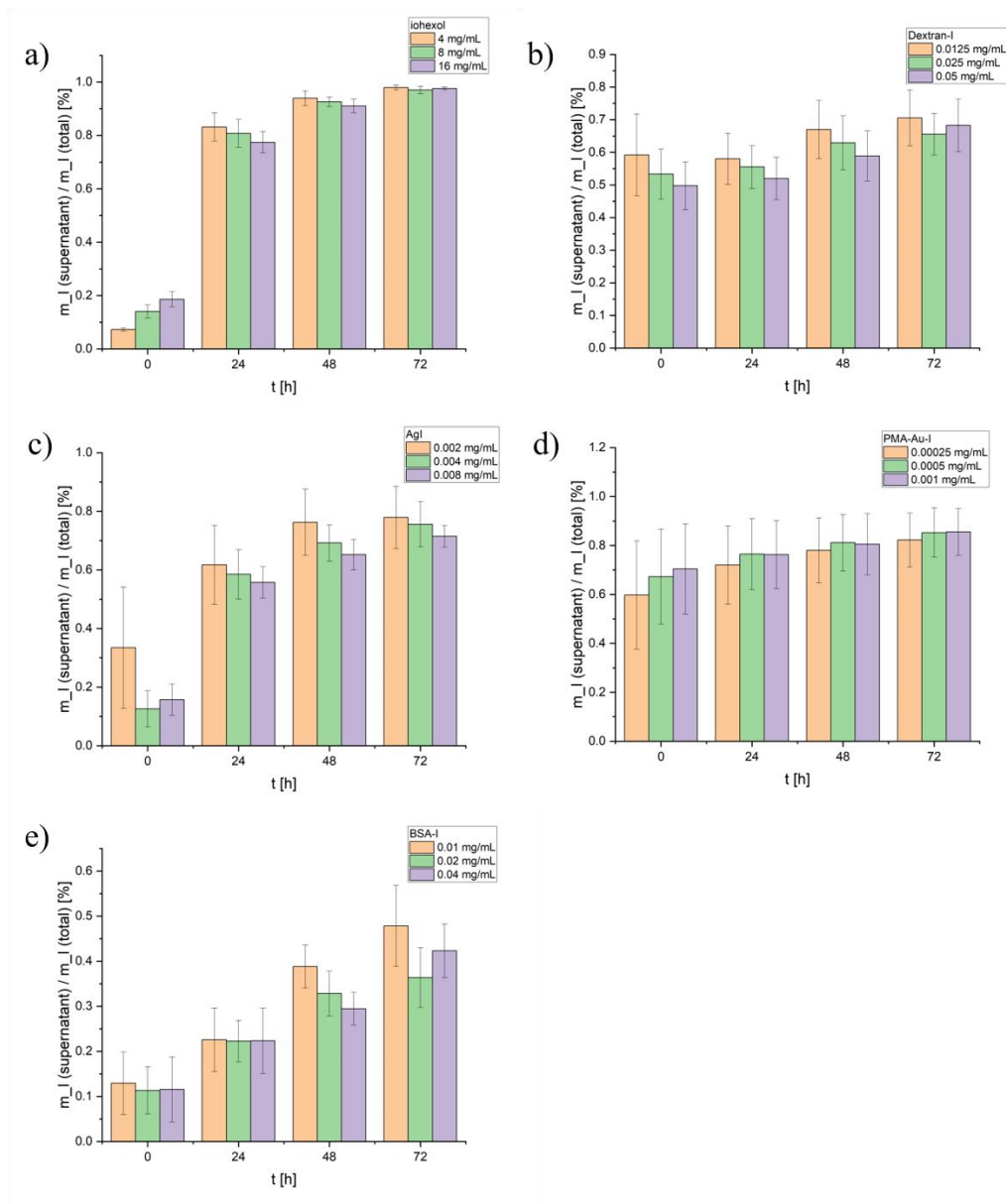
***Figure 2-19.*** *The exocytosis of Jurkat cell after exposed to different concentration at the indicated doses $c_I$ for 24 h (see the table of Table 2-3). The amount of iodine in supernatant as a percentage of total iodine of a) iohexol, b) Dex-I, c) AgI, d) PMA-Au-I, e) BSA-I, at the following 24, 48 and 72h. Results are showed as percent cell viability [%] (mean) ±standard deviation (s.d.) from 3 independent experiments (n=3). The ICP-MS was operated by our groupmate Yang Liu, and data was collected and analysis by myself.*

*Figure 2-20.* *The exocytosis of Jurkat cell after exposed to different concentration at the indicated doses $c_I$ for 24 h (see the table of Table 2-3). The amount of iodine in per cell of a) iohexol, b) Dex-I, c) AgI, d) PMA-Au-I, e) BSA-I, at the following 24, 48 and 72h. Results are showed as percent cell viability [%] (mean) ± standard deviation (s.d.) from 3 independent experiments (n=3). The ICP-MS was operated by our groupmate Yang Liu, and data was collected and analysis by myself.*

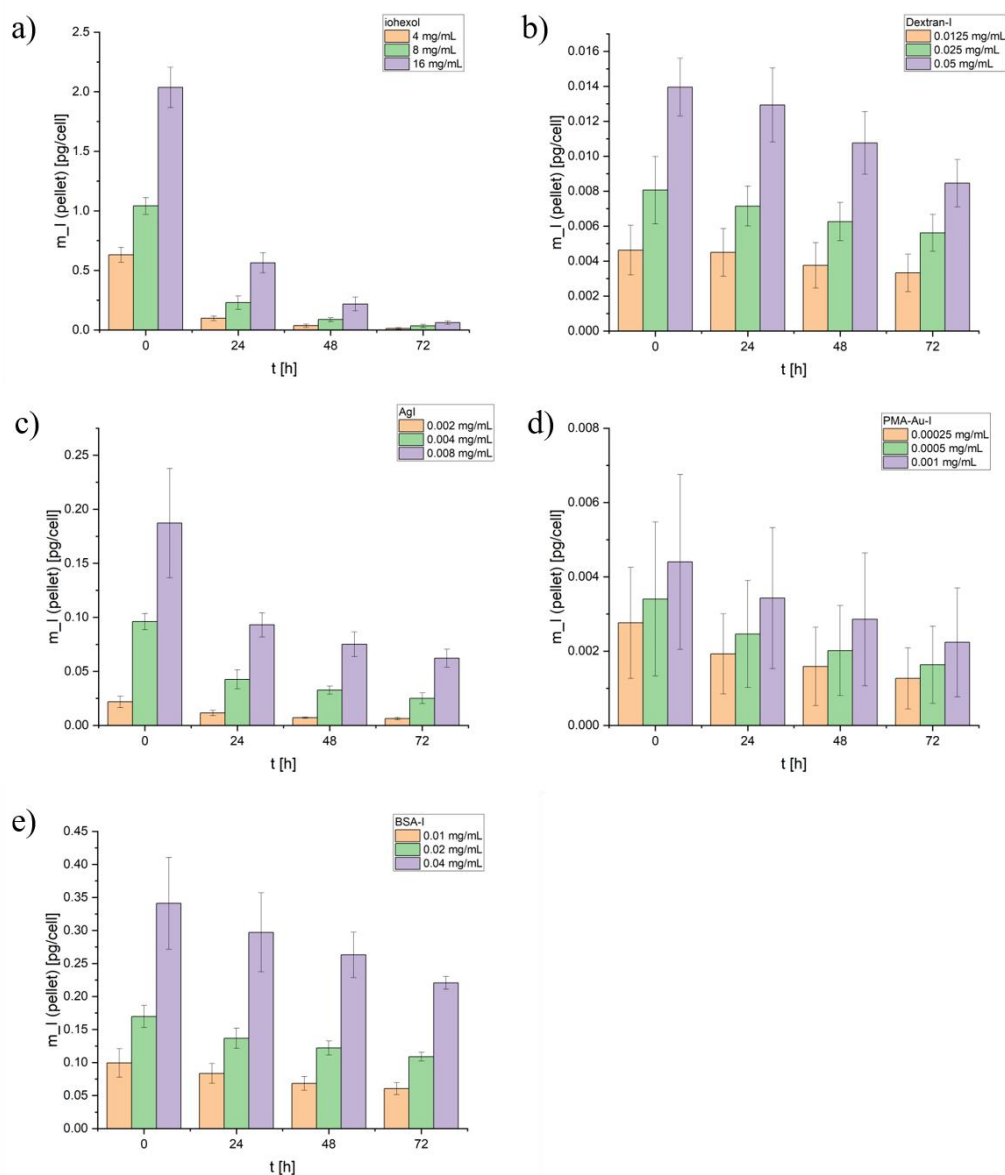## 2.6. Conclusion

X-ray imaging is one of the most widely used non-invasive imaging diagnostic techniques, which has been used in clinic for more than half a century. In order to enhance the contrast of soft tissues, a variety of CT contrast agents have been developed. At present, the most widely used water-soluble contrast agents in clinical practice are all derivatives of triiodobenzene ring, such as iohexol, iopamidol, iopromide, etc. However, since these contrast agents are small molecules containing iodine, the circulation time in the body is short, and the use of large doses leads to severe adverse reactions such as contrast-nephropathy, thyroid dysfunction, and allergies, which greatly limits their clinical application[7]. In the past decade, a great deal of research has been focused on the development of iodinated small molecules for clinical use into iodinated nanoparticles to prolong the circulation time of iodine in the body and increase its tissue permeability and retention time, including emulsions[96-97], liposomes[98], lipid proteins[99], polymer nanoparticles[100], etc. The primary purpose of these nanomaterials is to increase the iodine concentration in tissues so that the contrast can be higher than that of conventional water-soluble CT contrast agents. In addition, some studies have introduced metal and inorganic nanoparticles with high X-ray absorption properties into iodine contrast agents to increase their contrast performance[101-102]. For example, gold has attracted wide attention due to its higher atomic number than iodine and the photoelectric effect that contributes to X-ray attenuation. Many contrast agents based on Au nanoparticles are used for in vivo X-ray CT imaging[102-103]. Although there have been many ways to improve iodine-containing contrast agents, no research has shown which is the best way to deliver iodine, and the search for suitable iodine delivery vectors is essential for developing contrast agents that increase iodine concentration in tissues or organs for more efficient imaging.

This study investigated the efficiency of different carriers to deliver iodine into cells. First, BSA-I, Dex-I, AgI NP, and PMA-Au-I were synthesized by labeling iodine on proteins, glucose polymers and nanoparticles, respectively. The materials were characterized by UV, DLS, and TEM. The results showed the stability of iodine-labeled nanoparticles PMA-Au-I and AgI NP in the cell culture medium (with 10% FBS). The content of iodine in each material

was detected by ICP-MS, and the molar ratio of iodine to the carrier from high to low was BSA-I (4.19), Dex-I (2.87), AgI NP (0.61) and PMA-Au-I (0.07). Subsequent cell activity assay determined the toxicity of each carrier to Jurkat cells, that is, the highest safe concentrations of iohexol, Dex-I, AgI NP, PMA-Au-I and BSA-I are 32 mg/mL, 0.1 mg/mL, 0.008 mg/mL, 0.002 mg/mL and 0.04 mg/mL respectively. The uptake of iodine by Jurkat cells after exposure to a series of different vectors at different concentrations was measured by ICP-MS. The results showed that when Jurkat cells were exposed to the same concentration range of iodine, the internalization of AgI NP and BSA-I was significantly higher than that of iohexol, Dex-I and PMA-Au-I NP, and the iodine uptake showed a linear relationship with the concentration (Figure 2-14f). At low concentrations of AgI NP, the internalized iodine content of cells is not as evident as that of BSA-I compared to iohexol. For example, when the AgI NP concentration is $4.7 \times 10^{-4}$ mg/mL, the amount of iodine in each cell is 4.7 times that of iohexol, and when the BSA-I concentration is $3.1 \times 10^{-3}$ mg/mL, the intracellular iodine content is 10.6 times higher than that of iohexol. Although the endocytosis of AgI NP at high concentration is much higher than that of other materials, including BSA-I. However, $Ag^+$ is ionized in the cell, which is more toxic, resulting in its maximum safe concentration of 0.008 mg/mL. At this concentration, the iodine content is 0.22 pg/cell, 58.6 times that of iohexol. The safe concentration of BSA-I is higher than AgI NP, and the iodine content in each cell is 0.38 pg at 0.04 mg/mL, 103.7 times that of iohexol.

A carrier suitable for X-ray fluorescence imaging not only needs to be able to deliver as much iodine as possible into the cell, but also needs to remain in the cell long enough to meet the time required for imaging. Exocytosis showed that at least 60% of iohexol could be excreted by cells within 24 h, which was consistent with previous studies that iohexol was rapidly cleared from the circulatory system and vascularized tissues in vivo as a contrast agent[104]. AgI NP had a higher exocytosis rate, and about 40% of the iodine was excreted from the cells at 24 h, which may be because Ag nanoparticles are easy to dissociate into $Ag^+$ in the cells[105], which not only increases cytotoxicity, but also causes the loss of I ions. Although PMA-Au-I NP and Dex-I showed the lowest exocytosis rate, the amount of iodine in cell pellets only decreased by 22.5% at most after exocytosis 72 h. The low labeling rate of these two vectors resulted in the too little intracellular amount of

iodine and too large error in detection. However, the intracellular iodine mass of BSA-I was only reduced by about 10% within 24 h. Even after 72 h of exocytosis, the intracellular iodine mass was reduced by about 30%, and the amount of iodine retained in the cells was still the highest. In summary, although iohexol has the lowest toxicity to cells, its cellular uptake is low, especially at low concentrations, and its clearance rate is high. In contrast, BSA-I not only exhibits a significantly higher cellular uptake than other carriers, but also can remain in the cell for a longer period of time, indicating that BSA is a potential candidate for iodine delivery carriers. Therefore, BSA is the most excellent iodine delivery carrier in this study, which can not only deliver as much iodine into cells as possible, but also reduce the efflux of iodine by cells, prolonging the iodine angiography time, and provide the possibility for subsequent cell tracing by X-ray fluorescence imaging.

# 3. Evaluation of PSMA targeting AuNP based on Glu-Urea skeleton PSMA small molecule inhibitors

## 3.1. Introduction

Prostate cancer (PCa) is the malignant tumor with the highest incidence of the male reproductive system[106]. Early diagnosis of prostate cancer is of great significance to the prognosis of patients, but the current imaging technology has problems such as low sensitivity and poor specificity for the diagnosis of early prostate cancer[107]. Along with the development of molecular biology, found that the antigens associated with PCa tumor occurrence, development and biological markers, namely the prostate specific membrane antigen (PSMA), which is not only on the surface of PCa cells and tumor angiogenesis has high expression, and its expression level was positively correlated with tumor classification stage[24, 108], widely used in the diagnosis and treatment of PCa targeted study. Compared with traditional iodinated molecular contrast agents, AuNPs have a higher atomic number and X-ray absorption coefficient, and AuNPs have a longer blood vessel retention time, making them suitable for imaging applications. More recently, multiwalled carbon nanotubes and superparamagnetic iron oxide nanoparticles have been functionalized with PSMA ligand or the diagnosis and treatment of PCa[109-110]. Here, we report the synthesis and characterization of PSMA-targeted AuNPs and the investigation of targeting prostate cancer cells. Using 11-mercaptoundecanoic acid (MUA) as a spacer to obtain a high graft density of ligands on AuNPs, coupling PSMA-I to its carboxyl end gives AuNPs targeting. AuNPs coated with MUA were used as a control. Since the MUA chain length is only 1-2 nm, the size of PSMA-I may hinder the insertion of the motif into the binding pocket of the receptor. To account for this, we synthesized a set of additional ligands with an additional 6-aminohexanoic acid (AHX) spacer: MUA-AHX-PSMA-I, and MUA-AHX-GPI with alternative binding motifs, and MUA-AHX-Glu with terminal glutamic acid were used as another control without binding motifs. The above synthesized ligands bind to the surface of AuNPs through Au-S bonds, and we investigated their stabilizing effect on AuNPs and their targeting ability in vitro.

## 3.2. Major reagents

| Name | Purity | Company |
|---|---|---|
| DMEM medium no phenol red | NA | Gibico |
| Fetal bovine serum | NA | Gibico |
| Penicillin/streptomycin | NA | Gibico |
| Phosphate buffered saline | NA | Gibico |
| 0.05% trypsin/EDTA | NA | Gibico |
| Nitric acid | 67 wt% | Fisher Chemical |
| Hydrochloric acid | 35 wt% | Fisher Chemical |

## 3.3. Key instruments

| Name | Model | Company |
|---|---|---|
| Dynamic light scattering (DLS) | NANO ZS | Malvern |
| Transmission electron microscopy (TEM) | JEM-1400PLUS HC | JEOL, Germany |
| UV–Vis absorption spectrophotometer | Agilent 8453 | Agilent, USA |
| ICP-MS | 7700 Series | Agilent, USA |

## 3.4. Experiments and methods

### 3.4.1. Characterization of AuNPs modified with different ligands

#### 3.4.1.1. TEM of different batches of AuNPs used in this study

The ligands MUA, MUA-PSMA-I (PSMA-I), MUA-AHX-PSMA-I, MUA-AHX-GPI, MUA-AHX-Glu and AuNPs modified with these ligands were provided by Dr. Florian Schulz from the Faculty of Chemistry, Universität Hamburg and Center for Hybrid Nanostructures (CHyN).

For the modified AuNPs, the morphology and particles size of the core were observed by TEM. Simply, 10 µL of the diluted and evenly dispersed aqueous solution of AuNPs was gently dropped on a copper grid with carbon film, dry them naturally at room temperature, and put into transmission electron microscopy (TEM, JEOL, Germany) to take images and the histogram of particles size was analyzed by software ImageJ and Origin.



PSMA-I

MUA-AHX-PSMA-I

MUA

MUA-AHX-GPI

MUA-PSMA-I
(PSMA-I)

MUA-AHX-Glu
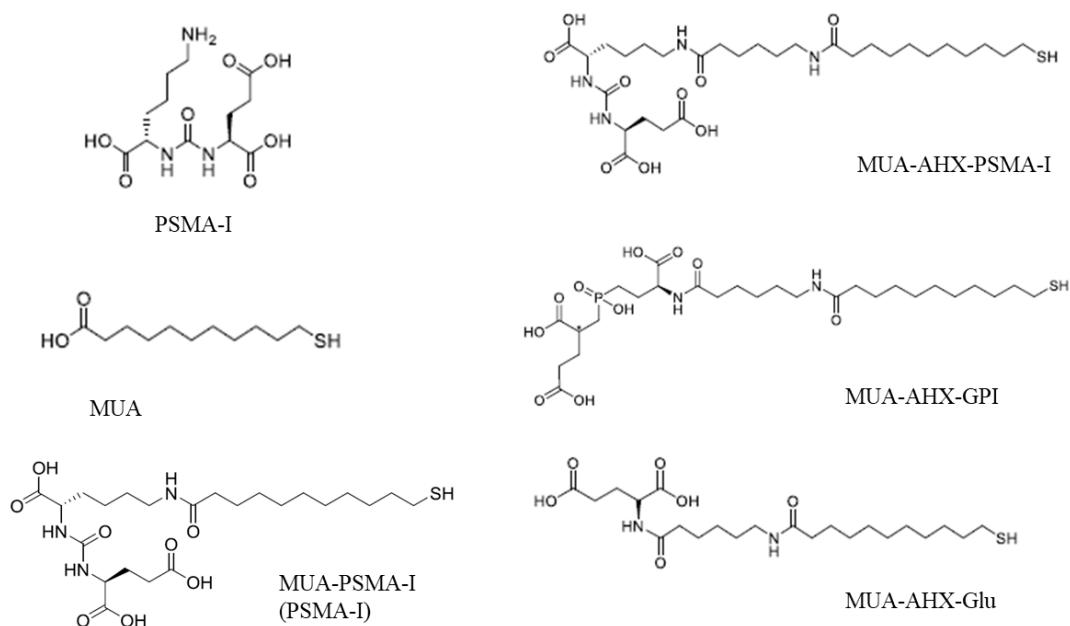
*Figure 3-1. Structures of the ligands used in the experiments.*

### 3.4.1.2. DLS and UV-vis

The hydrodynamic diameters $d_h$ and UV adsorption of various ligands-modified AuNPs were characterized by dynamic light scattering (DLS, Malvern ZS, England) and Ultraviolet–visible spectroscopy (UV-Vis). For that, each sample was diluted 50 times with MIlliQ water to a final volume of 2 mL. The sample was filtered using a filter membrane with a pore size of 0.22 µm and put in UV Kuevette, ZH 8.5 mm Deckel (Sarstedt, Germany) to equilibrate at 25 °C for 5 min, and then perform particles size measurement at 173 ° backscatter setting and a 633 nm laser.

Similarly, before the UV absorption spectra of AuNPs modified with different ligands were obtained, it is necessary to dilute the sample was diluted with MilliQ water to a suitable

concentration, and centrifuged at a low speed (e.g., 2000 rpm for 5 min) or filtered with a 0.22 μm filter membrane to remove impurities. Then transferred samples to UV Kuevette to collect the ultraviolet absorption spectra in the range of 300-800 nm wavelength using an Ultraviolet–visible spectroscopy (UV-Vis, Agilent 8453).

### 3.4.2. Colloidal stability of AuNPs modified with different ligands in different media

In order to evaluate the sedimentation of colloidal nanoparticles used in this experiment before conducting the in vitro experiment, the stability assay of AuNPs modified with different ligands dispersed in different media for 0 h and 24 h was performed. The investigated media include MilliQ water, PBS and cell medium (Dulbecco Modified Eagle Medium, DMEM) containing 10% fetal bovine serum (FBS). Simply, 10 μL of stock AuNPs solution was taken out and gently mixed into a cuvette containing 990 μL MilliQ water or PBS or DMEM supplement with 10% FBS, respectively. Stability was evaluated both by DLS and UV-vis at different incubation times of 0 h and 24 h. Firstly, the changes of absorption peaks of AuNPs modified with different ligands in different media at different time points were observed through UV-vis. Secondly, the changes of hydrodynamic diameter of AuNPs modified with different ligands in different media were measured by DLS.

### 3.4.3. Cell line and cell culture

PC3-PIP cells with (PC3+PSMA) and PC3 cells without (-PSMA) overexpression of the PSMA receptor were kindly provided by Dr. Elisabetta Gargioni of Department of Radiotherapy and Radiation Oncology, University Medical Center Hamburg-Eppendorf. PC3+PSMA cell and PC3-PSMA cell were cultured in Dulbecco's Modified Eagle's Medium (DMEM, Thermofisher, USA) supplemented with 10% fetal bovine serum (FBS, Biochrom, Germany) and 100 U/mL penicillin/streptomycin (P/S, Fisher Scientific, Germany) at 37 °C and 5% $CO_2$.

### 3.4.4. Cellular uptake study by ICP-MS

Cellular uptake experiments were conducted based on protocols described previously[111]. PC3+PSMA and PC3-PSMA cells were planted into 6-well plates with bottom growth area of 9.6 cm$^2$ at a density of $2 \times 10^5$ cells/well with volume of 2 mL containing serum medium (10%

fetal bovine serum, FBS), and were allowed to attach overnight. The next day, the old cell medium was removed and the cells were exposed to 2 mL fresh medium containing the according to nanoparticles. The exposure concentrations of AuNPs used in the experiment are shown in Table 3-1. The plate was incubated at 37 °C for 24 h or 48 h. After the exposure time, the nanoparticle solution was removed and cells were washed with 2 mL PBS three times. Then, 0.3 mL trypsin, ethylenedia-minetetraacetic acid (EDTA) (0.01% trypsin–EDTA) was added to detach the cells from the plate bottom and transferred to Eppendorf tubes. After centrifugation at 300 RCF for 5 min, cells were resuspended in 1 mL PBS, and 10 µL of this solution was diluted 10 times to count the cell number using a cell count chamber (Neubauer Chamber, Celeromics Technologies, Spain). Cells were then collected again by centrifugation. For digestion, 75 µL $HNO_3$ was added and the sample left overnight to lyse the cells, then 150 µL HCl was added to digest the AuNPs. Finally, the samples were further diluted (1:10) with 2 wt% HCl before measuring the elemental concentration of Au in the sample with ICP-MS. The Au-concentrations of all nanoparticle solutions used for uptake experiments were also determined with ICP-MS to calculate the uptake. By dividing the detected mass of elemental gold by the number of cells in the sample, the amount of internalized AuNPs per cell could be given as $m_{Au}$ [pg/cell]. Experiments were performed in independent triplicates; each experiment was with different generations of cells and incubations were done on different days.

***Table 3-1.*** *The concentrations of different ligands modified AuNPs used for cell uptake experiments. The concentrations are presented as mass concentration (mg/mL) of the Au.*

| sample | $C_{Au}$ (mg/mL) |
|---|---|
| MUA | $1.47 \times 10^{-3}$ -$9.40 \times 10^{-2}$ |
| PSMA-I | $1.47 \times 10^{-3}$ -$9.40 \times 10^{-2}$ |
| MUA-AHX-PSMA-I | $1.47 \times 10^{-3}$ -$9.40 \times 10^{-2}$ |
| MUA-AHX-GPI | $1.47 \times 10^{-3}$ -$9.40 \times 10^{-2}$ |
| MUA-AHX-Glu | $1.47 \times 10^{-3}$ -$9.40 \times 10^{-2}$ |

## 3.5. Results and discussions

### 3.5.1. Characterization of the different ligands modified AuNPs

A transmission electron microscope (TEM) was used to analyze the particle size and morphology of the obtained AuNPs. The TEM image is shown in Figure 3-2. It can be seen from the figure that the prepared AuNPs are spherical in appearance and uniform in particle size. The average particle size of AuNPs is calculated to be $11.5 \pm 0.79$ nm. We verified it by UV absorption spectroscopy. UV-vis absorption spectroscopy is one of the primary methods for studying gold nanoparticles. The number, position and intensity of its characteristic absorption peaks are related to the size, morphology and chemical environment of the gold nanoparticles. With the increase of particle size, the corresponding peak value of colloid nanoparticles would appear to a certain degree of redshift[112]. Generally, gold nanoparticles have strong absorption peaks at 500-600 nm[113]. The result is shown in Figure 3-3a. AuNPs have a maximum absorption peak at 516 nm, which is the typical surface plasmon resonance ultraviolet absorption characteristic of gold nanoparticles. In addition, the peak shape is symmetrical and the half-width is narrow, indicating that the prepared gold nanoparticles have a narrow particle size distribution. In addition, at room temperature, the particle size and distribution of colloidal gold solution were analyzed by Malvern particle Size analyzer, and the obtained particle size distribution of AuNPs was shown in Figure 3-3b. The result showed the particle size distribution of AuNPs is relatively uniform, with an average particle size of about $13.5 \pm 1.53$ nm, which is larger than that observed by TEM. This may be because the overlapped particles in the gold nanoparticles or the charged layer on the surface of the AuNPs interfere with the particle size analyzer so that the measured particle size is relatively large.
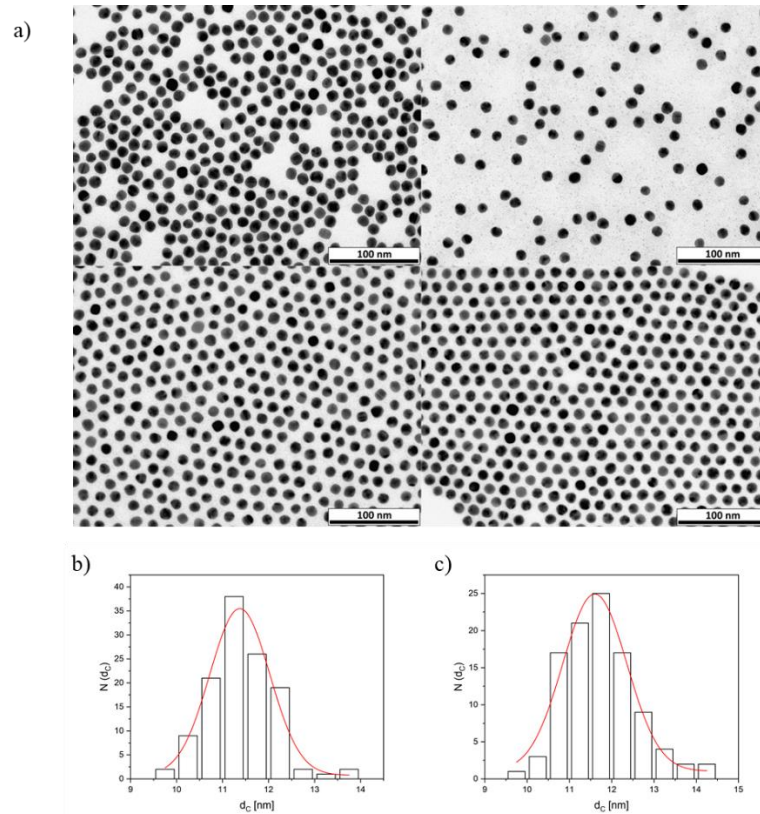
***Figure 3-2.*** *a) Exemplary TEM measurements of different AuNP batches used in this study. TEM figures were obtained from Dr. Florian Schulz from the Faculty of Chemistry. Histogram of particle size in two TEM images of lower panel, the mean value ± standard deviation of b) and c) sample were $d_C = 11.41 \pm 0.71$ nm and $11.67 \pm 0.86$ nm, respectively.*
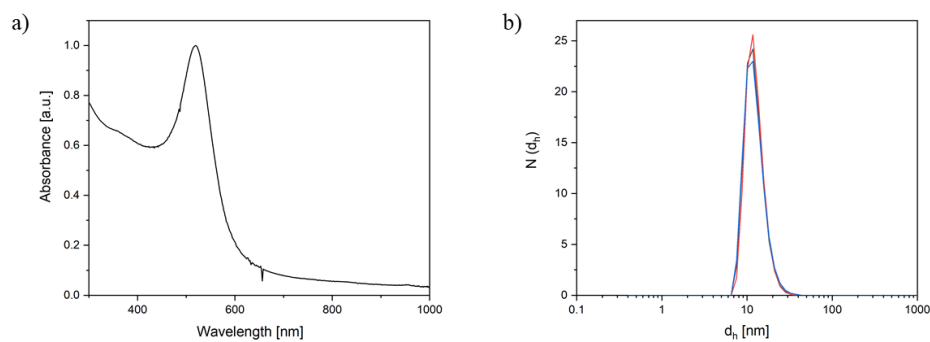


***Figure 3-3.*** *a）UV-vis spectra and b) DLS particle size distribution of AuNPs in TEM.*

### 3.5.2. Stability of AuNPs modified with different ligands in different media

To apply nanoparticles in the field of biomedicine, it is essential to investigate the stability of nanoparticles in the in vivo or in vitro environment. We investigated the stability of

AuNPs functionalized with different ligands which synthesized based on MUA to target PSMA protein in different solutions, including MilliQ-water, PBS and cell culture medium DMEM supplemented with 10% FBS. The surface plasmon resonance characteristics of AuNPs are susceptible to the spacing between particles. The well-dispersed gold nanoparticles are wine-red, the UV absorption peak is around 520 nm, and the half-peak width is narrow. After aggregation, it is blue or black, and its corresponding characteristic peak shows the phenomenon of red shift or widening and the absorption intensity decreases significantly. Therefore, we can judge whether the particles have aggregated by observing the state of the characteristic absorption peak of the surface plasma of AuNPs[114]. Figure 3-4 shows the UV-Vis absorption spectra of AuNPs with different surface modifications for 24 hours in different solutions. In Figure 3-4a, the MUA-modified AuNPs are only stable in water, while in PBS, the UV absorption peak appears broadened and a certain degree of redshift occurs. In DMEM, the stability of MUA is worse, and the ultraviolet absorption peak not only appears red-shifted and broadened, but also becomes two peaks. These results indicate that the irreversible aggregation of MUA occurs in PBS and DMEM. Also unstable in DMEM are AuNPs modified by MUA-AHX-Glu, as shown in Figure 3-4e, in DMEM, the stability of MUA-AHX-Glu is significantly reduced. Agglomeration occurs continuously with the extension of time, not only the maximum absorption peak splits into two peaks, but also the absorbance value is continually reduced to complete precipitation. In contrast, the UV absorption peaks of PSMA-I, MUA-AHX-PSMA-I and MUA-AHX-GPI in MilliQ-water, PBS and DMEM showed good reproducibility (Figure 3-4b, c, d). In particular, the UV absorption peaks of PSMA-I and MUA-AHX-PSAM-I almost wholly overlap, indicating that these two ligands can keep AuNPs stable in water or cell medium. However, the UV absorption peak of MUA-AHX-GPI is red-shifted from 520 nm to 533 nm in DMEM, indicating that there will be a small amount of aggregation in DMEM. The different performance of AuNPs modified by different ligands in cell culture media may be due to the difference in the surface charge of AuNPs caused by the different ligands, and the protein concentration required to maintain a stable concentration is also different[115]. The coagulation of MUA and MUA-AHX-Glu in the cell culture medium may be since the free protein on the surface of AuNPs is not enough to form a protein corona that completely "encapsulates" a single NP, so that they can overcome charge repulsion and

approach each other to cause aggregation[116-117].
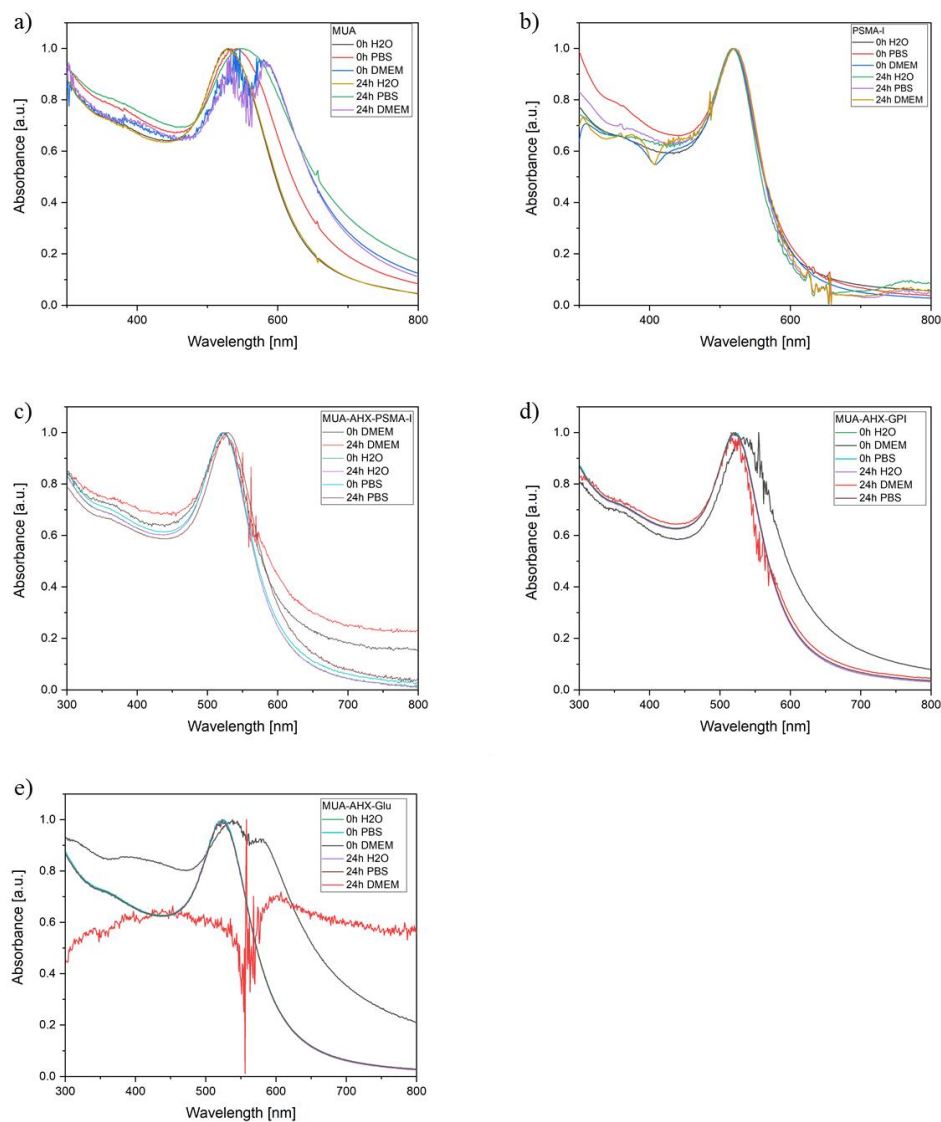


***Figure 3-4.*** *Absorbance spectra of a) MUA, b) PSMA-I, c) MUA-AHX-PSMA-I, d) MUA-AHX-GPI and e) MUA-AHX-Glu dispersed in different media: water (H₂O), PBS, and cell medium (Dulbecco Modified Eagle Medium, DMEM) at different waiting times (0 and 24 h). Broadening of the plasmon peak and scattering effects indicate significant agglomeration of the nanoparticles.*

We used DLS to detect the changes in hydrodynamic diameter ($d_h$) of each ligand-modified AuNPs in MilliQ-water, PBS and DMEM at different time points to further verify the stability. The results are shown in Figures 3-5, 3-6, 3-7, 3-8 and 3-9. The DLS test results are consistent with the UV results. PSMA-I and MUA-AHX-PSMA-I can remain stable in the

presence of FBS. Due to the formation of protein corona, the particle size of MUA-AHX-GPI is larger than that in water. DLS results show that the most unstable ones are still MUA-AHX-Glu and MUA, which have apparent precipitation formation in DMEM. However, it should point out that in Figure 3-5, MUA has agglomeration in PBS, which is contrary to its UV spectrum. This may be because the aggregated large particles sink to the bottom, and the solution was not shaken evenly during the UV detection, and the UV wavelength failed to irradiate the aggregated large particles.
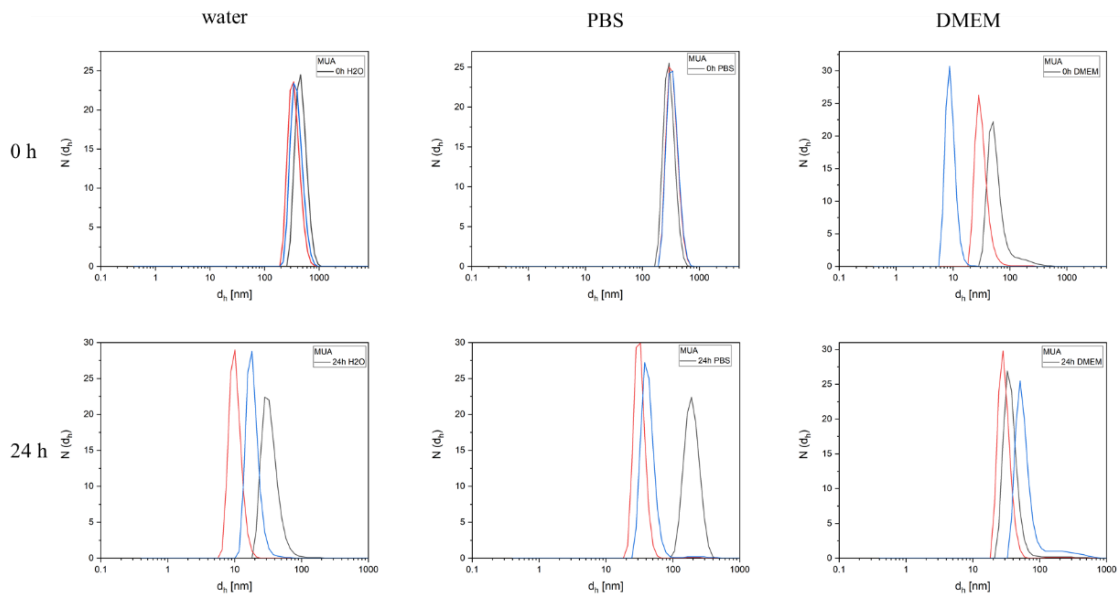


***Figure 3-5.*** *Hydrodynamic diameters of MUA dispersed in different media: water ($H_2O$), PBS, and cell medium (Dulbecco Modified Eagle Medium, DMEM) at different waiting times (0 and 24 h).*
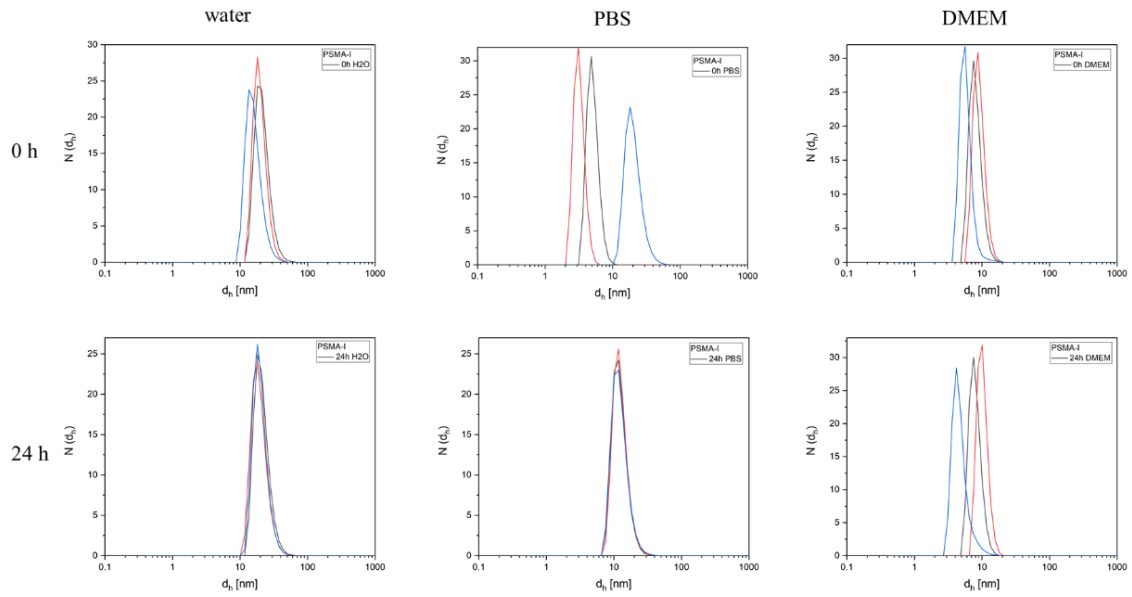
***Figure 3-6.*** *Hydrodynamic diameters of PSMA-I dispersed in different media: water ($H_2O$), PBS, and cell medium (Dulbecco Modified Eagle Medium, DMEM) at different waiting times (0 and 24 h).*
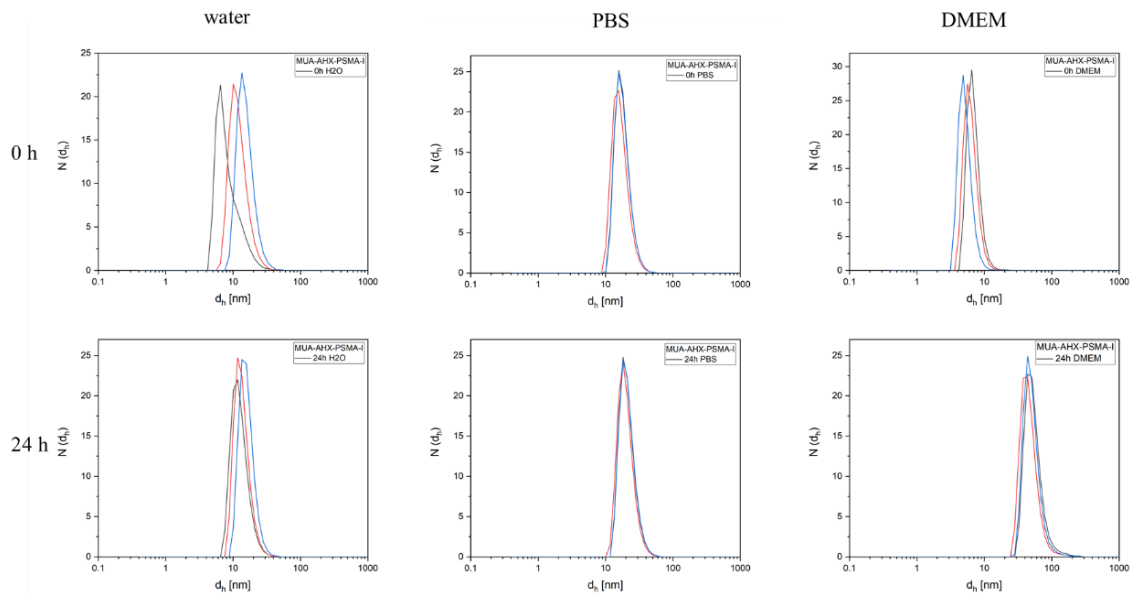


***Figure 3-7.*** *Hydrodynamic diameters of MUA-AHX-PSMA-I dispersed in different media: water ($H_2O$), PBS, and cell medium (Dulbecco Modified Eagle Medium, DMEM) at different waiting times (0 and 24 h).*
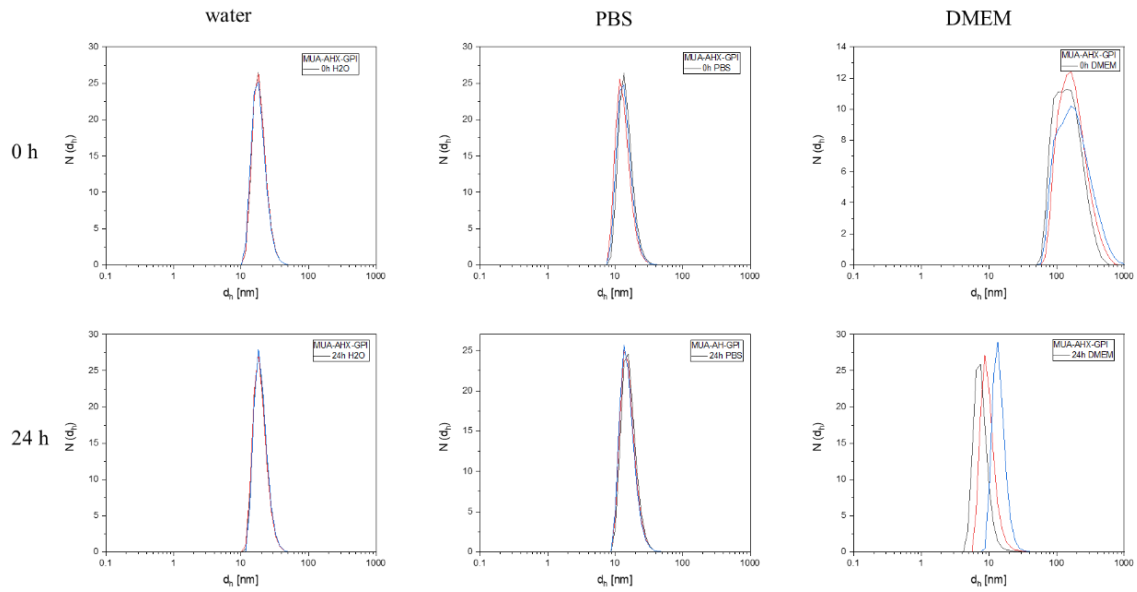
***Figure 3-8.*** *Hydrodynamic diameters of MUA-AHX-GPI dispersed in different media: water (H$_2$O), PBS, and cell medium (Dulbecco Modified Eagle Medium, DMEM) at different waiting times (0 and 24 h).*



***Figure 3-9.*** *Hydrodynamic diameters of MUA-AHX-Glu dispersed in different media: water (H$_2$O), PBS, and cell medium (Dulbecco Modified Eagle Medium, DMEM) at different waiting times (0 and 24 h).*

### 3.5.3. Cellular uptake study by ICP-MS

In order to evaluate the targeting of each ligand, PC3+PSMA cells (overexpress PSMA protein) and PC3-PSMA cells (not express PSMA protein) were exposed to different concentrations of MUA, PSMA-I, MUA-AHX-PAMA-I, MUA-AHX-GPI and MUA-AHX-Glu ligand-modified AuNPs for 24 h and 48 h, respectively. ICP-MS is used to detect the quality of the colle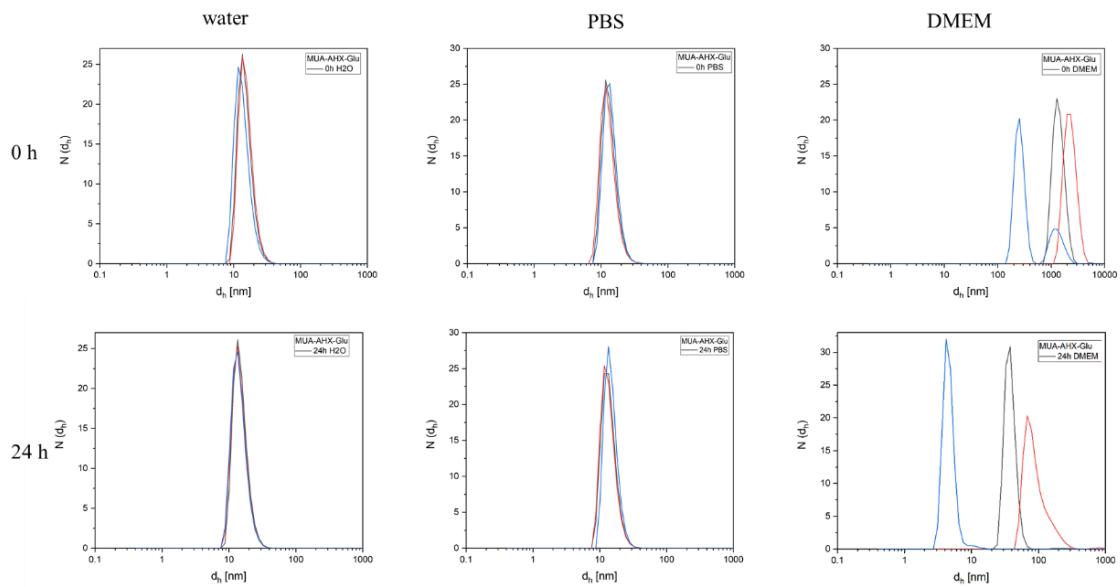cted intracellular gold to investigate the targeting. The results are shown in Figure 3-10. All cells and nanoparticles show typical concentration-dependent endocytosis. However, it is worth noting that the endocytosis of all nanoparticles in PC3-PSMA cells is higher than that in PC3+PSMA cells. After PC3+PSMA and PC3-PSMA cells were exposed to 0.094 mg/mL MUA for 24 h, their endocytosis was 8.34 ± 6.55 pg per cell and 2.73 ± 0.55 pg per cell, respectively. However, when the exposure time was increased to 48 h, each cell that overexpressed PSMA protein contained 4.46 ± 3.19 pg, and each cell that did not express PSMA protein contained 6.10 ± 0.22 pg (Figure 3-10a). Because MUA has no targeting effect, it is used as a control in this experiment. In addition, the relationship between the endocytosis of MUA and cell lines is not obvious. This is also because MUA is unstable in the culture medium and would aggregate and adhere to the cell membrane surface, which will significantly interfere with the test results of ICP-MS.

MUA-AHX-Glu, as shown in Figure 3-10e, which is also unstable in the culture medium, is deposited on the cell surface during cell exposure. Still, its endocytosis exhibits a concentration-dependent and time-dependent endocytosis. After PC3+PSMA cells were exposed to MUA-AHX-Glu for 24 h and 48 h, the amount of Au in each cell was 2.43 ± 0.33 pg and 4.04 ± 0.34 pg, respectively. The internalization amount of MUA-AHX-Glu in PC3-PSMA cells also showed that the increase in its content almost doubled with the prolongation of exposure time. The internalization of MUA-AHX-Glu in PC3-PSMA cells also showed that with the prolongation of exposure time, its content in each cell increased exponentially. When PC3-PSMA cells were exposed to 0.094 mg/mL MUA-AHX-Glu for 48 h, the amount of Au was 12.40 ± 2.35 pg per cell, which was three times that of PC3+PSMA cells. When cells were exposed to MUA-AHX-GPI, a small amount of aggregation of nanoparticles was observed under the microscope, which was consistent with its stability

results. The endocytosis results in the two types of cells are shown in Figure 3-10d. The internalization of the highest working concentration of MUA-AHX-GPI on PC3+PSMA and PC3-PSMA cells after 48 h is greater than 24 h, indicating that the endocytosis of MUA-AHX-GPI is also time-dependent.
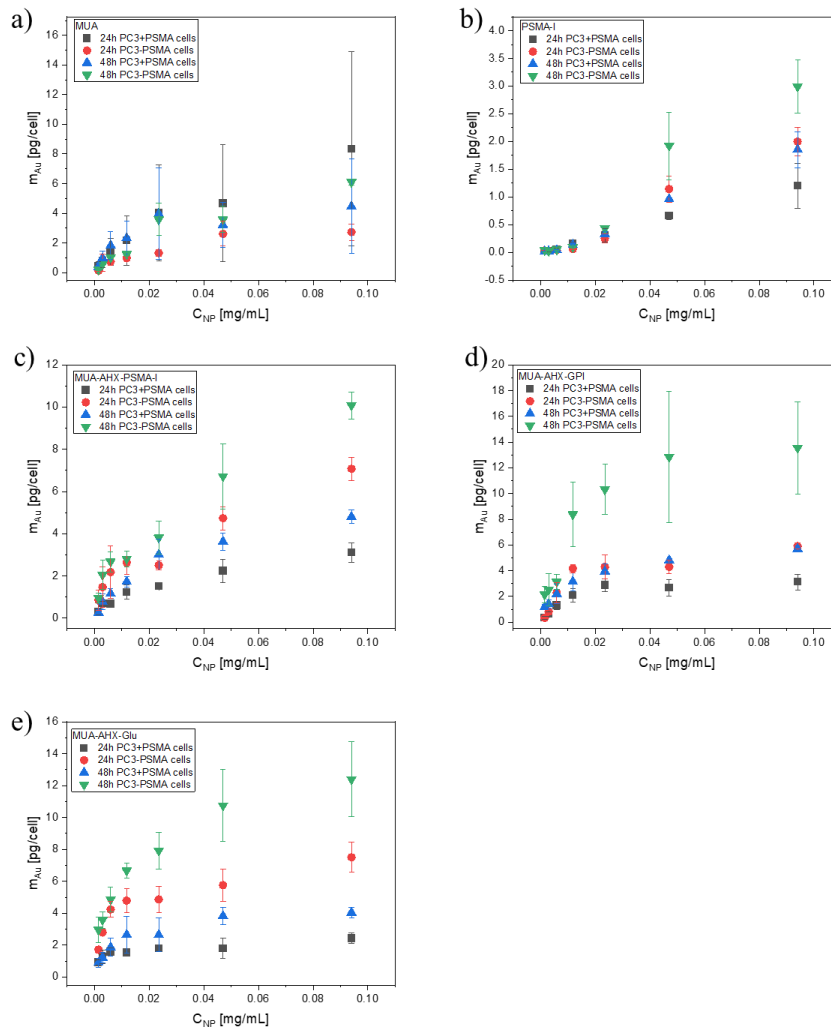


***Figure 3-10.*** *Uptake of a) MUA, b) PSMA-I, c) MUA-AHX-PSMA-I, d) MUA-AHX-GPI and e) MUA-AHX-Glu by PC3+PSMA and PC3-PSMA cells after 24 h and 48 h. Amount of internalized AuNPs in terms of mass of gold $m_{Au}$ per cell for different AuNPs and different incubation times. Data are from three independent experiments (n=3) and represent mean values ± standard deviations.*

The two endocytosis effects of PSMA-I and MUA-AHX-PSMA-I are shown in Figure 3-10b and c, which are consistent with the endocytosis of the above nanoparticles. The

endocytosis of these two kinds of nanoparticles in PC3-PSMA cells was significantly higher than that in PC3+PSMA cells. At 24 h, in PC3+PSMA cells treated with 0.094 mg/mL PSMA-I and MUA-AHX-PAMS-I, the amount of Au in each cell was 1.20 ± 0.40 pg and 3.11 ± 0.46 pg, respectively. Under the same conditions, the contents of the two types of nanoparticles in PC3-PSMA cells were 2.00 ± 0.26 pg and 7.07 ± 0.56 pg, respectively, which may be due to cell lineage effects.

To facilitate comparison, the uptake for each of the different nanoparticles is plotted for the two different cell types in Figure 3-11. It can be observed that the endocytosis of all nanoparticles in the two types of cells at 48 h is higher than the endocytosis at 24 h, except for MUA. In addition, the highest uptake is observed for MUA-AHX-GPI, however the uptake was higher in PC3-PSMA cells not overexpressing the PSMA receptor. This was also the case for the other particles. The lowest uptake was found in PSMA-I, regardless of cell type and time point, suggesting that increasing the length of the ligand chain plays a role in improving uptake.
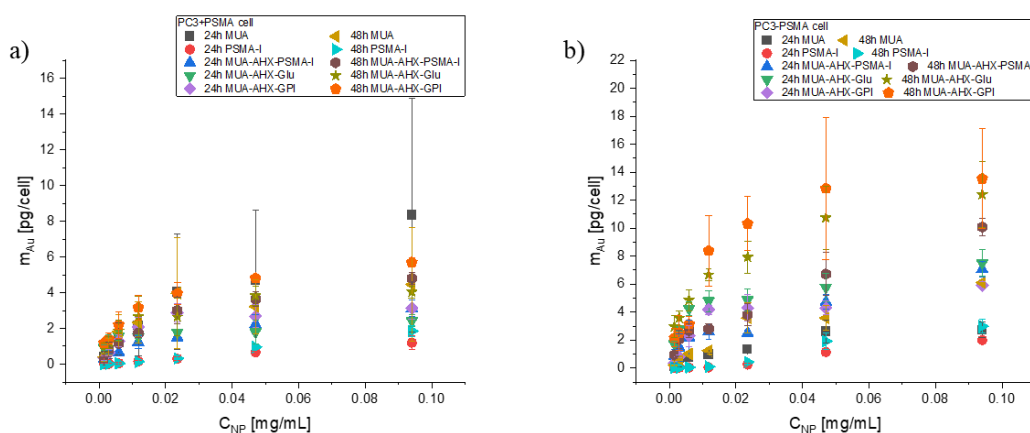


***Figure 3-11.*** *Uptake of MUA, PSMA-I, MUA-AHX-PSMA-I, MUA-AHX-GPI and MUA-AHX-Glu by a) PC3+PSMA cells (overexpressing PSMA) and b) PC3-PSMA cells (not overexpressing PSMA) after 24 h and 48 h. Amount of internalized AuNPs in terms of mass of gold mAu per cell for different AuNPs and different incubation times. Data are from three independent experiments (n=3) and represent mean values ± standard deviations.*

## 3.6. Conclusion

Early detection, early diagnosis and accurate clinical staging are essential for the development of appropriate treatment and management methods for prostate cancer patients[118]. However, due to prostate cancer, especially early prostate cancer, is characterized by small lesions and multifocal and scattered growth[119], conventional imaging methods such as ultrasound, CT, MRI, whole body bone imaging, etc., cannot meet the needs of clinicians for early diagnosis and accurate staging of prostate cancer patients, which are very important for the treatment and management of patients. Therefore, how to use imaging methods to improve the detection rate of suspicious prostate cancer has always been a research hotspot in the diagnosis of prostate cancer.

For prostate cancer, prostate-specific membrane antigen (PSMA) is a critical tumor-specific antigen. It is not only highly expressed on the surface of prostate cancer cells and tumor neovascularization[110], but its expression level is positively correlated with the tumor grade and staging[32, 108]. In addition, the sequence in the cytoplasmic domain of PSMA mediates the internalization and intracellular recovery of the contrast agent, which can make the contrast agent highly aggregate in tumor cells[120]. These characteristics of PSMA make it an important target for molecular imaging of prostate cancer. At present, several imaging methods based on PSMA have been developed, including antibodies, nanobodies and small molecule inhibitors[121]. PSMA small molecule inhibitors have the advantages of good cell permeability and fast blood clearance. They mainly include the following three categories: urea groups, sulfhydryl groups, and phosphate groups[65]. Studies have confirmed that PSMA small molecule inhibitors containing urea groups have the highest affinity for PSMA and the highest cell uptake rate, and can be imaged 1 to 2 hours after injection[122].

Based on the potential application advantages of PSMA small molecule inhibitors as targeted molecules, we designed and developed an AuNPs with Glu-Urea skeleton as the target molecule and MUA as the spacer, and used the unmodified MUA ligand as the control. MUA is smaller than PEG, making the gold surface obtain a higher graft density, and usually makes the nanoparticles more stable[123]. In addition, the MUA spacer allows the

binding motif to be only 1-2 nm away from AuNPs, so that the size of the nanoparticles after conjugation does not change much, and the small-sized nanoparticles are more conducive to the clearance of the kidney. However, its binding capacity may be reduced because the size of the conjugate may prevent the motif from being inserted into the binding pocket of the receptor. With this in mind, we added 6-aminohexanoic acid (AHX) to the MUA spacer, namely MUA-AHX-PSMA-I. In addition, combining glutamate and another alternative motif on MUA-AHX to synthesize MUA-AHX-Glu and MUA-AHX-GPI, respectively, as a control. After these ligands were successfully modified on the surface of AuNPs, they were subjected to basic characterization, such as ultraviolet and DLS, and the results showed that the synthesized PSMA targets AuNPs with uniform particle size. In order to further investigate the targeting properties of these ligands in vitro, we first investigated the stability of AuNPs modified by different PSMA targeting ligands in different media. The displacement and broadening of the plasma peak indicate the aggregation of nanoparticles and the displacement and limited reproducibility of the apparent hydrodynamic diameter measured by DLS[78, 111]. In MilliQ water or PBS, we observed strong signs of agglomeration of MUA and MUA-AHX-Glu through DLS and UV/Vis absorption spectroscopy, and MUA-PSMA-I, MUA-AHX-PSMA-I and MUA-AHX-GPI have slight aggregation. However, in the cell culture medium, except for MUA-PSMA-I, all the others showed evident aggregation. This may be because the steric stability provided by the small ligand MUA is limited to the AuNP with a diameter of dc ~ 12 nm used in this study[123]. Although MUA well exposes the functionalized part on the surface, it cannot reduce protein adsorption like PEG. The high-density grafting obtained by MUA causes too much protein to be adsorbed on the surface of AuNPs, which leads to aggregation of nanoparticles.

Then, five kinds of nanoparticles with different concentrations were exposed to PC3-positive cells expressing PSMA protein and PC3-negative cells without PSMA protein for 24 h and 48 h, respectively. The internalization number of nanoparticles in the two kinds of cells was detected by ICP-MS to investigate the targeting. For all cells and nanoparticles, typical concentration-dependent endocytosis can be observed. For both cell lines, the uptake of MUA is higher than that of MUA-PSMA-I, which indicates that the stability of colloidal nanoparticles is dominant in the uptake of nanoparticles. AuNP with poor colloidal

stability accumulates and deposits on the top of the cell, thus increasing the chance of the cell contacting the nanoparticles[111, 124].

In addition, in order to better investigate the feasibility of targeting nano-targeted PSMA small molecule inhibitors based on the Glu-Urea framework for the early diagnosis of prostate cancer, we need to improve the stability of the ligand. By using PEG ligands with hydrophobic spacers that connect the mercaptan group to the PEG portion, for example, α -methoxy poly(ethylene glycol)-ω-(11-mercaptoundecanoate) (PEGMUA), and the use of hydrophobic spacers are very effective for enhancing chemical stability and improving performance in biological media[123]. And our previous experimental results also show that the distance between the motif and the nanoparticles can be controlled by spacers. In addition, Matthias Eder et al.[125] synthesized a series of Glu-Urea-based DOTA-conjugated PSMA inhibitors and evaluated theirs in vitro and in vivo properties. The in vitro and in vivo experiments of 18 synthetic PSMA inhibitor variants show that the systematic chemical modification of the linker has a significant impact on tumor targeting and pharmacokinetic properties. Therefore, the following two directions can be studied: 1) optimizing the composition of the ligand shell and 2) improving the molecular structure of the ligand.

# 4. Oriented Coupling of Discrete Number of Antibody to AuNPs for targeted labeling cell

## 4.1. Introduction

Inorganic nanoparticles are suitable for intracellular drug delivery due to their unique physical and chemical properties[126]. Moreover, recent research has shown that multifunctional inorganic nanocarriers that integrate imaging, targeted drug delivery, and collaborative therapy have excellent application prospects in drug delivery systems. Many studies have reported that NP can passively target treatment sites through enhancement and penetration (EPR)[127]. However, active targeting is still the primary goal of nanocarrier research to target lesions and reduce damage to normal cells specifically. One classical approach for active targeting is mediated by molecular recognition via capture molecules, i.e., antibodies (Abs) specific for the target. NP needs to be combined with specific Abs to achieve targeting. Abs are usually coupled to the surface of NP by electrostatic adsorption or covalent bonding. The Abs orientation of the combination of these two methods is randomized, which is a combination of "end-on," "head-on," "sideways-on," and "flat-on" spatial orientation[128]. Especially in the case of Abs in the "end-on" and "sideways-on" orientations, the antigen recognition efficiency of functionalized NPs may be hindered due to steric hindrance[41]. In addition, studies have shown that the Abs density on the surface of NPs will also affect the targeting of NPs[129]. Therefore, the orientation and control of the number of Abs on the NP surface is the key to keeping the Abs activity intact to achieve the desired purpose.

Here, we integrated the SNAP-tag expression sequence into the plasmid backbone expressing the single-chain antibody scFv to obtain the scFv-SNAP with the SNAP-tag attached at the bottom. AuNPs with 1 or 2 G-PEG grafted on the surface were separated by gel electrophoresis. Since that SNAP-tag can specifically bind to benzylguanine (BG) and its derivatives, scFv was directionally coupled to 1-G-PEG-AuNPs or 2-G-PEG-AuNPs, to obtain AuNPs with different discrete numbers of scFv, and investigate the relationship between their in vitro targeting ability and surface antibody density.

## 4.2. Major reagents

| Name | Purity | Company |
| --- | --- | --- |
| hydrogen tetrachloroaurate (III) | ≥ 99.9% | Sigma aldrich |
| tetraoctylammonium bromide | 98% | Sigma aldrich |
| sodium borohydride | ≥ 98% | Sigma aldrich |
| dodecanethiol | ≥ 98% | Sigma aldrich |
| didodecyldimethylammonium bromide | ≥ 99% | Alfa Aesar |
| 6-chloroguanine | ≥ 99% | Sigma aldrich |
| N-methylpyrrolidine | ≥ 99% | Sigma aldrich |
| HO-PEGn-NHBOC | NA | Rapp Polymere |
| 1-ethyl-3-(3-dimethylaminopropyl)carbodiimide hydrochloride | ≥ 99% | Sigma aldrich |
| SNAP-Vista® Green | NA | NEW ENGLAND BioLabs |
| agarose | NA | Sigma aldrich |
| Tris-boric | ≥ 99.5% | Sigma aldrich |
| Thermo Scientific™ Coomassie (Bradford) Protein Assay Kit | NA | Thermo Scientific |
| ammonium persulphate | ≥ 98% | Sigma aldrich |
| Acrylamide solution 40% | 40% | Thermo fisher |
| N,N,N',N'-Tetramethyl ethylenediamine | ≥ 99% | Sigma aldrich |
| Glycerol | ≥ 99% | Sigma aldrich |
| Sodium Dodecyl Sulfate | NA | Sigma aldrich |
| dimethylformamide | ≥ 99% | Carl Roth |
| NaH | ≥ 99.9% | Sigma aldrich |
| trifluoroacetic acid | 99% | Sigma aldrich |

## 4.3. Key instrument

| Name | Model | Company |
|---|---|---|
| Dynamic light scattering (DLS) | NANO ZS | Malvern |
| Transmission electron microscopy (TEM) | JEM-1400PLUS HC | JEOL, Germany |
| UV–Vis absorption spectrophotometer | Agilent 8453 | Agilent, USA |
| nuclear magnetic resonance (NMR) | AV 700 | Bruker, USA |
| Gel electrophoresis | BioRad | BioRad |
| SDS-PAGE | BioRad | BioRad |

## 4.4. Experiments and methods

### 4.4.1. Synthesis of dodecanethiol-stabilized AuNPs

#### 4.4.1.1. Modified Brust–Schiffrin two-phase method

A modified Brust-Schiffrin method was used to synthesize hydrophobic 4nm AuNPs[78]. To be specific, 300 mg of hydrogen tetrachloroaurate (III) (0.9 mmol, $HAuCl_4$, 99.9%, Sigma Aldrich, no. 12325) was dissolved in 25 mL of MilliQ-water as the gold precursor and placed in a separation funnel of 250 mL. Following, 80 mL of toluene containing 2.170 g of tetraoctylammonium bromide (3.9 mmol, TOAB, $N(C_8H_{17})_4^+Br^-$, Sigma-Aldrich no. 294136) was added immediately as the organic phase. The two phases in the funnel were rotated and shaken up and down for 5 min, and the two phases were thoroughly mixed and then allowed to stand until completely stratified (the upper phase changes from colorless to orange, indicating the complete transfer of $AuCl^-$ ions to the organic layer). The aqueous phase (lower phase) was discarded and transferred the organic solution into a 250 mL round flask. After that, using sodium borohydride ($NaBH_4$, 98%, Sigma-Aldrich no. 452882) as reducing agent, 334 mg of $NaBH_4$ was dissolved in 5 mL Milli-Q water and added into the round flask, and stirred with organic solution containing gold precursor for 1 h at room

temperature to ensure the complete reaction. During this period, Au (III) was reduced by NaBH$_4$ to Au (0) forming TOAB-capped AuNPs and the solution would also change from orange to purple-black. The solution was then transferred to the separatory funnel and washed 3 times with 25 mL of 10 mM HCl and NaOH, respectively. After each time the organic phase and the washing liquid are shaken and thoroughly mixed, the lower water phase is thrown away. The washing step can remove the excess salt and the remaining unreacted gold ions in the system. The washed solution was re-transferred to a 250 mL round-bottom flask and stirred overnight to obtain stable AuNPs with a relatively uniform particles size.

TOAB, like Citrate ligand, is weakly adsorbed on the surface of AuNPs, and it's easy to fall off from the surface of AuNPs, resulting in irreversible agglomeration of AuNPs. In order to obtain more stable AuNPs for subsequent manipulation, TOAB can be ligand exchanged with dodecanethiol containing mercapto group, which can form strong Au-S bond on the surface of AuNPs. For that, add 10 mL of 1-dodecanethiol (DDT, 98%, Sigma-Aldrich no. 471364) to TOAB capped AuNPs solution and stirred the mixture at 65 °C for 2 h, and then cool down to room temperature to yield DDT stabilized AuNPs (DDT-AuNPs). Subsequently, the solution was placed into several 50 mL centrifuge tubes, centrifuged at 900 RCF for 5 min, and the solution was collected. At the same time, the sediment at the bottom was discarded to remove large nanoparticles. A suitable amount of methanol was added to the solution (until the DDT-AuNPs solution became turbidity) to precipitate DDT-AuNPs, and then the mixture was centrifuged at 900 RCF for 5 min to collect DDT-AuNPs. Next, the precipitated DDT-AuNPs were redispersed in chloroform, and methanol was added again for precipitation. The DDT-AuNPs were recollected by centrifuging at 900 RCF for 5 min. This step is repeated twice to collect the DDT-AuNPs of similar size. The final collected DDT-AuNPs precipitate was redispersed in chloroform for subsequent experiments.

### 4.4.1.2. Digestive ripening method

The principle of this method is the same as the above method[130], which also reduces Au (III) to Au (0) via NaBH$_4$ to form nanoparticles. However, the synthesis process of the digestive

ripening method is more straightforward and the nanoparticle size distribution of the obtained nanoparticles is narrower. In particular, 202 mg of didodecyldimethylammonium bromide (DDAB, 99%, Alfa Aesar, no. B22839) and 65 mg of HAuCl$_4$ were dissolved in 30 mL toluene with sonication, and the solution gradually turned orange, indicating the formation of didodecyldimethylammonium tetrachloroaurate ion pairs (N(C$_8$H$_{17}$)$_4^+$AuCl$_4^-$). 1 mL of Miili-Q water containing 40 mg of NaBH$_4$ was added to the solution with stirring at room temperature for 1 h. The solution turns purple-black indicated that the formation of AuNPs. After that, 1.6 mL of DDT was added for ligand exchange and stirred for 2 h. The obtained DDT-AuNPs were washed once with methanol or ethanol, dried under vacuum and redispersed in 20 mL of toluene containing 1.6 mL of DDT by ultrasonic for 3 min. The mixture was heated to a slightly boiling and kept boiling and condensing reflux for 3 h for digestive ripening. The AuNPs were then precipitated with 20 mL of methanol or ethanol and centrifuged at 9000 rpm for 10 min to collect, dried under vacuum and redispersed in 5 mL of chloroform with 50 μL of DDT. Finally, the solution was centrifuged at a low speed (2000 rpm, 5min) to remove large agglomerations.

### 4.4.2. Synthesis of PMA-coated AuNPs (PMA-AuNPs)

The procedures for PMA coating on the surface of DDT-AuNPs are the same as in section 2.4.1.4. In brief, 1 mL of 0.5 M PMA was added into 50 mL of chloroform and mixed with DDT-AuNPs solution, dried under reduced pressure at 40 °C and then redissolved in 50 mL of chloroform. This step was repeated three times to obtain a more homogeneous PMA coating. After the final drying, the film was dissolved in 10 mL of SBB buffer, followed by centrifuging at 50000 rpm for 30 min via an Ultracentrifugation to remove excess PMA and replaced the solvent with Milli-Q water.

### 4.4.3. Synthesis of Guanine-O-PEGn-NH$_2$ conjugate

#### 4.4.3.1. Synthesis of 1-(2-amino-7H-purin-6-yl)-1-methyl-pyrrolidinium chloride

In a 25 mL round-bottom flask, 169.6 mg of 6-chloroguanine (1 mmol, Sigma Aldrich, no. 109789) was added into 10 mL of dimethylformamide (DMF, Carl Roth, no. T921.2), heated

to 40 °C and stirred to dissolve, then 0.23 mL of *N*-methylpyrrolidine (2.23 mmol, Sigma Aldrich, no. 69110) and stirred for 18 h. After the reaction, 1 mL of acetone was added, and the mixture was filtered, washed twice with diethyl ether, and dried at low temperature to obtain the product.
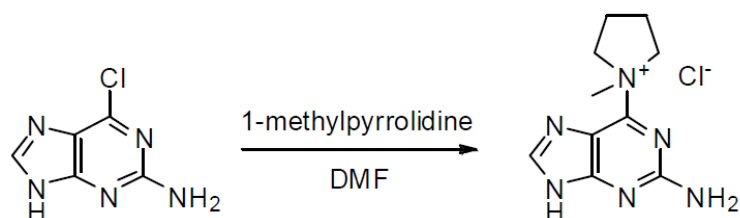


**Figure. 4-1.** *Synthesis of 1-(2-amino-7H-purin-6-yl)-1-methyl-pyrrolidinium chloride.*

### 4.4.3.2. Synthesis of Guanine-O-PEG$_n$-NHBOC conjugate

In a 10 mL round-bottom flask, 100 mg of HO-PEG$_n$-NHBOC (5 kDa, 0.02 mmol, Rapp Polymere, no. 135000-00-21) was dissolved in 5 mL of anhydrous dimethylformamide (DMF, Carl Roth, no. T921.2), followed by 2.2 mg of NaH (Sigma Aldrich, no. 223441) was added, stirred under nitrogen protection for 15 min, and then 5.6 mg of 1-(2-amino-7H-purin-6-yl)-1-methyl-pyrrolidinium chloride was added for reaction as shown in Figure 4-2. The reaction lasted for 48 h, after which the solvent was evaporated and the product was purified by size exclusion column to yield the grey-white powdered desire product.
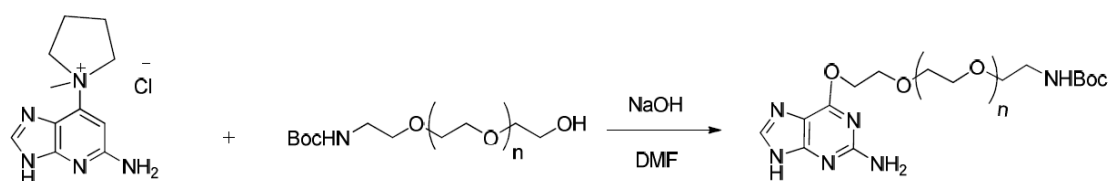


**Figure. 4-2.** *Synthesis of Guanine-O-PEG$_n$-NHBOC conjugate.*

### 4.4.3.3. Synthesis of Guanine-O-PEG$_n$-NH$_2$ conjugate

In a 10 mL round-bottom flask, 100 mg of Guanine-O-PEG$_n$-NHBOC conjugate was dissolved

in 3 mL of anhydrous dichloromethane, followed by 0.1 mL of trifluoroacetic acid (149 mg, 1.3 mmol, Sigma Aidrich, no. 302031) added and stirred overnight. Note that the whole reaction process is under nitrogen protection. Finally, the solvent was evaporated and yield desire product without any further purification.
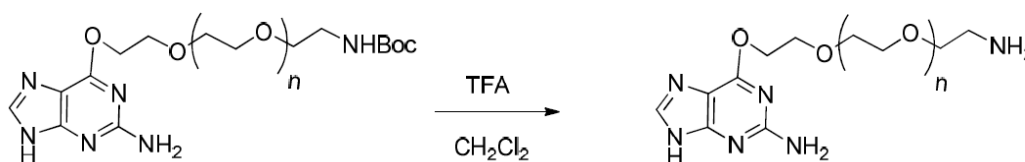


***Figure. 4-3.*** *Synthesis of Guanine-O-PEG$_n$-NH$_2$ conjugate.*

### 4.4.4. Characterization of PMA-AuNPs and Guanine-O-PEGn-NH$_2$ conjugate

### 4.4.4.1. Transmission electron microscopy (TEM) of PMA-AuNPs

The size and shape of PMA-AuNPs metal core were observed by TEM. Briefly, 10 µL of the diluted PMA-AuNPs were taken out and lightly dropped to the cooper grid covered with carbon film. After dried at room temperature, the images were captured by a JEM-1400PLUS HC TEM (JEOL, Germany). Corresponding histograms were analyzed by software Image J and Orign.

### 4.4.4.2. Dynamic light scattering (DLS) of PMA-AuNPs

The size distribution and hydrodynamic diameter $d_h$ of PMA-AuNPs were investigated by dynamic light scattering (DLS, Malvern NANO ZS, England). For that, the 10 µL of PMA-AuNPs stock solution was diluted with 1 mL MilliQ-water and placed in a UV-cuvette to equilibrate for 5 min at 25 °C. The measurement was performed using the DLS with a 173° scattering angle and 633 nm laser. The results were analyzed by software Orign and presented in number and intensity distribution.

### 4.4.4.3. UV/visible absorption spectra (UV-vis) of PMA-AuNPs

The UV/visible absorption spectra (UV-vis) of PMA-AuNPs was obtained by Ultraviolet–

visible spectroscopy (UV-Vis, Agilent 8453). 10 μL of PMA-AuNPs storage solution was adequately dispersed in 2 mL of MilliQ-water, transferred to a UV-cuvette and placed in the instrument to collect absorption spectra in the range of 300-800 nm. In addition, the concentration of nanoparticles can be calculated by UV absorption. According to previous reports[114], the concentration of 4 nm AuNPs can be calculated using the absorbance at 450 nm ($A_{450}$).

### 4.4.4.4. $^1$H NMR of synthesized conjugate

Synthesized 1-(2-amino-7H-purin-6-yl)-1-methyl-pyrrolidinium chloride and Guanine-O-PEG$_n$-NHBOC conjugate were weighed 20 mg and dissolved in 0.8 mL of DMSO-d$_6$ and CDCl$_3$, and the compositions was determined by $^1$H NMR spectroscopy (Bruker, America).

### 4.4.5. Conjugate discrete number of Guanine-O-PEG$_n$-NH$_2$ to PMA-AuNPs

After AuNP is coated with PMA, due to the presence of PMA, the surface is covered with many active carboxyl groups, which can be used to connect other functional ligands or small molecules. In the following, the discrete number (one or two) of guanine-PEG attachment were performed with 1-ethyl-3-(3-dimethylaminopropyl)carbodiimide hydrochloride (EDC). The reaction process is shown in Figure 4-4. The experimental procedures refer to the previous study of our group[131]. The PMA-AuNPs were dispersed in the sodium borate buffer (SBB, 50 mM, pH 9). According to the ratio stated in the paper, the concentration ratio of guanine-PEG and PMA-AuNPs is 500, c(PEG)/c(NP) = 500. Therefore, an aliquot of gram of guanine-PEG was dissolved in SBB to prepare the stock solution with concentration of 3 mM. Then, taken guanine-PEG and PMA-AuNPs of the same volume, mixed each other evenly, and divided into a series of 0.5 mL vials.

The amount of EDC added to the reaction determined how many guanine-PEG could be coupled to the PMA-AuNPs surface. In this case, we set a series of concentration ratio of EDC to PMA-AuNPs, c(EDC)/c(NP) = 32000, 16000, 8000, 4000, 2000, 1000, 500, 250, 125, 63, 31, 16, 8. To these, EDC was dissolved in SBB to get a concentration of 192 mM stock

solution, and the solution was diluted in half and half from high to low concentration successively. A series of diluted EDC solutions were taken out 10 μL and added into corresponding vials, and reacted at room temperature for 90 min. Gel electrophoresis was then carried out to separate PMA-AuNPs with one or two guanine-PEG conjugates to the surface.
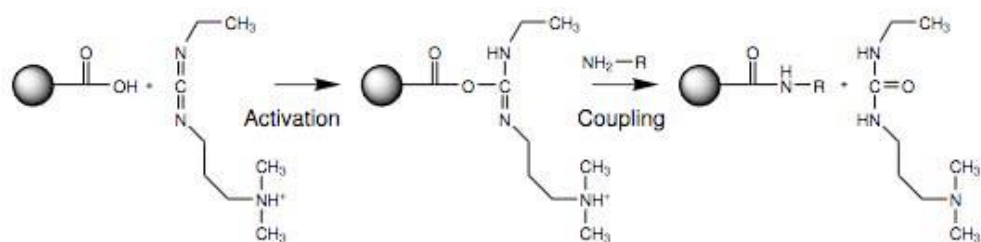


*Figure. 4-4.* *EDC activates the carboxyl group on the surface of NP and subsequent conjugate amino group via amide reaction. The figure was extract from reference[131].*

### 4.4.6. Gel electrophoresis

In this experiment, the effects of 0.5%, 1% and 2% agarose on separating 1 or 2 G-PEG attached PMA-AuNPs were compared. First, prepare the buffer solution required for electrophoresis and gel preparation, TBE buffer solution. For that, add 108 g of Tris base, 7.44 g of ethylenediaminetetraacetic acid (EDTA), 55 g of Boric acid to a 1 L volumetric flask, and add 800ml of MIlliQ-water and stir well to dissolve, then adjust the pH to 8.3, and dilute with water to make 1 L (445 mM Tris-boric, 10 mM EDTA) to get 10 × TBE buffer. For electrophoresis or gel preparation, we need to dilute 10 × TBE buffer to 0.5 × TBE buffer for use. Agarose was weighed according to the required gel concentration, such as 1% gel, 2 g agarose was weighed (w/v), put agarose powder into 500 mL conical flask and add 200 mL 0.5 × TBE buffer, then melt agarose in a microwave oven (800 w, 4 min). When heated, when the solution was boiled, carefully shake the conical flask to dissolve the agarose thoroughly. This operation was repeated several times until the agarose is completely dissolved. When the solution was cooled to 60-70 °C, the solution was poured into the gel tray and select a suitable comb was inserted into the gel. Leave it at room temperature for 40-50 min until the gel completely solidified.

Once solidified, the comb was gently pulled out and put the gel into the gel tank (BioRad), then 0.5 × TBE buffer was poured into the tank and covered the gel. Carefully added the sample (preparation as section 4.4.5.) into wells with pipette. Note, before loading the sample into the gel, the sample was mixed with 60% glycerinum so that can be deposited at the bottom of the well and not float in the buffer. After that, the electrophoresis device was connected to power source (BioRad Power Pac 1000) and ran for 60-80 min at 100 V.

At the end of the electrophoresis, the corresponding agarose gel was cut off (from top to bottom, the bands were 0 G-PEG attached NP, 1 G-PEG attached NP, 2 G-PEG attached NP) and placed in a dialysis bag. Filled the 0.5 × TBE buffer into the dialysis bag and put it in the electrophoresis tank to electrophoresis continued for 10-15 min, so that desired NP would be got out of agarose gel for collection. Then, 0.5 × buffer in the bag containing NP was transferred into a filter tube (Sigma Aldrich, Amicon® Ultra-4 Centrifugal Filter Unit 3 kDa, no. UFC800324) and washed with MilliQ-water four times to exchange the buffer with Milli-Q water and concentrated.

### 4.4.7. Determination of the concentration of scFv-SNAP

SNAP is provided by Prof.Davide Prosperi from the University of Bicocca in Italy. The classic protein determination method, the Coomassie blue assay, is used here to measure the concentration of SNAP. Simply, The BSA standard solution in the Thermo Scientific™ Coomassie (Bradford) Protein Assay Kit is diluted in sequence as shown in Table 2-1 to prepare a series of standard curving solutions. Then 30 μL of standard solution or diluted sample solution was mixed with 1.5 mL of Coomassie reagent solution that has returned to room temperature, and incubated at room temperature for 10 min. Subsequently, an Ultraviolet–visible spectroscopy (UV-Vis, Agilent 8453) was used to collect the absorbance of each sample at 595 nm sequentially.

### 4.4.8. Activity assay of scFv-SNAP

SNAP-Vista® Green (NEW ENGLAND BioLabs, England) is a green fluorescent substrate that can be used to label SNAP-tag fusion proteins (in cell lysates or purified proteins) for

detection by SDS-PAGE. The experiment was carried out following to manufacturer's protocol. In particular, 2 μL of substrate stock solution was mixed with 18 μL of (12.5 μg) SNAP sample and incubated at 37 °C for 30 min to bind the substrate to SNAP. After that, sample preparation was proceeded according to the requirements in polyacrylamide gel electrophoresis (SDS-PAGE) and run SDS-PAGE (for the detailed process, see section 4.4.10). After the gel is run, remove it from the glass plate and observe it immediately under a UV-transilluminator. The active SNAP bands showed an intense green fluorescence.

### 4.4.9. Conjugate scFv-SNAP to guanine-PEG-AuNPs

The purified guanine-PEG modified AuNPs and SNAP were gently mixed in 1 mL PBS (pH 7.4) at a molar ratio of 1:2 and incubated overnight at 4 °C. Then the mixture was transferred into a filter tube (Sigma Aldrich, Amicon® Ultra-4 Centrifugal Filter Unit 100 kDa, no. UFC800324) and washed with PBS five times by centrifuging at 5000 rpm for 10 min to remove unreacted SNAP and concentrated to a relatively high concentration.

### 4.4.10.    SDS-PAGE analysis of scFv-SNAP-PEG-AuNPs

Sodium dodecyl sulfate-polyacrylamide gel electrophoresis (SDS-PAGE) is a technique to separate proteins from samples based on their molecular weight. In this study, SDS-PAGE was used to evaluate scFv-SNAP conjugate to guanine-PEG-AuNPs. The specific experiment process is as follows. Firstly, the buffer solution needed for separating and stacking gel, running buffer and 10% of ammonium persulphate (AP) solution were prepared, respectively. Separating gel buffer solution (1.5 M, pH 8.8): 18.17 g Tris was added to a 100 mL volumetric flask, dissolved with MilliQ-water, and then adjusted pH value to 8.8 with 6 M HCl and filled with MilliQ-water to 100 mL. Stacking gel buffer solution (0.5 M, pH 6.8): 6.06 g Tris was added to a 100 mL volumetric flask and dissolved with MilliQ-water, then adjusted pH value to 6.8 with 6 M HCl and filled with MilliQ-water to 100 mL. For the running buffer, we usually prepared 10 × as stock solution and diluted 10 times during electrophoresis. 10 × running buffer containing 0.25 M Tris, 1.92 M Glycine and 0.1 % SDS with pH 8.3. Weighed 1 g of AP and dissolved in 10 mL MillIQ-water to prepare 10% of AP

solution. Note, it is necessary to divide AP solution into several 0.5 mL vials and stock in the freezer, otherwise, AP solution should be prepared fresh each time.

One short and one long glass plate were cleaned and assembled with clamps on both sides to fix them on the gel holder. Note that the bottom must be neatly sealed, and there should be a 1.5 mm gap between the two pieces of glass. Then prepare a 10% separating gel according to the order and volume shown in Table 4-1. After that, ~7 mL of separating gel solution was poured into a 1.5 mm gap, and overlaid with water to prevent contact with air, which inhibits polymerization. Allow acrylamide to polymerize for 20-30 min to form gel, then discard water and drain with filter paper.

**Table 4-1.** *Preparation of separating gel and stacking gel.*

| Regent | 10% separating gel | 5% stacking gel |
| --- | --- | --- |
| Acrylamide solution 40% | 2.5 mL | 0.5 mL |
| 1.5 M Tris, pH 8.8 | 2.5 mL | 0 |
| 0.5 M Tris, pH 6.8 | 0 | 1.25 mL |
| MilliQ-water | 4.95 mL | 3.23 mL |
| 10% AP solution | 100 μL | 50 μL |
| TEMED | 4 μL | 5 μL |

Prepared the stacking gel according to the above table and added it to the top of the separating gel with a pipette until it overflows. Then carefully insert the comb and wait for 20-30 min to let it solidify. Then, the clamps on the glass plates were removed and transferred to assembled electrophoresis cell, out of them into an electrophoresis tank. 1 × running buffer was poured into inner (upper) until overflow and outer (lower) buffer chambers to the indicator mark for 2 gels. After that, the comb was removed carefully and waited for loading samples.

For the sample preparation, 12 μL of prepared samples and protein standard were mixed with the same volume of loading buffer (Laemmli sample buffer containing 10% 2-mercaptoethanol, 0.004% Bromophenol blue, 20% Glycerol, 4% SDS and 0.125 M Tris-HCl),

respectively. Then, the samples were added to the wells and ran SDS-PAGE at 15 mA for 30 min, after changing to 25 mA for 1 h.

Staining of protein gels with Coomassie Brilliant Blue R-250 is a common procedure to visualize proteins resolved by SDS-PAGE. It is susceptible and is suitable for long-term storage of the gels. After the electrophoresis, remove the gel from the glass plates using a spatula and place it in a plastic tray containing Coomassie Blue solution (0.1% CBB R-250, 40% methanol and 10% Glacial acetic acid) and stain for 2-4 h. After staining, transfer the gel to destain solution (10% acetic acid and 5% ethanol) and place it on the rocking table for 4-6 h until clear blue bands are visualized on transparent background. Then, the gels could be stored in the gel store solution and photographed as required.

### 4.4.11. Dot blot analysis of scFv-SNAP-PEG-AuNPs

Dot blot is a simple and quick technique to determine if your antibodies and detection system are effective. Firstly, the PVDF membrane was activated by soaking methanol for 30 s and MilliQ-water for 1 min. Then, the membrane was locked on the equipment and dried via a vacuum. Secondly, 2 µg of 1-scFv-PEG-Au, 2-scFv-PEG-Au, or PMA-AuNPs, $NH_2$-PEG-AuNPs and scFv-SNAP were simply mixed as controls were dropped on the membrane carefully to make protein stick to the membrane. After the sample dried, the membrane was put in blocking solution (15 mL TBS buffer containing 5% skim milk and 0.05% Tween 20) for 2 h at room temperature. Pour off the block buffer, but keep the membrane wet at all times for the remainder of the procedure. Thirdly, the membrane was incubated with primary antibody, anti-His-tag (1:5000), in TBS buffer for 2 h. Then washed the membrane with 10 mL TBS buffer three times (10 min each time). After that, the membrane was incubated with secondary antibody, anti-HRP (1:3000), in TBS buffer for 1 h. Next, washed the membrane with 10 mL TBS buffer three times (10 min each time). And finally, immunoreactive spots were revealed using ECL Western blotting reagent (GE Healthcare).

### 4.5. Results and discussion

### 4.5.1. Characterization of PMA-AuNPs

Considering that the uniformity of particle size may affect the subsequent separation effect of agarose gel electrophoresis, this study used two methods, Brust-Schiffrin and Digestive ripening, to prepare 4nm AuNPs. The optical properties, particle size distribution and morphology of the synthesized PMA-AuNPs were characterized by UV and TEM. As shown in Figure 4-5a and b are the TEM images of AuNPs prepared by the two methods. The AuNPs prepared are spherical, but the uneven size distribution of AuNPs prepared by the Brust method can be visually observed. In sharp contrast, the AuNPs prepared by the digestive ripening method has uniform particle size. The average size of AuNPs prepared by the Brust method and digestive ripening method was calculated by counting to be 4.52 ± 1.38 nm and 5.34 ± 0.51 nm, respectively. Figure 4-5e shows the UV absorption spectrum of AuNPs. It can be seen that the UV maximum absorption peaks of AuNPs prepared by the two methods overlap, both are 520 nm, which is the plasma absorption peak of 4 nm AuNPs. In addition, the UV absorption peak of AuNPs prepared by the Brust method is significantly broader than that prepared by the digestive ripening method, which also indicates that the nanoparticles prepared by the latter approach are more uniform in size. Based on the above, we choose AuNPs prepared by the digestive ripening method for subsequent experiments.
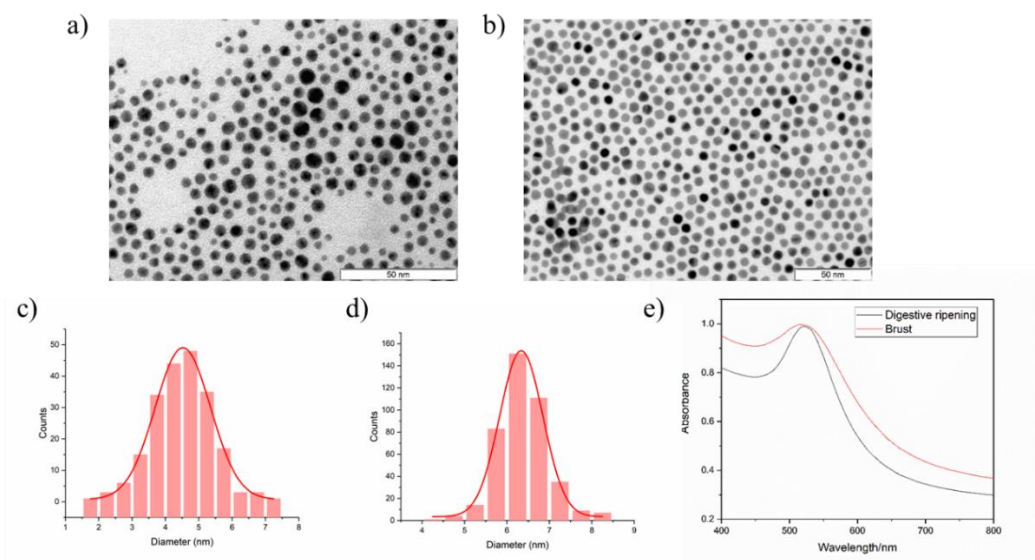


*Figure. 4-5.* *TEM image of size distribution of AuNPs prepared by a) Brust method and b) Digestive ripening method. TEM figures were captured by Stefan Werner form Chemistry department. The corresponding histogram of AuNPs prepared by c) Brust method and d) Digestive ripening method, size is 4.52 ±1.38 nm and 5.34 ±0.51 nm, respectively. e) UV spectra of AuNPs with different method.*

### 4.5.2. Characterization of Guanine-O-PEGn-NH₂ conjugate

#### 4.5.2.1. ¹H NMR of 1-(2-amino-7H-purin-6-yl)-1-methyl-pyrrolidinium chloride
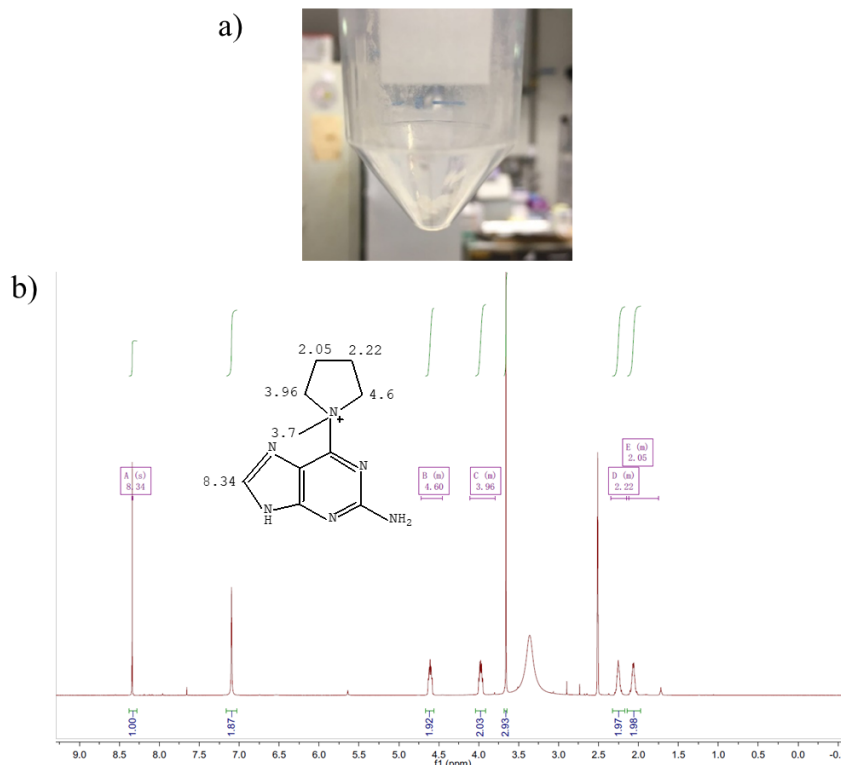


**Figure. 4-6.** *a) The appearance of 1-(2-amino-7H-purin-6-yl) -1-methyl-pyrrolidinium chloride. b) ¹H NMR of 1-(2-amino-7H-purin-6-yl) -1-methyl-pyrrolidinium chloride. The ¹H NMR was obtained by NMR-spectra service from chemistry department.*

The synthesized 1-(2-amino-7H-purin-6-yl)-1-methyl-pyrrolidinium chloride was washed with ethyl ether and dried. The final product obtained was a white solid powder with a yield of about 48%. The structure of the obtained product was determined by nuclear magnetic resonance, and its ¹H NMR is shown in Figure 4-6b. The assignment of each peak is as follows: ¹H-NMR (400 MHz, DMSO-$d_6$): δ (ppm) 2.05 (m, 2H, -CH2-, pyrrolidin), 2.22 (m, 2H, -CH2-, pyrrolidin), 3.70 (s, 3H, -CH3), 3.96 (m, 2H, -CH2-N+-, pyrrolidin), 4.60 (m, 2H, -CH2-N+-, pyrrolidin), 7.11 (s, 2H, -NH2), 8.34 (s, 1H, H8), 13.38 (s, 1H, H9). The ¹H NMR peak of the obtained product is consistent with that reported in the literature[36], indicating that the synthesis is successful.

### 4.5.2.2. ¹H NMR of Guanine-O-PEG$_n$-NHBOC conjugate
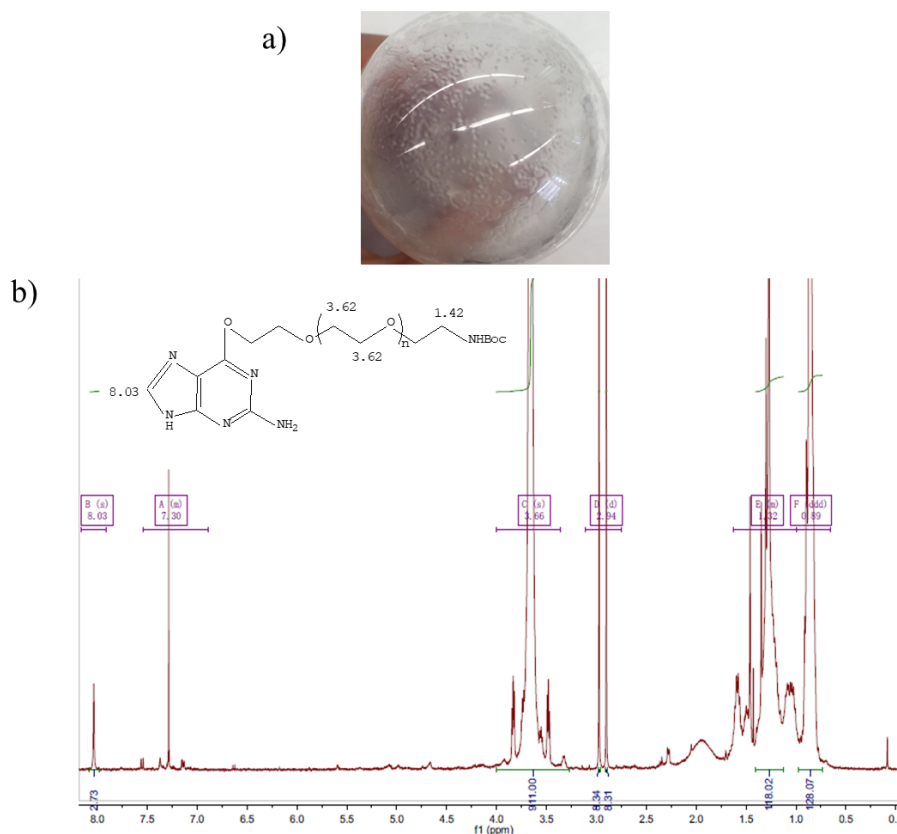


**Figure. 4-7.** *a) The appearance of Guanine-O-PEG$_n$-NHBOC conjugate. b) ¹H NMR of Guanine-O-PEG$_n$-NHBOC conjugate. The ¹H NMR was obtained by NMR-spectra service from chemistry department.*

Conjugate the 5kDa HO-PEG$_n$-NHBOC to the product obtained in the previous step by nucleophilic substitution to obtain Guanine-O-PEG$_n$-NHBOC, a derivative of guanine. After the product is purified by a PD-10 column, a light-yellow slurry solid desire product is obtained. The ¹H NMR is shown in Figure 4-7b, and the specific assignments are as follows: ¹H-NMR (400 MHz，CDCl$_3$) δ (ppm) 1.42 (t-BuO-), 3.62 (-O-CH 2-CH 2-O-), 8.03 (H8). Consistent with the description in the literature[36], indicating the successful synthesis of Guanine-O-PEG$_n$-NHBOC.

### 4.5.2.3. ¹H NMR of Guanine-O-PEG$_n$-NH₂ conjugate

TFA was used to remove the BOC protecting group on Guanine-O-PEG$_n$-NHBOC to obtain a

guanine derivative with active NH$_2$. The $^1$H NMR is shown in Figure 4-8, the BOC peak at 1.42 ppm disappeared, indicating that BOC was successfully removed and the final desired product was obtained.
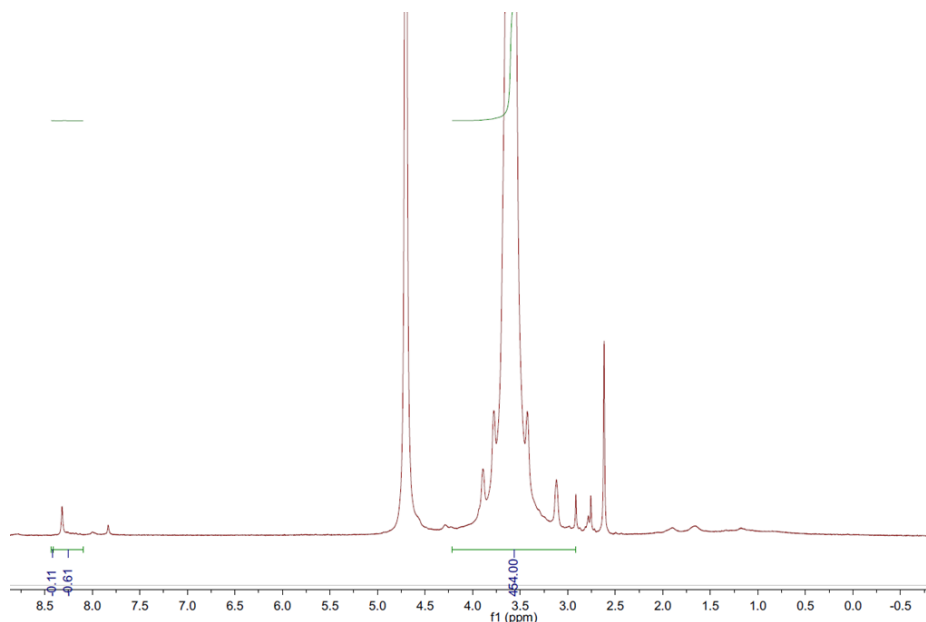


***Figure. 4-8.*** *$^1$H NMR of Guanine-O-PEG$_n$-NH$_2$ conjugate. The $^1$H NMR was obtained by NMR-spectra service from chemistry department.*

### 4.5.3. Separate AuNPs conjugated with different numbers of Guanine-O-PEG$_n$-NH$_2$ (BG-AuNPs) by gel electrophoresis

When molecules are placed in an electric field, they will move to the appropriate electrode with a fixed velocity. This rate of migration of molecules under the electric field is called electrophoresis mobility. It is proportional to the strength of the electric field and the amount of net charge carried by the electrophoretic molecule itself. In other words, the higher the electric field intensity and the more net charge the electrophoresis molecules carry, the faster migration speed will be, and vice versa. Agarose gel electrophoresis is an electrophoresis method that uses agarose as a supporting medium. Because agarose has a network structure, the substance molecules will encounter resistance when they pass through. It has the dual functions of "molecular sieve" and "electrophoresis" (Figure 4-9). The particle size of PMA-AuNPs would be different when the different number of ligands are attached to the surface of PMA-AuNPs. Based on this assumption, we use agarose gel

electrophoresis to separate, collect and characterize PMA-AuNPs with the discrete number of 1 or 2 G-PEG attached.
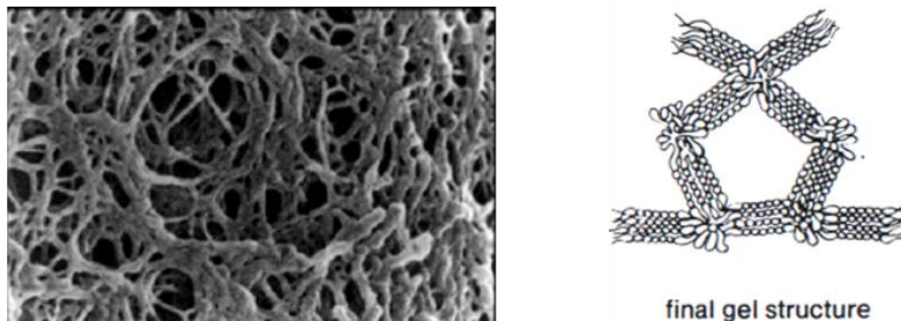


*Figure. 4-9. Scanning Electron Microscopic view of agarose gel and structure of agarose gel. The figure was extract from website: http://home.sandiego.edu/~josephprovost/AGAROSE%20GELS.pdf*

### 4.5.3.1. The influence of agarose concentration on separation

The concentration of agarose determines the pore size of the molecular sieve, which affects the mobility of the nanoparticles. Therefore, we investigated the separation of AuNPs in different concentrations of agarose gel electrophoresis. 0.5%, 1% and 2% agarose gels were used, and AuNPs were coupled by $NH_2$-PEG-$NH_2$ instead of Guanine-O-$PEG_n$-$NH_2$ to screen out the most suitable separation conditions. AuNPs are coupled with different numbers of PEG ligands on the surface under the action of different concentrations of EDC, and exhibit different mobility in agarose gel electrophoresis. The results are shown in Figure 4-10. First, the gel formed after the solidification of low-concentration agarose is low in hardness and large in pore size, which can be intuitively observed from the appearance of 0.5%, 1% and 2% agarose gels in the experiment. The gel formed by 0.5% agarose is almost transparent, while the gel formed by 1% and 2% agarose is white, indicating sufficient hardness and support. In addition, due to the large pore size of the 0.5% gel, the migration speed of AuNPs in the gel is fast (Figure 4-10a). Under the same electrophoresis conditions, even if the AuNPs have migrated out of the gel, the AuNPs with different numbers of PEG attached to the surface cannot be separated. In contrast, AuNPs with different numbers of PEGs on the surface showed different mobility in 1% and 2% gel

with smaller pore size. From top to bottom, the clearer bands are 0 PEG-linked AuNPs and 1 PEG-linked AuNPs (1-PEG-Au), respectively (Figure 4-10a, b). In conclusion, 1% agarose gel can well separate the 4nm AuNPs with 0 or 1 PEG ligand.
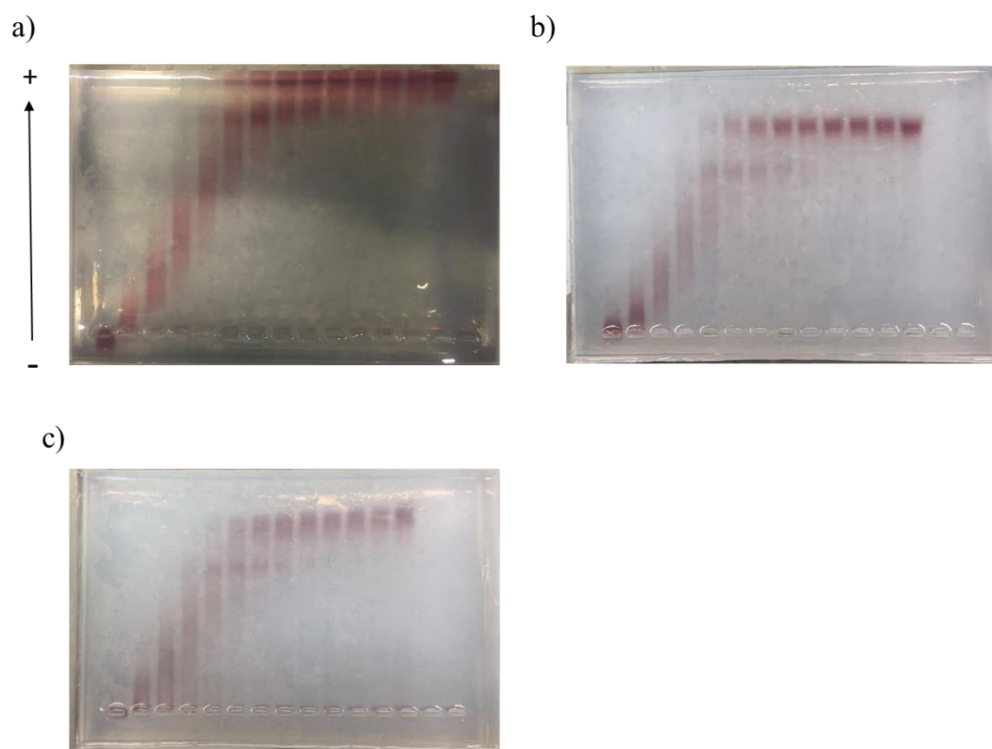


*Figure. 4-10. Gel electrophoresis separation with different concentration agarose of AuNPs conjugated with NH2-PEG-NH2 (Mw: 10000). The concentration of agarose is a) 0.5%, b) 1% and c) 2%. Channel (1-13) from left to right are, $C_{EDC}/C_{NP}$ = 32000, 16000, 8000, 4000, 2000, 1000, 500, 250, 125, 63, 31, 16, 8. Channel (14) is control, AuNPs without PEG and EDC. $C_{PEG}/C_{NP}$ = 500, $C_{NP}$ = 3 μM.*

### 4.5.3.2. The influence of nanoparticles purification on separation

In order to ensure that AuNPs obtain a stable and uniform PMA coating, excessive PMA is added during the coating process. PMA is an amphiphilic polymer, which cannot be removed in the general purification process. Therefore, there is a large amount of free PMA in the PMA-AuNPs solution finally obtained. When PEG was conjugated to the surface of AuNP, free PMA could compete with PMA on the surface of AuNPs. This process not only consumes a large amount of EDC, but also requires a large amount of PEG. Therefore, it is

necessary to purify AuNPs to remove excess PMA. The particle size of AuNPs was 4 nm, and the supernatant containing PMA was replaced with MIlliQ water by ultra-high-speed centrifugation at 60000 rpm for 30 min, as shown in Figure 4-11. Note that multiple high-speed centrifugations can easily lead to irreversible aggregation and precipitation of nanoparticles, and this step can be repeated twice to remove free PMA.
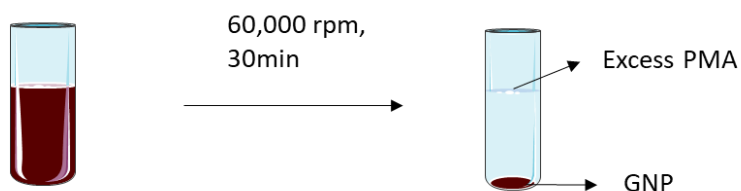


**Figure. 4-11.** *Schematic of nanoparticle purification.*

The AuNPs before and after purification were reacted with PEG in different concentrations of EDC, and the samples were characterized and separated by 1% agarose electrophoresis. Results as shown in Figure 4-12a, the concentration of EDC required for unpurified AuNPs was $C_{EDC}/C_{NP}$ = 32000, 16000, 8000, 4000, 2000, 1000, 500, 250, 125, 63, 31. When the concentration of EDC is $C_{EDC}/C_{NP}$ = 32000, 16000, 8000, 4000, 2000, 1000, the AuNPs surface has been coupled with at least four or more PEG, resulting in the overall particle size becoming larger, unable to pass through the pore size of the gel, remaining in the sample adding hole. When $C_{EDC}/C_{NP}$ = 500, 250, 125, 63, 31, tailing bands appear in the sample during electrophoresis, indicating that 1, 2, or 3 PEG ligands are coupled to the surface of AuNPs. Especially when $C_{EDC}/C_{NP}$ = 63, 31, two clear bands appear, from top to bottom, there are 0 PEG-Au and 1-PEG-Au, respectively. The electrophoresis results of the purified AuNPs are shown in Figure 4-12b. The ratio of tailing bands is $C_{EDC}/C_{NP}$ = 256, 128, 64, 32, 16, 8, 4, 2, 1, which compared with unpurified AuNPs, the amount of EDC is reduced by half. And when $C_{EDC}/C_{NP}$ = 1, the results show that there is already 1 PEG attached to the surface of some AuNPs. However, when $C_{EDC}/C_{NP}$ = 32, 16, AuNPs coupled with 1 PEG were the most, and showed a clear third band, that is, AuNPs coupled with 2 PEGs. In addition, it is worth noting that the ratio of PEG to AuNPs after purification has been reduced by ten times from $C_{EDC}/C_{NP}$ = 500 to $C_{EDC}/C_{NP}$ = 50, which significantly saves the amount of PEG. In summary, the purification of AuNPs can remove excess PMA and reduce the amount of

EDC and PEG required in the coupling process.
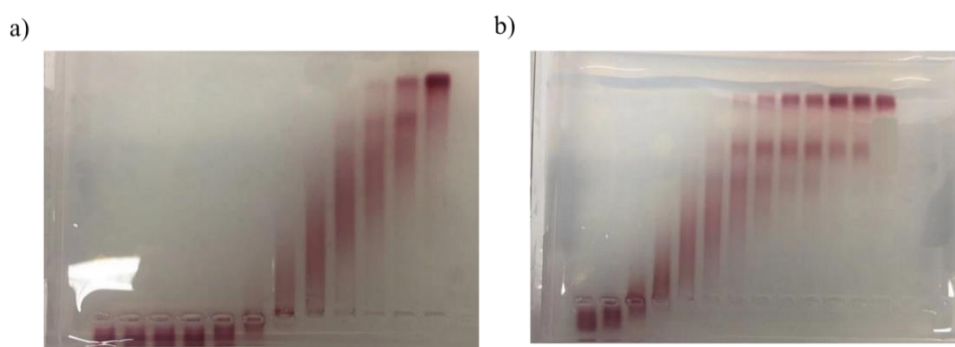


***Figure. 4-12.*** *Effect of AuNPs purification on gel electrophoresis separation. a) AuNPs before purification. Channels (1-11) from left to right are, $C_{EDC}/C_{NP}$ = **32000, 16000, 8000, 4000, 2000, 1000, 500, 250, 125, 63, 31**. Channel (12) is control, AuNPs without PEG and EDC. $C_{NP}$ = 6 μM, $C_{PEG}/C_{NP}$ = 500. b) AuNPs after purification. Channels (1-12) from left to right are, $C_{EDC}/C_{NP}$ = **2048, 1024, 512, 256, 128, 64, 32, 16, 8, 4, 2, 1**. Channel (13) is control, AuNPs without PEG and EDC. $C_{NP}$ = 6 μM, $C_{PEG}/C_{NP}$ = 50.*

According to the above results, the optimal conditions for 1-G-PEG-Au and 2-G-PEG-Au were as follows: the ratio of purified AuNPs to Guanine-O-PEG$_n$-NH$_2$ was 50, $C_{EDC}/C_{NP}$ = 32,16, and separation by 1% agarose gel. And use this condition to carry out the large scale reaction, as shown in Figure 4-13a, the result shows three clear bands, namely PMA-AuNPs, 1-G-PEG-Au and 2-G-PEG-Au. After cutting the 1-G-PEG-Au and 2-G-PEG-Au bands, they are placed in a dialysis bag to continue electrophoresis to collect the desired nanoparticles. Perform gel electrophoresis on the collected 1-G-PEG-Au and 2-G-PEG-Au again to confirm the number of G-PEG attached to the surface of AuNPs. The results are shown in Figure 4-13b, which is consistent with previous literature reports[131]. From top to bottom, AuNPs without PEG has the fastest migration rate, which is the first band; AuNPs coupled with 1 G-PEG, the particle size changes significantly, and the migration rate is also significantly slower than the control PMA-AuNPs, which is the second band; The particle size of AuNPs with two G-PEGs is theoretically significantly larger than 1-G-PEG-Au, and its migration rate is the slowest, which is the third band.
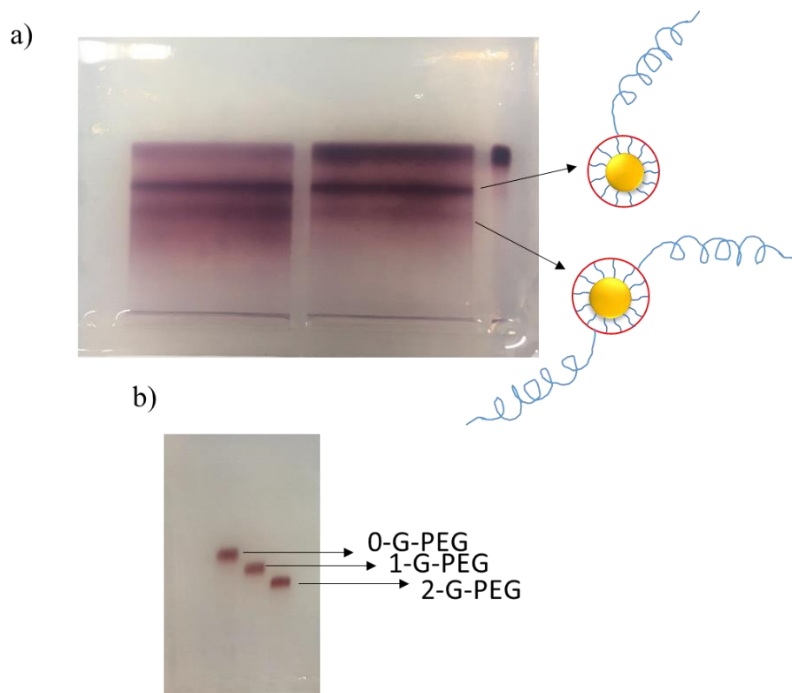
*Figure. 4-13.* a) PMA-AuNP after the EDC coupling with Guanine-PEG$_n$-NH$_2$ in a 1% agarose gel. Channels (1-2) from left to right are, $C_{EDC}/C_{NP}$ = 32, 16. Channel (3) is control, AuNPs without PEG and EDC. $C_{NP}$=14μM, $C_{PEG}/C_{NP}$=50. b) Gel electrophoresis of collected 1-G-PEG-Au and 2-G-PEG-Au.

### 4.5.4. scFv-SNAP activity assay

SNAP-tag protein is a mutant of O$^6$-alkylguanine-DNA-alkyltransferase (hAGT) of human DNA repair protein, consisting of 182 amino acids (20kDa). It can react quickly and specifically with benzylguanine (BG) and its derivatives, thereby forming a stable thioether bond between the SNAP-tag protein and the substrate, with fast reaction speed and high specificity[36, 41]. Taking advantage of the single-chain antibody fragment (scFv) expression sequence is inserted into the SNAP-tag-encoding plasmid backbone (as shown in Figure 4-14), and the scFv-SNAP obtained by vector expression can quickly and directionally fix the scFv on the surface of AuNPs. In order to detect whether the obtained scFv-SNAP has the ability to bind to O$^6$-guanine derivatives specifically, we used fluorescein-based BG derivative SNAP-Vista® Green as a substrate (SVG) for activity testing. SDS-PAGE after the reaction between SNAP-tag and SVG can be visualized as a fluorescent band, thereby judging the specific binding activity of SNAP-tag. After the SVG is co-incubated, scFv-SNAP

would specifically replace the guanine on the SVG to obtain fluorescence, and the reaction can still be maintained in SDS-PAGE. We tested the activity of different batches of scFv-SNAP, and the results are shown in Figure 4-15a. All scFv-SNAP showed a single band of about 45kDa on SDS-PAGE, which was consistent with the actual molecular weight of the protein. Some batches of scFv-SNAP also showed bands at other molecular weights, which may be caused by incomplete purification or partial decomposition. After co-incubation with SVG, all batches of scFv-SNAP showed a green fluorescent band under UV lamp, indicating that the obtained scFv-SNAP could react specifically with BG derivatives.
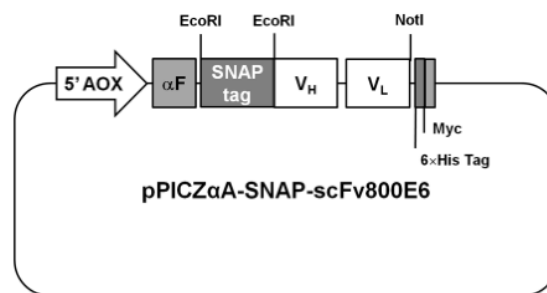


*Figure. 4-14. Schematic diagram of the pPICZ αA-SNAP-scFv800E6 expression vector. The recombinant gene encoding SNAP tag was inserted into the pPICZ αA-scFv800E6 vector under the control of the alcohol-oxidase-1 (AOX1) promoter, in frame with the prepro-αfactor signal sequence (αF) and with Myc and histidine (6 ×His) tags. scFv-SNAP Provide by Prof.Davide Prosperi.*
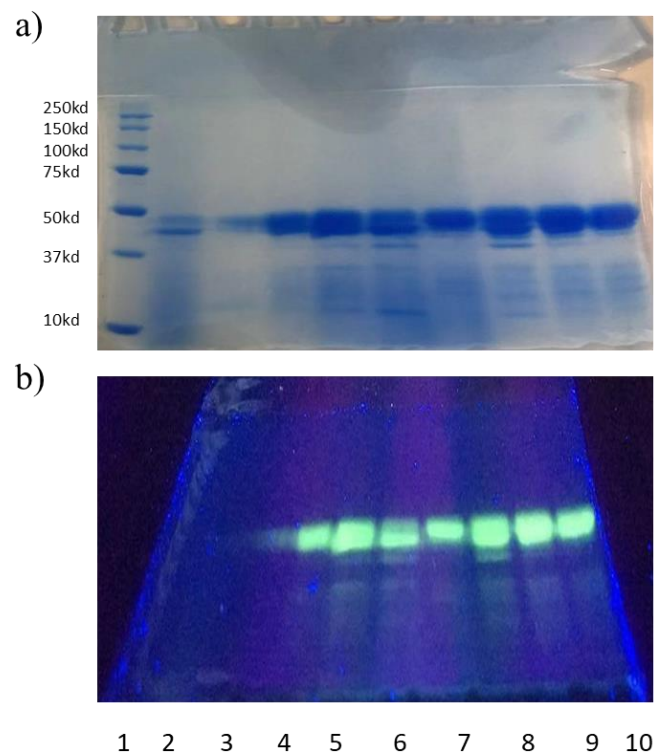
*Figure. 4-15.* *Activity of different batches of SNAP. a) SDS-PAGE of scFv-SNAP incubated with SVG. b) SDS-PAGE of scFv-SNAP incubated with SVG under UV light. Channel (1) is protein standard (without fluorescence). Channel (2) is scFv-SNAP protein (5ug, without SVG). Channel (3-10) are different batches of scFv-SNAP samples with SVG.*

### 4.5.5. SDS-PAGE analysis of scFv-SNAP-PEG-AuNPs

In the co-incubation process of scFv-SNAP and conjugated with one or two G-PEG-Au, scFv-SNAP would react specifically with the BG group on G-PEG, so that scFv could be fixed on the surface of AuNPs directionally[41, 132]. SDS-PAGE was used to verify the hypothesis that scFv-SNAP binds specifically to the surface of AuNPs. scFv-PEG-Au after the reaction was washed to remove unreacted scFv-SNAP, and PMA-AuNPs, $NH_2$-PEG-AuNPs and scFv-SNAP were simply mixed as controls. The results are shown in Figure 4-16, the single scFv-SNAP showed a single band on SDS-PAGE, about 45kDa, which was consistent with the previous results. AuNPs showed no bands either with only PMA coating or with one or two G-PEG ligands or $NH_2$-PEG ligands conjugation (channel 3, 4 in Figure 4-16a and channel 3, 5, 6 in Figure 4-16b), proving that only scFv-SNAP conjugation to AuNPs surface showed bands in

SDS-PAGE. Secondly, both 1-G-PEG-Au and 2-G-PEG-Au reacted with scFv-SNAP and showed bands in SDS-PAGE at the same position as scFv-SNAP, indicating that scFv-SNAP was coupled to the AuNPs surface (channel 5 in Figure 4-16a and channel 7 in Figure 4-16b). However, when PMA-AuNPs or 2-NH$_2$-PEG-Au without BG derivative ligand conjugation is mixed with scFv-SNAP, the sample still shows a single band consistent with scFv-SNAP in SDS-PAGE, even after cleaning for more than ten times (channel 6 in Figure 4-16a and channel 4, 8 in Figure 4-16b), which indicated that scFv-SNAP protein would non-specifically adsorb on the surface of AuNPs. Based on the above results, scFv-SNAP can react with one or two G-PEG ligands coupled to the surface of AuNPs to immobilize scFv on the surface of AuNPs. However, there is non-specific adsorption in this process, which will affect the directional immobilization and number control of scFv on the surface of AuNPs.
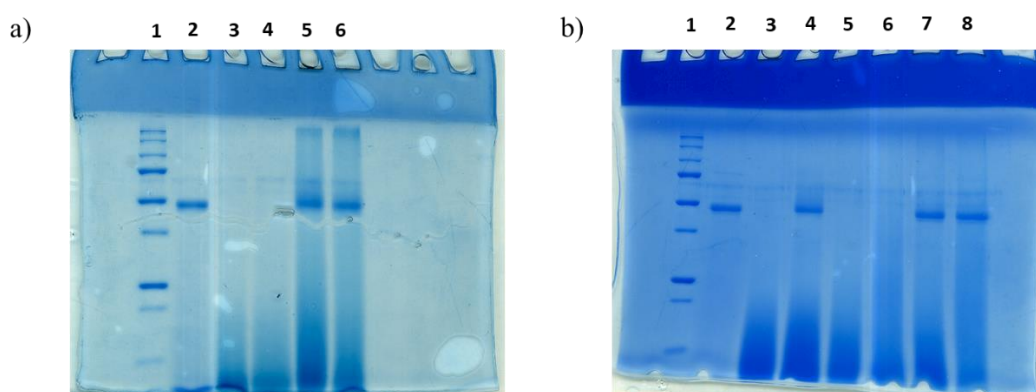


*Figure. 4-16. SDS-PAGE of scFv-SNAP conjugate to AuNPs. a) SDS-PAGE of one scFv-SNAP conjugate to AuNPs. Channel (1) is protein standard, (2) is scFv-SNAP, (3) is PMA-AuNPs, (4) is 1-G-PEG-Au, (5) is 1-scFv-PEG-Au, (6) is scFv-SNAP mixed with 1-NH$_2$-PEG-Au. b) SDS-PAGE of two scFv-SNAP conjugate to AuNPs. Channel (1) is protein standard, (2) is scFv-SNAP, (3) is PMA-AuNPs, (4) is PMA-AuNPs mixed with scFv-SNAP (PMA-SNAP). (5) is 2-G-PEG-Au, (6) is 2-NH$_2$-PEG-Au, (7) is 2-scFv-PEG-Au, (8) is scFv-SNAP mixed with 2-NH$_2$-PEG-Au.*

### 4.5.6. Dot blot analysis of scFv-SNAP-PEG-AuNPs

We use Dot blot to detect further whether scFv is immobilized on the surface of AuNPs. PVDF membrane can be used as a solid phase to adsorb the scFv dropped on it. Since the

sequence of scFv-SNAP contains His-tag expression sequence (Figure 4-14), anti-His-tag can react with the scFv-SNAP on PVDF membrane for antigen-antibody reaction. Then the HRP enzyme-labeled secondary antibody can specifically bind to the bound primary antibody anti-His-tag to form an antigen-antibody-HRP enzyme-labeled secondary antibody complex[133] on the membrane. When the complex is incubated with the luminescent solution, the luminescent solution A and B undergo a chemical reaction under the catalysis of the HRP enzyme to emit fluorescence[134-135], and the sample containing the scFv would be developed. The results are shown in Figure 4-17, the spots exhibited by scFv-SNAP are the brightest, indicating that it binds specifically to anti-His-tag and anti-HRP, which also proves the feasibility of dot blot verification. After PMA-Au was incubated with the antibody, no fluorescent signal was detected, indicating that no non-specific binding occurred, consistent with the SDS-PAGE results. Both 1-scFv-PEG-Au and 2-scFv-PEG-Au showed weak spots, meaning that less scFv was adsorbed on the surface of the PVDF membrane. Theoretically, the loading amount of scFv in these two groups is twice that of the control group, and its spot brightness should be higher than that of the control group. However, due to the steric hindrance of the nanoparticles, the scFv exposed on the surface of the PVDF film was less than that of the control group. In addition, ligands without BG derivatives, such as PMA coating, $NH_2$-PEG, also show spots with brightness comparable to 1-scFv-PEG-Au and 2-scFv-PEG-Au, suggesting that scFv-SNAP was adsorbed on AuNPs surface in these samples, which was also consistent with SDS-PAGE results. In the above results, there is no evidence that scFv in 1-scFv-PEG-Au or 2-scFv-PEG-Au is specific binding or non-specific adsorption, so the orientation of scFv on AuNPs surface cannot be guaranteed, and further experiments are needed to prove it.
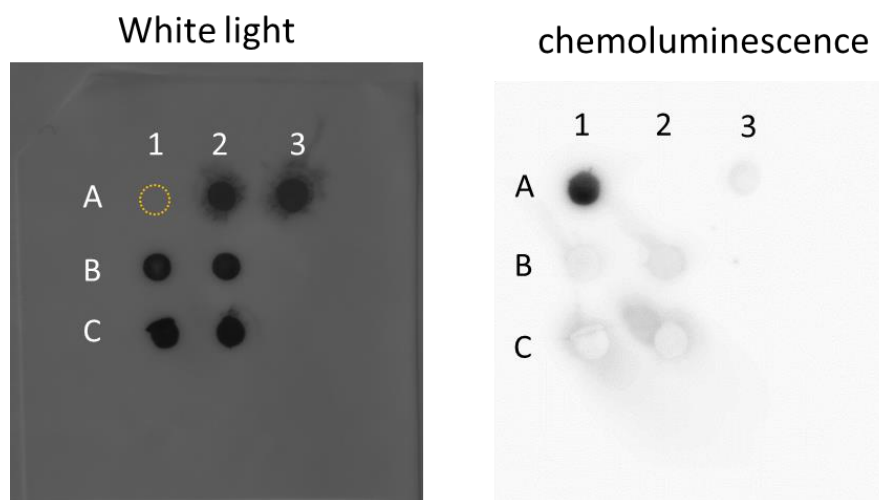
***Figure. 4-17.*** *Dot blot assay of scFv-SNAP conjugate to AuNPs. A: 1 to 3 are scFv-SNAP (1 µg), PMA-Au and PMA-Au mixed with scFv-SNAP, respectively. B: 1 to 2 are 1-NH$_2$-PEG-Au mixed with scFv-SNAP and 1-scFv-PEG-Au (2 µg), respectively. C: 1 to 2 are 2-NH$_2$-PEG-Au mixed with scFv-SNAP and 2-scFv-PEG-Au (2 µg), respectively. They were filtered on a PVDF membrane and probed with an anti-Myc-HRP antibody. Immunoreactive spots were revealed with an ECL substrate.*

## 4.6. Conclusion

Nanoparticles are small in size and easily overcome biological barriers to enter cells, so they have a certain degree of targeting: high permeability and long retention effect (EPR). Still, they have shortcomings such as being easily swallowed by the reticuloendothelial system (RES)[136]. Therefore, in recent years, modifying the surface of nanocarriers to prepare active targeting nanocarriers to improve their targeting has become one of the hotspots of research. However, the most specific recognition is the unique expression or overexpression of antigens and surface receptors by diseased cells. Therefore, nanoparticles can recognize these molecular entities by coupling specific molecules such as antibodies, peptides, DNA or RNA, etc., to increase the active targeting specificity of drug delivery and improve the efficacy[137]. Antibodies are specific and have strong binding ability to corresponding antigens. They are one of the most widely used targeting ligands in nanocarriers[41]. However, due to the large volume of antibody molecules, the infiltration of antibody-conjugated nanoparticles into tissues is impeded and the distribution of

antibody-conjugated nanoparticles in cells is limited. In addition, antibody-conjugated nanoparticles often cause changes in the three-dimensional structure of antibodies[138]. In order to overcome the obstacles related to antibody size affecting antibody efficiency, recombinant antibodies have been specifically developed. One of the most widespread applications is single-chain variable fragment antibody (scFv), the smallest functional structural unit with all the antigen-binding specificities of the complete antibody[139].

The coupling of antibodies and nanoparticles can be divided into the non-covalent coupling and covalent coupling. The former is a physical method of non-covalent bonding, such as electrostatic attraction, which has a weak binding force; the latter uses chemical bonding, which mainly includes sugar modification, amino or carboxyl modification, sulfhydryl modification, etc., with high stability[41]. However, these are arbitrary immobilization methods, which will cause 1) the unorientation of antibody binding, the active site is shielded, and the targeting efficiency is reduced[140]; 2) influencing the stability of the antibody, the covalent binding site on the antibody may destroy the folding stability of its spatial structure[138]. Therefore, during the antibody coupling process, the correctness of the antibody orientation must be ensured under the premise of a stable connection. The fusion tag method is currently a research hotspot in the targeted immobilization of proteins. A fusion tag is introduced into a specific part of the target protein, and the protein is fixed on the surface of the carrier through the specific reaction of the tag without damaging the normal function of the protein[41, 141].

So far, various protein tags have been developed to study protein systems in living bodies, and SNAP-tag is one of the best fusion tags. SNAP-tag is a variant of human DNA alkyltransferase (hAGT), specifically covalently linked to $O^6$ benzylguanine (BG)[54] and its derivatives[142]. At present, studies have[36, 143] shown that SNAP-tag fusion of scFv and specific binding of BG functionalized effector molecules to achieve antibody homogeneously labeled, which not only directionally fixed the antibody on the surface of nanoparticles, but also significantly reduced the mutual interference between antibodies and effector molecules. In addition to optimizing antibody targeting efficiency through the above strategies, researchers also need to consider the antibody density on the surface of the

nanoparticles. When the antibody density is too high, the interaction between the antibody and the antigen may be hindered due to steric hindrance[41].

In this work, we developed a direct method to achieve the orientated immobilization of discrete numbers of antibodies on the AuNP surface. First, 4 nm AuNPs with highly uniform particle size were synthesized by the digestive ripening method, and PMA coating was applied for subsequent ligand modification. In order to reduce the influence of antibody size and immobilized direction on the targeting efficiency, we inserted the expression sequence of SNAP-tag into the plasmid skeleton expressing scFv, and obtained the scFv fused with SNAP-tag at the N-terminal. SNAP-tag can form a stable thioether bond with BG derivatives, which can orient the fused protein to the nanoparticle. For this reason, we successfully synthesized a PEG ligand with a BG group on one terminal and an amino group on the other. Previous studies[131] have shown that the carboxyl group on PMA can react with amino groups for functional modification, and the number of amino ligands can be precisely controlled by EDC and separated by gel electrophoresis. Based on this, we optimized the conditions for gel electrophoresis to separate and couple 1 or 2 G-PEGs to AuNPs. Finally, the optimal conditions were determined as follows: PMA-AuNPs purified by ultracentrifugation reacted with G-PEG, the molar concentration ratio of PEG/NP was 50:1, the molar concentration ratio of EDC/NP was 32:1, 16:1, and the separation was performed in gel electrophoresis with 1% agarose concentration after 2h reaction. In addition, we co-incubated scFv-SNAP with a green fluorescent BG substrate, and the green fluorescent band displayed in SDS-PAGE also indicated the specific binding of scFv-SNAP to BG. We reacted 1-G-PEG-AuNP and 2-G-PEG-AuNP with scFv-SNAP at a molar ratio of 1:2 overnight. After washing, SDS-PAGE and Dot blot were performed to characterize the scFv bands. Both 1-G-PEG-AuNP and 2-G-PEG-AuNP incubated with scFv-SNAP showed protein bands, indicating that scFv was bound to BG-PEG. However, when scFv-SNAP was incubated with NH$_2$-PEG-AuNP, SDS-PAGE also showed bands, indicating that scFv could non-specifically adsorb on the AuNP surface. This may be because AuNP is only coupled with a discrete number of PEG, and there are many negatively charged carboxyl groups left in the PMA coating on the surface, leading to t non-specifically adsorption of protein. In summary, although scFv-SNAP specifically binds to BG-PEG-AuNP, the non-specific adsorption on the

AuNP surface cannot be removed completely, which may affect the subsequent targeting investigation.

In order to ensure the specific adsorption of scFv on the AuNP surface and the accuracy of the subsequent targeting investigation, it is necessary to minimize the formation of the protein corona. Polyethylene glycol (PEG) is currently the most widely used anti-non-specific adsorption material. PEG is extremely hydrophilic and electrically neutral over a wide range of pH blocks the electrostatic interaction between the matrix and the protein[144]. In addition, PEG can provide a more significant steric hindrance, which is conducive to blocking non-specifically adsorbed substances far away from the substrate surface, and further controls the occurrence of non-specific adsorption[144-145]. Zwitterionic compounds such as phosphocholine, thiobetaine and carboxybetaine polymers represent a new type of anti-non-specific protein adsorption material that can replace traditional polyethylene glycol polymers[146-147]. This kind of material molecules contain super hydrophilic anion and cationic groups at the same time, the total charge is neutral, and can highly form hydrogen bonds with water molecules, which wraps the nanoparticles and reduces the effect of Coulomb attraction[148-149], thus preventing non-specific adsorption of proteins. Therefore, two strategies can be used to reduce the non-specific adsorption of AuNPs on the surface: 1) G-PEG-AuNPs surface coupled with shorter PEG to resist non-specific adsorption of proteins; 2) zwitterionic polymerization instead of PMA for AuNPs surface coating.

# References

1.      Ryvolova, M.; Chomoucka, J.; Drbohlavova, J.; Kopel, P.; Babula, P.; Hynek, D.; Adam, V.; Eckschlager, T.; Hubalek, J.; Stiborova, M.; Kaiser, J.; Kizek, R., Modern Micro and Nanoparticle-Based Imaging Techniques. *Sensors* **2012,** *12* (11), 14792-14820.

2.      Han, X.; Xu, K.; Taratula, O.; Farsad, K., Applications of nanoparticles in biomedical imaging. *Nanoscale* **2019,** *11* (3), 799-819.

3.      Loudos, G.; Kagadis, G. C.; Psimadas, D., Current status and future perspectives of in vivo small animal imaging using radiolabeled nanoparticles. *European Journal of Radiology* **2011,** *78* (2), 287-295.

4.      Hsu, J. C.; Nieves, L. M.; Betzer, O.; Sadan, T.; Noël, P. B.; Popovtzer, R.; Cormode, D. P., Nanoparticle contrast agents for X‐ray imaging applications. *WIREs Nanomedicine and Nanobiotechnology* **2020,** *12* (6).

5.      Hainfeld, J. F.; Slatkin, D. N.; Focella, T. M.; Smilowitz, H. M., Gold nanoparticles: a new X-ray contrast agent. *The British Journal of Radiology* **2006,** *79* (939), 248-253.

6.      Krause, W.; Schneider, P. W., Chemistry of X-Ray Contrast Agents. In *Contrast Agents II: Optical, Ultrasound, X-Ray and Radiopharmaceutical Imaging*, Krause, W., Ed. Springer Berlin Heidelberg: Berlin, Heidelberg, 2002; pp 107-150.

7.      De La Vega, J. C.; Häfeli, U. O., Utilization of nanoparticles as X-ray contrast agents for diagnostic imaging applications. *Contrast Media & Molecular Imaging* **2015,** *10* (2), 81-95.

8.      Lusic, H.; Grinstaff, M. W., X-ray-Computed Tomography Contrast Agents. *Chemical Reviews* **2013,** *113* (3), 1641-1666.

9.      Jost, G.; Lenhard, D. C.; Sieber, M. A.; Lengsfeld, P.; Hütter, J.; Pietsch, H., Changes of Renal Water Diffusion Coefficient After Application of Iodinated Contrast Agents: Effect of Viscosity. *Investigative Radiology* **2011,** *46* (12).

10.     Fähling, M.; Seeliger, E.; Patzak, A.; Persson, P. B., Understanding and preventing contrast-induced acute kidney injury. *Nature Reviews Nephrology* **2017,** *13* (3), 169-180.

11.     Jost, G.; Pietsch, H.; Sommer, J.; Sandner, P.; Lengsfeld, P.; Seidensticker, P.; Lehr, S.; Hütter, J.; Sieber, M. A., Retention of Iodine and Expression of Biomarkers for Renal Damage in the Kidney After Application of Iodinated Contrast Media in Rats. *Investigative Radiology* **2009,** *44* (2).

12.     Seeliger, E.; Sendeski, M.; Rihal, C. S.; Persson, P. B., Contrast-induced kidney injury: mechanisms, risk factors, and prevention. *European Heart Journal* **2012,** *33* (16), 2007-2015.

13.     Trcka, J.; Schmidt, C.; Seitz, C. S.; Bröcker, E.-B.; Gross, G. E.; Trautmann, A., Anaphylaxis to Iodinated Contrast Material: Nonallergic Hypersensitivity or IgE-Mediated Allergy? *American Journal of Roentgenology* **2008,** *190* (3), 666-670.

14.     Inoue, K.; Leung, A. M.; Sugiyama, T.; Tsujimoto, T.; Makita, N.; Nangaku, M.; Ritz, B. R., Urinary Iodine Concentration and Mortality Among U.S. Adults. *Thyroid* **2018,** *28* (7), 913-920.

15.     Jackson, P. A.; Rahman, W. N. W. A.; Wong, C. J.; Ackerly, T.; Geso, M., Potential dependent superiority of gold nanoparticles in comparison to iodinated contrast agents. *European Journal of Radiology* **2010,** *75* (1), 104-109.

16.     Aviv, H.; Bartling, S.; Kieslling, F.; Margel, S., Radiopaque iodinated copolymeric nanoparticles for X-ray imaging applications. *Biomaterials* **2009,** *30* (29), 5610-5616.

17.     Ahn, S.; Jung, S. Y.; Lee, J. P.; Lee, S. J., Properties of Iopamidol-Incorporated Poly(vinyl alcohol) Microparticle as an X-ray Imaging Flow Tracer. *The Journal of Physical Chemistry B* **2011,** *115* (5), 889-901.

18.     Chabner, B. A.; Roberts, T. G., Chemotherapy and the war on cancer. *Nature Reviews Cancer* **2005,** *5* (1), 65-72.

19.     Farokhzad, O. C.; Langer, R., Impact of Nanotechnology on Drug Delivery. *ACS Nano* **2009,** *3* (1), 16-20.

20.     Kim, H.; Beack, S.; Han, S.; Shin, M.; Lee, T.; Park, Y.; Kim, K. S.; Yetisen, A. K.; Yun, S. H.; Kwon, W.; Hahn, S. K., Multifunctional Photonic Nanomaterials for Diagnostic, Therapeutic, and Theranostic Applications. *Advanced Materials* **2018,** *30* (10), 1701460.

21.     Danhier, F.; Feron, O.; Préat, V., To exploit the tumor microenvironment: Passive and active tumor targeting of nanocarriers for anti-cancer drug delivery. *Journal of Controlled Release* **2010,** *148* (2), 135-146.

22.     Santra, S.; Kaittanis, C.; Santiesteban, O. J.; Perez, J. M., Cell-Specific, Activatable, and Theranostic Prodrug for Dual-Targeted Cancer Imaging and Therapy. *Journal of the American Chemical Society* **2011,** *133* (41), 16680-16688.

23.     Torre, L. A.; Siegel, R. L.; Ward, E. M.; Jemal, A., Global Cancer Incidence and Mortality Rates and Trends—An Update. *Cancer Epidemiology Biomarkers &amp;amp; Prevention* **2016,** *25* (1), 16.

24.     Ghosh, A.; Heston, W. D. W., Tumor target prostate specific membrane antigen (PSMA) and its regulation in prostate cancer. *Journal of Cellular Biochemistry* **2004,** *91* (3), 528-539.

25.     Silver, D. A.; Pellicer, I.; Fair, W. R.; Heston, W. D.; Cordon-Cardo, C., Prostate-specific membrane antigen expression in normal and malignant human tissues. *Clinical Cancer Research* **1997,** *3* (1), 81.

26.     DeMarzo, A. M.; Nelson, W. G.; Isaacs, W. B.; Epstein, J. I., Pathological and molecular aspects of prostate cancer. *The Lancet* **2003,** *361* (9361), 955-964.

27.     Perner, S.; Hofer, M. D.; Kim, R.; Shah, R. B.; Li, H.; Möller, P.; Hautmann, R. E.; Gschwend, J. E.; Kuefer, R.; Rubin, M. A., Prostate-specific membrane antigen expression as a predictor of prostate cancer progression. *Human Pathology* **2007,** *38* (5), 696-701.

28.     Eder, M.; Eisenhut, M.; Babich, J.; Haberkorn, U., PSMA as a target for radiolabelled small molecules. *European Journal of Nuclear Medicine and Molecular Imaging* **2013,** *40* (6), 819-823.

29.     Lütje, S.; Heskamp, S.; Cornelissen, A. S.; Poeppel, T. D.; van den Broek, S. A. M. W.; Rosenbaum-Krumme, S.; Bockisch, A.; Gotthardt, M.; Rijpkema, M.; Boerman, O. C., PSMA Ligands for Radionuclide Imaging and Therapy of Prostate Cancer: Clinical Status. *Theranostics* **2015,** *5* (12), 1388-1401.

30.     Dhar, S.; Gu, F. X.; Langer, R.; Farokhzad, O. C.; Lippard, S. J., Targeted delivery of cisplatin to prostate cancer cells by aptamer functionalized Pt(IV) prodrug-PLGA–PEG nanoparticles. *Proceedings of the National Academy of Sciences* **2008,** *105* (45), 17356.

31.     Barinka, C.; Byun, Y.; Dusich, C. L.; Banerjee, S. R.; Chen, Y.; Castanares, M.; Kozikowski, A. P.; Mease, R. C.; Pomper, M. G.; Lubkowski, J., Interactions between Human Glutamate Carboxypeptidase II and Urea-Based Inhibitors: Structural Characterization. *Journal of Medicinal Chemistry* **2008,** *51* (24), 7737-7743.

32.     Banerjee, S. R.; Pullambhatla, M.; Byun, Y.; Nimmagadda, S.; Green, G.; Fox, J. J.; Horti, A.; Mease, R. C.; Pomper, M. G., 68Ga-Labeled Inhibitors of Prostate-Specific Membrane Antigen (PSMA) for Imaging Prostate Cancer. *Journal of Medicinal Chemistry* **2010,** *53* (14), 5333-5341.

33.     Mangadlao, J. D.; Wang, X.; McCleese, C.; Escamilla, M.; Ramamurthy, G.; Wang, Z.; Govande, M.; Basilion, J. P.; Burda, C., Prostate-Specific Membrane Antigen Targeted Gold Nanoparticles for Theranostics of Prostate Cancer. *ACS Nano* **2018,** *12* (4), 3714-3725.

34.     Vidarsson, G.; Dekkers, G.; Rispens, T., IgG Subclasses and Allotypes: From Structure to Effector Functions. *Frontiers in Immunology* **2014,** *5* (520).

35.     Stefanelli, V. L.; Barker, T. H., The evolution of fibrin-specific targeting strategies. *Journal of Materials Chemistry B* **2015,** *3* (7), 1177-1186.

36.     Colombo, M.; Mazzucchelli, S.; Montenegro, J. M.; Galbiati, E.; Corsi, F.; Parak, W. J.; Prosperi, D., Protein Oriented Ligation on Nanoparticles Exploiting O6-Alkylguanine-DNA Transferase (SNAP) Genetically Encoded Fusion. *Small* **2012,** *8* (10), 1492-1497.

37.     Leong, S. S. J.; Chen, W. N., Preparing recombinant single chain antibodies. *Chemical Engineering Science* **2008,** *63* (6), 1401-1414.

38.     Nissim, A.; Chernajovsky, Y., Historical Development of Monoclonal Antibody Therapeutics. In *Therapeutic Antibodies*, Chernajovsky, Y.; Nissim, A., Eds. Springer Berlin Heidelberg: Berlin, Heidelberg, 2008; pp 3-18.

39.     Staneloudi, C.; Smith, K. A.; Hudson, R.; Malatesti, N.; Savoie, H.; Boyle, R. W.; Greenman, J., Development and characterization of novel photosensitizer   :   scFv conjugates for use in photodynamic therapy of cancer. *Immunology* **2007,** *120* (4), 512-517.

40.     Deonarain, M. P.; Yahioglu, G., Current strategies for the discovery and bioconjugation of smaller, targetable drug conjugates tailored for solid tumor therapy. *Expert Opinion on Drug Discovery* **2021,** *16* (6), 613-624.

41.     Montenegro, J.-M.; Grazu, V.; Sukhanova, A.; Agarwal, S.; de la Fuente, J. M.; Nabiev, I.; Greiner, A.; Parak, W. J., Controlled antibody/(bio-) conjugation of inorganic nanoparticles for targeted delivery. *Advanced Drug Delivery Reviews* **2013,** *65* (5), 677-688.

42.     Ha, T. H.; Jung, S. O.; Lee, J. M.; Lee, K. Y.; Lee, Y.; Park, J. S.; Chung, B. H., Oriented Immobilization of Antibodies with GST-Fused Multiple Fc-Specific B-Domains on a Gold Surface. *Analytical Chemistry* **2007,** *79* (2), 546-556.

43.     Lu, B.; Smyth, M. R.; O'Kennedy, R., Tutorial review. Oriented immobilization of antibodies and its applications in immunoassays and immunosensors. *The Analyst* **1996,** *121* (3), 29R.

44.     Simons, J. R.; Mosisch, M.; Torda, A. E.; Hilterhaus, L., Site directed immobilization of glucose-6-phosphate dehydrogenase via thiol-disulfide interchange: Influence on catalytic activity of cysteines introduced at different positions. *Journal of Biotechnology* **2013,** *167* (1), 1-7.

45.     Yin, J.; Liu, F.; Li, X.; Walsh, C. T., Labeling Proteins with Small Molecules by Site-Specific Posttranslational Modification. *Journal of the American Chemical Society* **2004,** *126* (25), 7754-7755.

46.     Sletten, E. M.; Bertozzi, C. R., Bioorthogonal Chemistry: Fishing for Selectivity in a Sea of Functionality. *Angewandte Chemie International Edition* **2009,** *48* (38), 6974-6998.

47.     Welch, N. G.; Scoble, J. A.; Muir, B. W.; Pigram, P. J., Orientation and characterization of immobilized antibodies for improved immunoassays (Review). *Biointerphases* **2017,** *12* (2), 02D301.

48.     Zarrineh, M.; Mashhadi, I. S.; Farhadpour, M.; Ghassempour, A., Mechanism of antibodies purification by protein A. *ANALYTICAL BIOCHEMISTRY* **2020,** *609*.

49.     Crivianu-Gaita, V.; Thompson, M., Immobilization of Fab' fragments onto substrate surfaces: A survey of methods and applications. *BIOSENSORS & BIOELECTRONICS* **2015,** *70*, 167-180.

50.     Terpe, K., Overview of tag protein fusions: from molecular and biochemical fundamentals to commercial systems. *Applied Microbiology and Biotechnology* **2003,** *60* (5), 523-533.

51.     Sapsford, K. E.; Algar, W. R.; Berti, L.; Gemmill, K. B.; Casey, B. J.; Oh, E.; Stewart, M. H.; Medintz, I. L., Functionalizing Nanoparticles with Biological Molecules: Developing Chemistries that Facilitate Nanotechnology. *Chemical Reviews* **2013,** *113* (3), 1904-2074.

52.     Waugh, D. S., Making the most of affinity tags. *Trends in Biotechnology* **2005,** *23* (6), 316-320.

53.     Hussain, A. F.; Heppenstall, P. A.; Kampmeier, F.; Meinhold-Heerlein, I.; Barth, S., One-step site-specific antibody fragment auto-conjugation using SNAP-tag technology. *Nature Protocols* **2019,** *14* (11), 3101-3125.

54.     Keppler, A.; Gendreizig, S.; Gronemeyer, T.; Pick, H.; Vogel, H.; Johnsson, K., A general method for the covalent labeling of fusion proteins with small molecules in vivo. *Nature Biotechnology* **2003,** *21* (1), 86-89.

55.     Engin, S.; Fichtner, D.; Wedlich, D.; Fruk, L., SNAP-tag as a Tool for Surface Immobilization. *CURRENT PHARMACEUTICAL DESIGN* **2013,** *19* (30), 5443-5448.

56.     Kampmeier, F.; Ribbert, M.; Nachreiner, T.; Dembski, S.; Beaufils, F.; Brecht, A.; Barth, S., Site-Specific, Covalent Labeling of Recombinant Antibody Fragments via Fusion to an Engineered

Version of 6-O-Alkylguanine DNA Alkyltransferase. *Bioconjugate Chemistry* **2009,** *20* (5), 1010-1015.

57.     Heinrich, M. C.; Kuhlmann, M. K.; Grgic, A.; Heckmann, M.; Kramann, B.; Uder, M., Cytotoxic Effects of Ionic High-osmolar, Nonionic Monomeric, and Nonionic Iso-osmolar Dimeric Iodinated Contrast Media on Renal Tubular Cells in Vitro. *Radiology* **2005,** *235* (3), 843-849.

58.     Costa, N., Understanding Contrast Media. *Journal of Infusion Nursing* **2004,** *27* (5).

59.     Ashton, J. R.; West, J. L.; Badea, C. T., In vivo small animal micro-CT using nanoparticle contrast agents. *Frontiers in Pharmacology* **2015,** *6* (256).

60.     Hainfeld, J. F.; Ridwan, S. M.; Stanishevskiy, Y.; Panchal, R.; Slatkin, D. N.; Smilowitz, H. M., Iodine nanoparticles enhance radiotherapy of intracerebral human glioma in mice and increase efficacy of chemotherapy. *Scientific Reports* **2019,** *9* (1), 4505.

61.     Bhavane, R.; Badea, C.; Ghaghada, K. B.; Clark, D.; Vela, D.; Moturu, A.; Annapragada, A.; Johnson, G. A.; Willerson, J. T.; Annapragada, A., Dual-Energy Computed Tomography Imaging of Atherosclerotic Plaques in a Mouse Model Using a Liposomal-Iodine Nanoparticle Contrast Agent. *Circulation: Cardiovascular Imaging* **2013,** *6* (2), 285-294.

62.     Banerjee, S. R.; Foss, C. A.; Horhota, A.; Pullambhatla, M.; McDonnell, K.; Zale, S.; Pomper, M. G., 111In- and IRDye800CW-Labeled PLA–PEG Nanoparticle for Imaging Prostate-Specific Membrane Antigen-Expressing Tissues. *Biomacromolecules* **2017,** *18* (1), 201-209.

63.     Kratochwil, C.; Bruchertseifer, F.; Rathke, H.; Bronzel, M.; Apostolidis, C.; Weichert, W.; Haberkorn, U.; Giesel, F. L.; Morgenstern, A., Targeted α-Therapy of Metastatic Castration-Resistant Prostate Cancer with $^{225}$Ac-PSMA-617: Dosimetry Estimate and Empiric Dose Finding. *Journal of Nuclear Medicine* **2017,** *58* (10), 1624.

64.     Weineisen, M.; Schottelius, M.; Simecek, J.; Baum, R. P.; Yildiz, A.; Beykan, S.; Kulkarni, H. R.; Lassmann, M.; Klette, I.; Eiber, M.; Schwaiger, M.; Wester, H.-J., $^{68}$Ga- and $^{177}$Lu-Labeled PSMA I&T: Optimization of a PSMA-Targeted Theranostic Concept and First Proof-of-Concept Human Studies. *Journal of Nuclear Medicine* **2015,** *56* (8), 1169.

65.     Zhou, J.; Neale, J. H.; Pomper, M. G.; Kozikowski, A. P., NAAG peptidase inhibitors and their potential for diagnosis and therapy. *Nature Reviews Drug Discovery* **2005,** *4* (12), 1015-1026.

66.     Bouchelouche, K.; Turkbey, B.; Choyke, P. L., PSMA PET and Radionuclide Therapy in Prostate Cancer. *Seminars in Nuclear Medicine* **2016,** *46* (6), 522-535.

67.     Yong, K. W.; Yuen, D.; Chen, M. Z.; Porter, C. J. H.; Johnston, A. P. R., Pointing in the Right Direction: Controlling the Orientation of Proteins on Nanoparticles Improves Targeting Efficiency. *Nano Letters* **2019,** *19* (3), 1827-1831.

68.     Mazzucchelli, S.; Colombo, M.; De Palma, C.; Salvadè, A.; Verderio, P.; Coghi, M. D.; Clementi, E.; Tortora, P.; Corsi, F.; Prosperi, D., Single-Domain Protein A-Engineered Magnetic Nanoparticles: Toward a Universal Strategy to Site-Specific Labeling of Antibodies for Targeted Detection of Tumor Cells. *ACS Nano* **2010,** *4* (10), 5693-5702.

69.     Choi, H. S.; Liu, W.; Liu, F.; Nasr, K.; Misra, P.; Bawendi, M. G.; Frangioni, J. V., Design considerations for tumour-targeted nanoparticles. *Nature Nanotechnology* **2010,** *5* (1), 42-47.

70.     Colombo, M.; Fiandra, L.; Alessio, G.; Mazzucchelli, S.; Nebuloni, M.; De Palma, C.; Kantner, K.; Pelaz, B.; Rotem, R.; Corsi, F.; Parak, W. J.; Prosperi, D., Tumour homing and therapeutic effect of colloidal nanoparticles depend on the number of attached antibodies. *Nature Communications* **2016,** *7* (1), 13818.

71.     Johnson, P.; Federico, M.; Kirkwood, A.; Fosså, A.; Berkahn, L.; Carella, A.; d'Amore, F.; Enblad, G.; Franceschetto, A.; Fulham, M.; Luminari, S.; O'Doherty, M.; Patrick, P.; Roberts, T.; Sidra, G.; Stevens, L.; Smith, P.; Trotman, J.; Viney, Z.; Radford, J.; Barrington, S., Adapted Treatment Guided by Interim PET-CT Scan in Advanced Hodgkin's Lymphoma. *New England Journal of Medicine* **2016,** *374* (25), 2419-2429.

72.     Makaju, S.; Prasad, P. W. C.; Alsadoon, A.; Singh, A. K.; Elchouemi, A., Lung Cancer Detection

using CT Scan Images. *Procedia Computer Science* **2018,** *125*, 107-114.

73.	Sigal-Cinqualbre, A. B.; Hennequin, R.; Abada, H. T.; Chen, X.; Paul, J.-F., Low-Kilovoltage Multi–Detector Row Chest CT in Adults: Feasibility and Effect on Image Quality and Iodine Dose. *Radiology* **2004,** *231* (1), 169-174.

74.	Cademartiri, F.; de Monye, C.; Pugliese, F.; Mollet, N. R.; Runza, G.; van der Lugt, A.; Midiri, M.; de Feyter, P. J.; Lagalla, R.; Krestin, G. P., High Iodine Concentration Contrast Material for Noninvasive Multislice Computed Tomography Coronary Angiography: Iopromide 370 Versus Iomeprol 400. *Investigative Radiology* **2006,** *41* (3).

75.	Tatsugami, F.; Matsuki, M.; Inada, Y.; Kanazawa, S.; Nakai, G.; Takeda, Y.; Morita, H.; Takada, H.; Ashida, K.; Yoshikawa, S.; Fukumura, K.; Narumi, Y., Feasibility of Low-volume Injections of Contrast Material with a Body Weight–Adapted Iodine-Dose Protocol in 320-Detector Row Coronary CT Angiography. *Academic Radiology* **2010,** *17* (2), 207-211.

76.	Kondo, H.; Kanematsu, M.; Goshima, S.; Tomita, Y.; Kim, M.-J.; Moriyama, N.; Onozuka, M.; Shiratori, Y.; Bae, K. T., Body Size Indexes for Optimizing Iodine Dose for Aortic and Hepatic Enhancement at Multidetector CT: Comparison of Total Body Weight, Lean Body Weight, and Blood Volume. *Radiology* **2009,** *254* (1), 163-169.

77.	Andreucci, M.; Solomon, R.; Tasanarong, A., Side Effects of Radiographic Contrast Media: Pathogenesis, Risk Factors, and Prevention. *BioMed Research International* **2014,** *2014*, 741018.

78.	Hühn, J.; Carrillo-Carrion, C.; Soliman, M. G.; Pfeiffer, C.; Valdeperez, D.; Masood, A.; Chakraborty, I.; Zhu, L.; Gallego, M.; Yue, Z.; Carril, M.; Feliu, N.; Escudero, A.; Alkilany, A. M.; Pelaz, B.; del Pino, P.; Parak, W. J., Selected Standard Protocols for the Synthesis, Phase Transfer, and Characterization of Inorganic Colloidal Nanoparticles. *Chemistry of Materials* **2017,** *29* (1), 399-461.

79.	Zhang, F.; Lees, E.; Amin, F.; Riveragil, P.; Yang, F.; Mulvaney, P.; Parak, W. J., Polymer-Coated Nanoparticles: A Universal Tool for Biolabelling Experiments. *Small* **2011,** *7* (22), 3113-3127.

80.	Park, J.-W.; Shumaker-Parry, J. S., Structural Study of Citrate Layers on Gold Nanoparticles: Role of Intermolecular Interactions in Stabilizing Nanoparticles. *Journal of the American Chemical Society* **2014,** *136* (5), 1907-1921.

81.	Jokerst, J. V.; Lobovkina, T.; Zare, R. N.; Gambhir, S. S., Nanoparticle PEGylation for imaging and therapy. *Nanomedicine* **2011,** *6* (4), 715-728.

82.	Lipka, J.; Semmler-Behnke, M.; Sperling, R. A.; Wenk, A.; Takenaka, S.; Schleh, C.; Kissel, T.; Parak, W. J.; Kreyling, W. G., Biodistribution of PEG-modified gold nanoparticles following intratracheal instillation and intravenous injection. *Biomaterials* **2010,** *31* (25), 6574-6581.

83.	Hou, T.-Y.; Shao, F.-Y.; Sun, Y.-T.; Yang, K.-S.; Chang, W. H.; Lin, C.-A. J., From mono-PEGylation towards anti-nonspecific protein interaction: comparison of dihydrolipoic acid versus glutathione-capped fluorescent gold nanoclusters using gel electrophoresis. *Nanoscale* **2020,** *12* (34), 17786-17794.

84.	Makiura, R.; Yonemura, T.; Yamada, T.; Yamauchi, M.; Ikeda, R.; Kitagawa, H.; Kato, K.; Takata, M., Size-controlled stabilization of the superionic phase to room temperature in polymer-coated AgI nanoparticles. *Nature Materials* **2009,** *8* (6), 476-480.

85.	Liu, D.; Ding, X.; Yang, J.; Ma, Z.; Wang, W. In *A controlling method for AgI nanoparticles preparation using combinatorial surfactants*, 2013 13th IEEE International Conference on Nanotechnology (IEEE-NANO 2013), 5-8 Aug. 2013; 2013; pp 1192-1195.

86.	Chen, S.; Ida, T.; Kimura, K., Thiol-Derivatized AgI Nanoparticles: Synthesis, Characterization, and Optical Properties. *The Journal of Physical Chemistry B* **1998,** *102* (32), 6169-6176.

87.	Lepetit, C.; Maraval, V.; Canac, Y.; Chauvin, R., On the nature of the dative bond: Coordination to metals and beyond. The carbon case. *Coordination Chemistry Reviews* **2016,** *308*, 59-75.

88.	Nold, P.; Hartmann, R.; Feliu, N.; Kantner, K.; Gamal, M.; Pelaz, B.; Hühn, J.; Sun, X.; Jungebluth, P.; del Pino, P.; Hackstein, H.; Macchiarini, P.; Parak, W. J.; Brendel, C., Optimizing

conditions for labeling of mesenchymal stromal cells (MSCs) with gold nanoparticles: a prerequisite for in vivo tracking of MSCs. *Journal of Nanobiotechnology* **2017,** *15* (1), 24.

89.     Sun, X.; Gamal, M.; Nold, P.; Said, A.; Chakraborty, I.; Pelaz, B.; Schmied, F.; von Pückler, K.; Figiel, J.; Zhao, Y.; Brendel, C.; Hassan, M.; Parak, W. J.; Feliu, N., Tracking stem cells and macrophages with gold and iron oxide nanoparticles – The choice of the best suited particles. *Applied Materials Today* **2019,** *15*, 267-279.

90.     Moore, T. L.; Rodriguez-Lorenzo, L.; Hirsch, V.; Balog, S.; Urban, D.; Jud, C.; Rothen-Rutishauser, B.; Lattuada, M.; Petri-Fink, A., Nanoparticle colloidal stability in cell culture media and impact on cellular interactions. *Chemical Society Reviews* **2015,** *44* (17), 6287-6305.

91.     O'Brien, J.; Wilson, I.; Orton, T.; Pognan, F., Investigation of the Alamar Blue (resazurin) fluorescent dye for the assessment of mammalian cell cytotoxicity. *European Journal of Biochemistry* **2000,** *267* (17), 5421-5426.

92.     Rosca, I.; Petrovici, A. R.; Peptanariu, D.; Nicolescu, A.; Dodi, G.; Avadanei, M.; Ivanov, I. C.; Bostanaru, A. C.; Mares, M.; Ciolacu, D., Biosynthesis of dextran by Weissella confusa and its In vitro functional characteristics. *International Journal of Biological Macromolecules* **2018,** *107*, 1765-1772.

93.     Mannerström, M.; Zou, J.; Toimela, T.; Pyykkö, I.; Heinonen, T., The applicability of conventional cytotoxicity assays to predict safety/toxicity of mesoporous silica nanoparticles, silver and gold nanoparticles and multi-walled carbon nanotubes. *Toxicology in Vitro* **2016,** *37*, 113-120.

94.     Mosquera, J.; García, I.; Liz-Marzán, L. M., Cellular Uptake of Nanoparticles versus Small Molecules: A Matter of Size. *Accounts of Chemical Research* **2018,** *51* (9), 2305-2313.

95.     Pan, Y.; Neuss, S.; Leifert, A.; Fischler, M.; Wen, F.; Simon, U.; Schmid, G.; Brandau, W.; Jahnen-Dechent, W., Size-Dependent Cytotoxicity of Gold Nanoparticles. *Small* **2007,** *3* (11), 1941-1949.

96.     Hayashi, H.; Toyota, T.; Goto, S.; Ooishi, A.; Gao, T.; Ee, L. B.; Hatayama, H.; Nomoto, T.; Fujinami, M.; Matsubara, H., Development of a non-blurring, dual-imaging tissue marker for gastrointestinal tumor localization. *Surgical Endoscopy* **2015,** *29* (6), 1445-1451.

97.     Attia, M. F.; Anton, N.; Chiper, M.; Akasov, R.; Anton, H.; Messaddeq, N.; Fournel, S.; Klymchenko, A. S.; Mély, Y.; Vandamme, T. F., Biodistribution of X-Ray Iodinated Contrast Agent in Nano-Emulsions Is Controlled by the Chemical Nature of the Oily Core. *ACS Nano* **2014,** *8* (10), 10537-10550.

98.     Chen, Z.; Li, Y.; Airan, R.; Han, Z.; Xu, J.; Chan, K. W. Y.; Xu, Y.; Bulte, J. W. M.; van Zijl, P. C. M.; McMahon, M. T.; Zhou, S.; Liu, G., CT and CEST MRI bimodal imaging of the intratumoral distribution of iodinated liposomes. *Quant Imaging Med Surg* **2019,** *9* (9), 1579-1591.

99.     Lin, Q.; Jin, C. S.; Huang, H.; Ding, L.; Zhang, Z.; Chen, J.; Zheng, G., Nanoparticle-Enabled, Image-Guided Treatment Planning of Target Specific RNAi Therapeutics in an Orthotopic Prostate Cancer Model. *Small* **2014,** *10* (15), 3072-3082.

100.    Hainfeld, J. F.; Ridwan, S. M.; Stanishevskiy, Y.; Smilowitz, N. R.; Davis, J.; Smilowitz, H. M., Small, Long Blood Half-Life Iodine Nanoparticle for Vascular and Tumor Imaging. *Scientific Reports* **2018,** *8* (1), 13803.

101.    Mansouri, M.; Shahbazi-Gahrouei, D., A review on theranostic applications of iodine nanoparticles: Recent findings and perspectives. *NANOMEDICINE JOURNAL* **2021,** *8* (4), 234-240.

102.    Kim, J.; Chhour, P.; Hsu, J.; Litt, H. I.; Ferrari, V. A.; Popovtzer, R.; Cormode, D. P., Use of Nanoparticle Contrast Agents for Cell Tracking with Computed Tomography. *Bioconjugate Chemistry* **2017,** *28* (6), 1581-1597.

103.    Khademi, S.; Sarkar, S.; Shakeri-Zadeh, A.; Attaran, N.; Kharrazi, S.; Ay, M. R.; Ghadiri, H., Folic acid-cysteamine modified gold nanoparticle as a nanoprobe for targeted computed tomography imaging of cancer cells. *Materials Science and Engineering: C* **2018,** *89*, 182-193.

104.    Bae, K. T., Intravenous Contrast Medium Administration and Scan Timing at CT: Considerations and Approaches. *Radiology* **2010,** *256* (1), 32-61.

105. Akter, M.; Sikder, M. T.; Rahman, M. M.; Ullah, A. K. M. A.; Hossain, K. F. B.; Banik, S.; Hosokawa, T.; Saito, T.; Kurasaki, M., A systematic review on silver nanoparticles-induced cytotoxicity: Physicochemical properties and perspectives. *Journal of Advanced Research* **2018,** *9*, 1-16.

106. Siegel, R.; Ma, J.; Zou, Z.; Jemal, A., Cancer statistics, 2014. *CA Cancer J Clin* **2014,** *64* (1), 9-29.

107. Qi, T.; Chen, Y.; Zhu, Y.; Jiang, J.; Wang, L.; Qi, J., Contrast-enhanced Transrectal Ultrasonography for Detection and Localization of Prostate Index Tumor: Correlation With Radical Prostatectomy Findings. *Urology* **2014,** *84* (1), 138-143.

108. Schmittgen, T. D.; Teske, S.; Vessella, R. L.; True, L. D.; Zakrajsek, B. A., Expression of prostate specific membrane antigen and three alternatively spliced variants of PSMA in prostate cancer patients. *International Journal of Cancer* **2003,** *107* (2), 323-329.

109. Lee, S. S.; Roche, P. J. R.; Giannopoulos, P. N.; Mitmaker, E. J.; Tamilia, M.; Paliouras, M.; Trifiro, M. A., Prostate-specific membrane antigen–directed nanoparticle targeting for extreme nearfield ablation of prostate cancer cells. *Tumor Biology* **2017,** *39* (3), 1010428317695943.

110. Nagesh, P. K. B.; Johnson, N. R.; Boya, V. K. N.; Chowdhury, P.; Othman, S. F.; Khalilzad-Sharghi, V.; Hafeez, B. B.; Ganju, A.; Khan, S.; Behrman, S. W.; Zafar, N.; Chauhan, S. C.; Jaggi, M.; Yallapu, M. M., PSMA targeted docetaxel-loaded superparamagnetic iron oxide nanoparticles for prostate cancer. *Colloids and Surfaces B: Biointerfaces* **2016,** *144*, 8-20.

111. Xu, M.; Soliman, M. G.; Sun, X.; Pelaz, B.; Feliu, N.; Parak, W. J.; Liu, S., How Entanglement of Different Physicochemical Properties Complicates the Prediction of in Vitro and in Vivo Interactions of Gold Nanoparticles. *ACS Nano* **2018,** *12* (10), 10104-10113.

112. Foss, C. A.; Hornyak, G. L.; Stockert, J. A.; Martin, C. R., Template-Synthesized Nanoscopic Gold Particles: Optical Spectra and the Effects of Particle Size and Shape. *The Journal of Physical Chemistry* **1994,** *98* (11), 2963-2971.

113. Dobrucka, R.; Dlugaszewska, J., Biomimetic synthesis of nanogold using Bidens tripartitus extract and evalution of their antimicrobial and catalytic activities. *Inorganic and Nano-Metal Chemistry* **2020,** *50* (6), 459-468.

114. Haiss, W.; Thanh, N. T. K.; Aveyard, J.; Fernig, D. G., Determination of Size and Concentration of Gold Nanoparticles from UV−Vis Spectra. *Analytical Chemistry* **2007,** *79* (11), 4215-4221.

115. Piella, J.; Bastús, N. G.; Puntes, V., Size-Dependent Protein–Nanoparticle Interactions in Citrate-Stabilized Gold Nanoparticles: The Emergence of the Protein Corona. *Bioconjugate Chemistry* **2017,** *28* (1), 88-97.

116. Gebauer, J. S.; Malissek, M.; Simon, S.; Knauer, S. K.; Maskos, M.; Stauber, R. H.; Peukert, W.; Treuel, L., Impact of the Nanoparticle–Protein Corona on Colloidal Stability and Protein Structure. *Langmuir* **2012,** *28* (25), 9673-9679.

117. Ho, Y. T.; Azman, N. A.; Loh, F. W. Y.; Ong, G. K. T.; Engudar, G.; Kriz, S. A.; Kah, J. C. Y., Protein Corona Formed from Different Blood Plasma Proteins Affects the Colloidal Stability of Nanoparticles Differently. *Bioconjugate Chemistry* **2018,** *29* (11), 3923-3934.

118. You, J.; Cozzi, P.; Walsh, B.; Willcox, M.; Kearsley, J.; Russell, P.; Li, Y., Innovative biomarkers for prostate cancer early diagnosis and progression. *Critical Reviews in Oncology/Hematology* **2010,** *73* (1), 10-22.

119. Hövels, A. M.; Heesakkers, R. A. M.; Adang, E. M.; Jager, G. J.; Strum, S.; Hoogeveen, Y. L.; Severens, J. L.; Barentsz, J. O., The diagnostic accuracy of CT and MRI in the staging of pelvic lymph nodes in patients with prostate cancer: a meta-analysis. *Clinical Radiology* **2008,** *63* (4), 387-395.

120. Rajasekaran, S. A.; Anilkumar, G.; Oshima, E.; Bowie, J. U.; Liu, H.; Heston, W.; Bander, N. H.; Rajasekaran, A. K., A Novel Cytoplasmic Tail MXXXL Motif Mediates the Internalization of Prostate-specific Membrane Antigen. *Molecular Biology of the Cell* **2003,** *14* (12), 4835-4845.

121. A. Foss, C.; C. Mease, R.; Y. Cho, S.; J. Kim, H.; G. Pomper, M., GCPII Imaging and Cancer.

*Current Medicinal Chemistry* **2012,** *19* (9), 1346-1359.

122.    Cho, S. Y.; Gage, K. L.; Mease, R. C.; Senthamizhchelvan, S.; Holt, D. P.; Jeffrey-Kwanisai, A.; Endres, C. J.; Dannals, R. F.; Sgouros, G.; Lodge, M.; Eisenberger, M. A.; Rodriguez, R.; Carducci, M. A.; Rojas, C.; Slusher, B. S.; Kozikowski, A. P.; Pomper, M. G., Biodistribution, Tumor Detection, and Radiation Dosimetry of &lt;sup&gt;18&lt;/sup&gt;F-DCFBC, a Low-Molecular-Weight Inhibitor of Prostate-Specific Membrane Antigen, in Patients with Metastatic Prostate Cancer. *Journal of Nuclear Medicine* **2012,** *53* (12), 1883.

123.    Schulz, F.; Dahl, G. T.; Besztejan, S.; Schroer, M. A.; Lehmkühler, F.; Grübel, G.; Vossmeyer, T.; Lange, H., Ligand Layer Engineering To Control Stability and Interfacial Properties of Nanoparticles. *Langmuir* **2016,** *32* (31), 7897-7907.

124.    Feliu, N.; Sun, X.; Alvarez Puebla, R. A.; Parak, W. J., Quantitative Particle–Cell Interaction: Some Basic Physicochemical Pitfalls. *Langmuir* **2017,** *33* (27), 6639-6646.

125.    Benešová, M.; Bauder-Wüst, U.; Schäfer, M.; Klika, K. D.; Mier, W.; Haberkorn, U.; Kopka, K.; Eder, M., Linker Modification Strategies To Control the Prostate-Specific Membrane Antigen (PSMA)-Targeting and Pharmacokinetic Properties of DOTA-Conjugated PSMA Inhibitors. *Journal of Medicinal Chemistry* **2016,** *59* (5), 1761-1775.

126.    Paul, W.; Sharma, C. P., 13 - Inorganic nanoparticles for targeted drug delivery. In *Biointegration of Medical Implant Materials (Second Edition)*, Sharma, C. P., Ed. Woodhead Publishing: 2020; pp 333-373.

127.    Henriksen-Lacey, M.; Carregal-Romero, S.; Liz-Marzán, L. M., Current Challenges toward In Vitro Cellular Validation of Inorganic Nanoparticles. *Bioconjugate Chemistry* **2017,** *28* (1), 212-221.

128.    Zhao, X.; Pan, F.; Lu, J. R., Interfacial assembly of proteins and peptides: recent examples studied by neutron reflection. *Journal of The Royal Society Interface* **2009,** *6* (suppl_5), S659-S670.

129.    Elias, D. R.; Poloukhtine, A.; Popik, V.; Tsourkas, A., Effect of ligand density, receptor density, and nanoparticle size on cell targeting. *Nanomedicine: Nanotechnology, Biology and Medicine* **2013,** *9* (2), 194-201.

130.    Wen, T.; Majetich, S. A., Ultra-Large-Area Self-Assembled Monolayers of Nanoparticles. *ACS Nano* **2011,** *5* (11), 8868-8876.

131.    Sperling, R. A.; Pellegrino, T.; Li, J. K.; Chang, W. H.; Parak, W. J., Electrophoretic Separation of Nanoparticles with a Discrete Number of Functional Groups. *Advanced Functional Materials* **2006,** *16* (7), 943-948.

132.    Wichner, S. M.; Mann, V. R.; Powers, A. S.; Segal, M. A.; Mir, M.; Bandaria, J. N.; DeWitt, M. A.; Darzacq, X.; Yildiz, A.; Cohen, B. E., Covalent Protein Labeling and Improved Single-Molecule Optical Properties of Aqueous CdSe/CdS Quantum Dots. *ACS Nano* **2017,** *11* (7), 6773-6781.

133.    Zhang, P.; Lu, H.; Chen, J.; Han, H.; Ma, W., Simple and sensitive detection of HBsAg by using a quantum dots nanobeads based dot-blot immunoassay. *Theranostics* **2014,** *4* (3), 307-315.

134.    Kim, B. B.; Pisarev, V. V.; Egorov, A. M., A comparative study of peroxidases from horse radish and Arthromyces ramosus as labels in luminol-mediated chemiluminescent assays. *Analytical Biochemistry* **1991,** *199* (1), 1-6.

135.    Wang, H.; Yuan, R.; Chai, Y.; Niu, H.; Cao, Y.; Liu, H., Bi-enzyme synergetic catalysis to in situ generate coreactant of peroxydisulfate solution for ultrasensitive electrochemiluminescence immunoassay. *Biosensors and Bioelectronics* **2012,** *37* (1), 6-10.

136.    Lee, P. Y.; Wong, K. K. Y., Nanomedicine: A New Frontier in Cancer Therapeutics. *CURRENT DRUG DELIVERY* **2011,** *8* (3), 245-253.

137.    Allen, T. M., Ligand-targeted therapeutics in anticancer therapy. *Nature Reviews Cancer* **2002,** *2* (10), 750-763.

138.    Rapoport, N., Physical stimuli-responsive polymeric micelles for anti-cancer drug delivery. *Progress in Polymer Science* **2007,** *32* (8), 962-990.

139.    Crivianu-Gaita, V.; Thompson, M., Aptamers, antibody scFv, and antibody Fab' fragments:

An overview and comparison of three of the most versatile biosensor biorecognition elements. *Biosensors and Bioelectronics* **2016,** *85*, 32-45.

140.     Puertas, S.; Moros, M.; Fernández-Pacheco, R.; Ibarra, M. R.; Grazú, V.; de la Fuente, J. M., Designing novel nano-immunoassays: antibody orientation versus sensitivity. *Journal of Physics D: Applied Physics* **2010,** *43* (47), 474012.

141.     Sugawara, K.; Ishizaki, S.; Kikuchi, S.; Kuramitz, H.; Kadoya, T., Construction of Protein Probe with a His-tag and an Electron-transfer Peptide for a Target Protein Sensing. *Electroanalysis* **2021,** *33* (4), 975-986.

142.     Bosch, Peter J.; Corrêa, Ivan R.; Sonntag, Michael H.; Ibach, J.; Brunsveld, L.; Kanger, Johannes S.; Subramaniam, V., Evaluation of Fluorophores to Label SNAP-Tag Fused Proteins for Multicolor Single-Molecule Tracking Microscopy in Live Cells. *Biophysical Journal* **2014,** *107* (4), 803-814.

143.     Mazzucchelli, S.; Colombo, M.; Verderio, P.; Rozek, E.; Andreata, F.; Galbiati, E.; Tortora, P.; Corsi, F.; Prosperi, D., Orientation-Controlled Conjugation of Haloalkane Dehalogenase Fused Homing Peptides to Multifunctional Nanoparticles for the Specific Recognition of Cancer Cells. *Angewandte Chemie International Edition* **2013,** *52* (11), 3121-3125.

144.     Partikel, K.; Korte, R.; Stein, N. C.; Mulac, D.; Herrmann, F. C.; Humpf, H.-U.; Langer, K., Effect of nanoparticle size and PEGylation on the protein corona of PLGA nanoparticles. *European Journal of Pharmaceutics and Biopharmaceutics* **2019,** *141*, 70-80.

145.     Mori, Y.; Nagaoka, S.; Takiuchi, H.; Kikuchi, T.; Noguchi, N.; Tanzawa, H.; Noishiki, Y., A new antithrombogenic material with long polyethyleneoxide chains. *Trans Am Soc Artif Intern Organs* **1982,** *28*, 459-463.

146.     Kitano, H.; Kawasaki, A.; Kawasaki, H.; Morokoshi, S., Resistance of zwitterionic telomers accumulated on metal surfaces against nonspecific adsorption of proteins. *Journal of Colloid and Interface Science* **2005,** *282* (2), 340-348.

147.     Hu, Y.; Yang, G.; Liang, B.; Fang, L.; Ma, G.; Zhu, Q.; Chen, S.; Ye, X., The fabrication of superlow protein absorption zwitterionic coating by electrochemically mediated atom transfer radical polymerization and its application. *Acta Biomaterialia* **2015,** *13*, 142-149.

148.     Bao, C.; Conde, J.; Polo, E.; del Pino, P.; Moros, M.; Baptista, P. V.; Grazu, V.; Cui, D.; de la Fuente, J. M., A promising road with challenges: where are gold nanoparticles in translational research? *Nanomedicine* **2014,** *9* (15), 2353-2370.

149.     García, K. P.; Zarschler, K.; Barbaro, L.; Barreto, J. A.; O'Malley, W.; Spiccia, L.; Stephan, H.; Graham, B., Zwitterionic-Coated "Stealth" Nanoparticles for Biomedical Applications: Recent Advances in Countering Biomolecular Corona Formation and Uptake by the Mononuclear Phagocyte System. *Small* **2014,** *10* (13), 2516-2529.

# Publications

1. **Y. Kang**, N. Feliu, W. J. Parak "Quantitative comparison of different iodine labels as intracellular labels for cell tracking", in preparation

2. **Y. Kang**, L. Nack, Y. Liu, B. Qi, Y. Huang, Z. Liu, I. Chakraborty, F. Schulz, A. Ahmed, M. Clavo Podeva, F. Hafizi, S. Roy, M. Mutas, M. Holzapfel, C. Sanchez Cano, K. D. Wegner, N. Feliu, W. J. Parak, "Quantitative considerations about the size dependency for cellular entry and excretion of colloidal nanoparticles for different cells", ChemTexts, in revision.

3. J. M. Romo-Herrera, K. Juarez-Moreno, L. Guerrini, **Y. Kang**, N. Feliu, W. J. Parak, R. A. Alvarez-Puebla, "Paper-based plasmonic substrates as surface-enhanced Raman scattering spectroscopy platforms for cell culture applications", Materials Today Bio 11, 100125 (2021).

4. O. Schmutzler, S. Graf, N. Behm, W. Y. Mansour, F. Blumendorf, T. Staufer, C. Körnig, D. Salah, **Y. Kang**, J. N. Peters, Y. Liu, N. Feliu, W. J. Parak, A. Burkhardt, E. Gargioni, S. Gennis, S. Chandralingam, F. Höeg, W. Maison, K. Rothkamm, F. Schulz, F. Grüner, "X-Ray Fluorescence Uptake Measurement of Functionalized Gold Nanoparticles in Tumor Cell Microsamples", International Journal of Molecular Sciences 22, 3691 (2021).

5. C. Sanchez-Cano, R. A. Alvarez-Puebla, J. M. Abendroth, T. Beck, R. Blick, Y. Cao, F. Caruso, I. Chakraborty, H. N. Chapman, C. Chen, B. E. Cohen, A. L. C. Conceição, D. P. Cormode, D. Cui, K. A. Dawson, N. Feliu, M. Gao, E. Gargioni, C. C. Glüer, F. Grüner, M. Hassan, Y. Hu, Y. Huang, S. Huber, N. Huse, **Y. Kang**, A. Khademhosseini, T. F. Keller, C. Körnig, N. A. Kotov, D. Koziej, X.-J. Liang, B. Liu, S. Liu, Y. Liu, Z. Liu, L. M. Liz-Marzan, X. Ma, A. Machicote, W. Maison, A. P. Mancuso, S. Megahed, B. Nickel, F. Otto, C. Palencia Ramirez, S. Pascarelli, A. Pearson, O. PeñateMedina, B. Qi , T. Staufer, D. M. Stemer, A. Stierle, X. Sun, G. Tsakanova, P. S. Weiss, H. Weller, F. Westermeier, M. Xu, H. Yan, Y. Zeng, Y. Zhao, Y. Zhao, D. Zhu, Y. Zhu, W. J. Parak, et al. "X-Ray-Based Techniques to Study the Nano-Bio Interface", ACS Nano 15, 3554-3807 (2021).

## Acknowledgements

# Abbreviations

| | |
|---|---|
| TEM | Transmission electron microscopy |
| DLS | Dynamic light scattering |
| NMR | Nuclear magnetic resonance |
| FBS | Fetal bovine serum |
| PBS | Phosphate buffered saline |
| PMA | Phorbol 12-myristate 13-acetate |
| P/S | Penicillin/streptomycin |
| DMEM | Dulbecco's Modified Eagle's Medium |
| RPMI 1640 | Roswell Park Memorial Institute 1640 Medium |
| BSA | Bovine serum albumin |
| DDA | dodecylamine |
| EDC | N-(3-Dimethylaminopropyl)-N'-ethylcarbodiimide hydrochloride |
| SBB | sodium borate buffer |
| DDT | 1-dodecanethiol |
| TOAB | Tetraoctylammoniumbromid |
| 4IH | 4-Iodobenzylamine hydrochloride |

# List of hazardous substances

| Substance | GHS pictograms | Hazard Sentences | Precaution Sentence |
|---|---|---|---|
| RPMI-1640 medium | Not hazardous substance | | |
| Sodium pyruvate solution | Not hazardous substance | | |
| Dulbecco's modified eagle medium | Not hazardous substance | | |
| Penicillin/streptomycin | Not hazardous substance | | |
| Fetal bovine serum | Not hazardous substance | | |
| Resazurin | Not hazardous substance | | |
| Phosphate buffered saline | Not hazardous substance | | |
| 0.05% trypsin/EDTA | Not hazardous substance | | |
| Sodium citrate | Not hazardous substance | | |
| poly(isobutylene-alt-maleic anhydride) | Not hazardous substance | | |
| Bovine serum albumin | Not hazardous substance | | |
| Sodium chloride | Not hazardous substance | | |

| | | | |
|---|---|---|---|
| gold(III) chloride trihydrate | Danger | H314-H317 | P305 + P351 + P338-P310 |
| Sodium hydroxide | Danger | H290-H314 | P260-P280-P303 + P361 3-P304 + P340 + P310-P305 + P351 + P338 |
| Silver nitrite | Warning, Danger | H272+H314 +H400+H410 | P210, P220, P221, P260, P264, P273, P280, P301+P330+P331, P303+P361+P353, P304+P340, P305+P351+P338, P310, P321, P363, P370+P378, P391, P405, and P501 |
| N-(3-Dimethylaminopropyl) - N'-ethylcarbodiimide hydrochloride | Danger | H315-H318-H335 | P261-P280-P305 + P351 + P338 |
| Sodium iodide | Warning | H315-H319-H400 | P273-P305 + P351 + P338 |
| β-mercaptoethanol | Danger | H331- H310-H315-H317- H318-H373-H410 | P273-P280-P301 + P310-P302 + P350-P305 + P351 + P338 |
| Tetraoctylammonium bromide | Warning | H315+H319+H33 5 | P261, P264, P271, P280, P302+P352, P304+P340, P305+P351+P338, P312, P321, |

| | | | P332+P313, P337+P313, P362, P403+P233, P405, and P501 |
|---|---|---|---|
| Methanol | Danger | H225+H301+H311+H331+H370 | P210, P233, P240, P241, P242, P243, P260, P261, P264, P270, P271, P280, P301+P310, P302+P352, P303+P361+P353, P304+P340, P307+P311, P311, P312, P321, P322, P330, P361, P363, P370+P378, P403+P233, P403+P235, P405, and P501 |
| Sodium borohydride | Danger | H260+H301+H311+H314+H318+H332+H360 | P201, P202, P223, P231+P232, P260, P261, P264, P270, P271, P280, P281, P301+P310, P301+P330+P331, P302+P352, P303+P361+P353, P304+P312, P304+P340, |

| | | | P305+P351+P338, |
|---|---|---|---|
| | | | P308+P313, P310, |
| | | | P312, P321, P322, |
| | | | P330, P335+P334, |
| | | | P361, P363, |
| | | | P370+P378, |
| | | | P402+P404, P405, and |
| | | | P501 |
| 1- dodecanethiol | Danger | H302+H304+H312+H314+H315+H317+H318+H319+H332+H334+H335+H400+H410 | P260, P261, P264, P270, P271, P272, P273, P280, P285, P301+P310, P301+P312, P301+P330+P331, P302+P352, P303+P361+P353, P304+P312, P304+P340, P304+P341, P305+P351+P338, P310, P312, P321, P322, P330, P331, P332+P313, P333+P313, P337+P313, P342+P311, P362, P363, P391, P403+P233, P405, P501 |

| | | | |
|---|---|---|---|
| dodecylamine | Danger | H302+H304+H314+H318+H335+H373+H400+H410 | P260, P261, P264, P270, P271, P273, P280, P301+P310, P301+P312, P301+P330+P331, P303+P361+P353, P304+P340, P305+P351+P338, P310, P312, P314, P321, P330, P331, P363, P391, P403+P233, P405, and P501 |
| CHO-PEG-SH 2000 | Warning | H302 | P264, P270, P301+P312, P330, and P501 |
| iohexol | Warning | H315+H319 | P264, P280, P302+P352, P305+P351+P338, P321, P332+P313, P337+P313, and P362 |
| CM-dextran | Not hazardous substance | | |

# Declaration on oath

I hereby declare on oath, that I have written the present dissertation by my own and have not used other than the acknowledged resources and aids.


Date


Signature